

**The feasibility of targeting REEs in
tailings using satellite remote sensing
data: A case study of abandoned mine
sites, in Bangka Island, Indonesia**

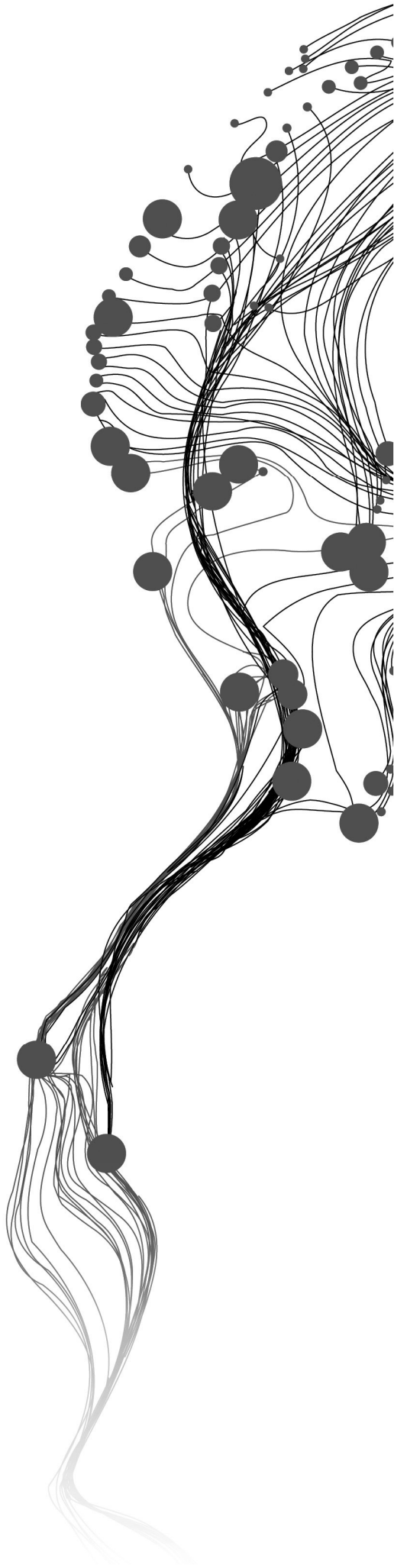
IMAM PURWADI

February, 2018

SUPERVISORS:

Dr. Harald van der Werff

Dr. Caroline Lievens



The feasibility of targeting REEs in tailings using satellite remote sensing data: A case study of abandoned mine sites, in Bangka Island, Indonesia

IMAM PURWADI

Enschede, the Netherlands, February, 2018

Thesis submitted to the Faculty of Geo-Information Science and Earth Observation of the University of Twente in partial fulfilment of the requirements for the degree of Master of Science in Geo-information Science and Earth Observation.

Specialization: Applied Earth Sciences - Geological Remote Sensing

SUPERVISORS:

Dr. Harald van der Werff

Dr. Caroline Lievens

THESIS ASSESSMENT BOARD:

Prof. Dr. F.D. (Freek) van der Meer (Chair)

Dr. Fiorenza Deon

DISCLAIMER

This document describes work undertaken as part of a programme of study at the Faculty of Geo-Information Science and Earth Observation of the University of Twente. All views and opinions expressed therein remain the sole responsibility of the author, and do not necessarily represent those of the Faculty.

ABSTRACT

Rare Earth Elements (REEs) were once considered as unwanted elements and discarded with other elements as tailing in mining industry. Presently, REEs are sought and could turn tailings into a precious resource. Remote sensing can serve as a method for locating REE-bearing tailings. However, the existing studies mainly focus on studying the spectroscopy of pure REE-bearing minerals in the laboratory scale. In this study, REE concentrations in tailing samples were quantified using ICP-OES. Then, we linked variations in the spectral absorption features of REE-bearing tailings in the Visible and Near Infrared (VNIR) wavelength range to REE concentrations. The spatial and spectral specifications of a satellite remote sensing required to target REE-bearing tailings were determined by evaluating the capability of several satellite remote sensing.

In the VNIR wavelength range, we expected to observe the famous Nd^{3+} absorption features at around 745nm, 802nm, and 871nm, yet none of our samples had distinct absorption features related to Nd^{3+} . Nevertheless, a new absorption feature was observed centred at around 674nm, which has never been reported in the previous literature. Through this study, we have also discovered an unexpected high concentration of Erbium (Er) - even higher than Er concentration in the processed REE ore of Mount Pass deposit. Moreover, in one of our data set, the 674nm absorption feature and Er concentration had a strong correlation with Pearson correlation coefficient as high as 0.829.

Algorithms were developed to target the 674 absorption feature related to Erbium using a satellite remote sensing, and we found that the algorithms can identify a pixel with the 674 absorption feature. By comparing the capability of Sentinel-2 MSI and Landsat 8 OLI to target this absorption feature, the spatial and spectral specifications of a satellite remote sensing for targeting REEs in the study area were defined. A satellite remote sensing with a 10m spatial resolution or higher is required. In terms of spectral resolution, a satellite sensor with a spectral specification equivalent to or higher than Sentinel-2 MSI suffices.

ACKNOWLEDGEMENTS

I owe my sincere gratitude to many people who have helped me in completing this thesis. Of these generous people, I would like to mention a few of them.

Harald van der Werff and Caroline Lievens, my word is not enough to express my gratitude. Harald and Caroline, I thank you for your advice and your patience. Harald, I thank you for keeping me on the right track, when I am conducting this research. Caroline, I am grateful that you supervised and allowed me working in ITC Geoscience laboratory, even though I could not tell differences between nitric acid and citric acid.

Freek van der Meer and Fiorenza Deon, I thank you that you chose to partake in the examination of this thesis. Freek, I thank you for your supervision during the proposal and mid-term presentation. Fiorenza, I thank you for your help in answering my questions related to fieldwork regulation in Indonesia.

Also, I would like to thank Chris Hecker for his help in the early stage of this research, Wim Bakker for his suggestion and permission to allow me using spectrometers, and Bart Krol for his help in making this research to be possible.

My gratitude is also to LPDP scholarships who fully financed my studies and to geological remote sensing group who gave financial support to this research.

TABLE OF CONTENTS

1. Introduction.....	1
1.1. Problem definition.....	1
1.2. Research objectives.....	2
1.3. Research questions.....	2
1.4. Thesis structure.....	2
2. Research background.....	3
2.1. Study area.....	3
2.2. Rare earth elements.....	4
2.3. Existing studies on REE spectral reflectance.....	4
3. Material and Methodology.....	6
3.1. Material.....	6
3.1.1. Field samples.....	6
3.1.2. A mixture of Quartz and Xenotime.....	9
3.1.3. Satellite remote sensing images.....	9
3.1.4. Software used.....	10
3.2. Methodology.....	10
3.2.1. Sample preparation.....	10
3.2.2. Data acquisition.....	11
3.2.3. Data analysis.....	13
3.2.4. Evaluating the feasibility of targeting REEs using satellite remote sensing.....	15
4. Results.....	18
4.1. Chemical composition.....	18
4.2. Spectral reflectance data.....	20
4.3. Statistical correlation between REE concentration and spectral reflectance.....	24
4.4. Quantitative relationships.....	28
4.5. REE detectability by satellite remote sensing sensors.....	28
4.6. Application to multispectral images.....	31
5. Discussion.....	35
5.1. Chemical compositions.....	35
5.2. Spectral reflectance.....	35
5.3. The effect of samples preparation.....	36
5.4. Statistical correlation between REE concentration and spectral reflectance.....	37
5.5. Quantitative relationship.....	37
5.6. Probable origin of the 674 absorption feature and material carrying REEs.....	37
5.7. REE detectability by satellite remote sensing sensors.....	38
5.8. Application to multispectral images.....	39
5.9. The origin of absorption features at band 4, 5, and 6 of the Sentinel-2 MSI image.....	40
6. Discriminating three absorption features.....	41
7. Conclusion and Recommendation.....	43
7.1. Conclusion.....	43
7.2. Recommendations.....	44
8. Appendixes.....	48

LIST OF FIGURES

Figure 1 Top-Left: Orange box indicates the location of the study area.	3
Figure 2 a) The boundary of location 1 (a red-dashed box), location 2 (a green-dashed box),.....	6
Figure 3 a) Subset of Sentinel-2 MSI natural colour image (shown in Figure 2a) showing location 1.....	6
Figure 4 The collected tailing samples were divided into two data sets,	7
Figure 5 a) Showing the band position of WorldView2, Sentinel-2 MSI, and Landsat 8 OLI,.....	9
Figure 6 Graphs illustrating the signal intensity of element being measured in ICP-OES.	12
Figure 7 REE concentration in the UCC.....	13
Figure 8 Spectral variations in sample spectra in the VNIR wavelength range	14
Figure 9 Illustration of calculating band ratio, band depth, and band math.	16
Figure 10 A comparison between the mean REE concentrations.....	19
Figure 11 Chondrite-normalized REE distribution of mean REE concentrations.....	19
Figure 12 a) Showing the diffractogram of 10 samples.....	20
Figure 13 a) The spectral reflectance of a mixture of Quartz and Xenotime.....	21
Figure 14 The min, mean, and max spectra of the samples of location 1(a),.....	22
Figure 15 A comparison of the mean spectra of the samples from location 2 and 3.	22
Figure 16 An illustration of ROI and its mean spectra.	23
Figure 17 a) Spectral variation varying in REE concentrations.....	23
Figure 18 Pearson correlation coefficient among REE and Fe concentrations.....	24
Figure 19 Pearson correlation value between the depth of continuum-removed spectra.....	25
Figure 20 Location 1: Pearson correlation coefficients between spectral parameters and REE.....	26
Figure 21 Location 2 and 3: Pearson correlation coefficients between spectral parameters and REE.....	27
Figure 22 Plots showing the result of resampling spectra	29
Figure 23 A comparison of Sentinel-2 MSI and Landsat 8 OLI spatial resolution.....	29
Figure 24 a) A false colour composite of Sentinel-2 MSI band 6, 4, 3 (R-G-B) in a 2-98% linear stretch. .	31
Figure 25 Image products after removing vegetation and water areas.....	32
Figure 26 Colour composite images of band ratio, depth, and math derived.....	33
Figure 27 Comparing spectral variations in absorption features.....	33
Figure 28 a) Subset Figure 26b.....	41
Figure 29 Colour composite images of band ratio, depth, and math	42

LIST OF TABLES

Table 1 The list of candidate and used wavelengths for REEs.....	11
Table 2 The concentration of REE in water-leached samples from location 1 and natural water samples	18
Table 3 REE concentrations in total concentration samples.	18
Table 4 The concentrations of major elements.	20
Table 5 REE concentrations in the mixture of Quartz (Q) and Xenotime (X).....	21
Table 6 The Estimation of Precision (EOP) between duplicated samples.....	24
Table 7 Pearson correlation coefficients between three spectral parameters.....	27
Table 8 Statistical summary of stepwise and enter multilinear regressions.....	28
Table 9 Statistical summary of stepwise and enter multilinear regressions.....	28
Table 10 Pearson correlation coefficients between spectral parameters and REE concentrations.....	30
Table 11 Pearson correlation coefficients between spectral parameters and REE concentrations.....	30

LIST OF APPENDIXES

Appendix A Grain size 48

Appendix B Map showing the distribution of tailing and water sample 49

Appendix C Procedure for selecting samples of location 2 and 3 52

Appendix D The created scripts 53

Appendix E The arrangement of 126 grains..... 58

Appendix F Images of NDVI products and water masked 62

Appendix G Images of spectral parameter products 63

LIST OF ABBREVIATIONS

REEs	Rare Earth Elements
LREEs	Light Rare Earth Elements
HREEs	Heavy Rare Earth Elements
VNIR	Visible and Near-Infrared
La	Lanthanum
Ce	Cerium
Pr	Praseodymium
Tb	Terbium
Dy	Dysprosium
Ho	Holmium
Er	Erbium
Tm	Thulium
Yb	Ytterbium
Lu	Lutetium
Sc	Scandium
Y	Yttrium
nm	Nanometre
µg	Micrometre
mm	Millimetre
ICP-OES	Inductively Coupled Plasma Optical Emission Spectrometry
LOD	Limits of Detection
FTIR-ATR	Fourier Transform Infrared - Attenuated Total Reflectance
XRD	X-ray Diffraction
ROI	Region of Interest
R ²	the coefficient of determination
r	Pearson correlation coefficient
RPD	Residual Prediction Deviation
NDVI	Normalized Difference Vegetation Index
UCC	Upper Continental Crust
AVIRIS	Airborne Visible-Infrared Imaging Spectrometer
EOP	Estimation of Precision

1. INTRODUCTION

1.1. Problem definition

Tailings refer to mine waste material that is left after extracting a particular ore from a deposit (Lottermoser, 2010). Tailings which contain Rare Earth Elements (REEs) may turn out to be a sought-after resource (Falagán et al., 2017). It is because REEs are currently critical ingredients in high-tech industries (Mancheri, 2012). As more uses of REE are found, the industries' demand continues to grow. In 2011, the demand for REE exceeded supply, subsequently leading to a leap in price (Barakos et al., 2016). Paulick & Machacek (2017) suspected that it stimulated a boom in REE exploration.

Satellite remote sensing has demonstrated its usefulness for mineral exploration (Goetz et al., 1983). However, the potential use of remote sensing for REE exploration is still being evaluated by studying the spectral reflectance of REE-bearing mineral in the laboratory scale (e.g., Neave et al. (2016); Turner et al. (2016;2014); Wang et al. (2017)). Also, only research conducted by Rowan & Mars (2003) detected the absorption feature of REEs in their airborne remote sensing data because their study area included a stockpile of processed REE ore.

Targeting REE-bearing minerals with remote sensing can be a challenging task due to several reasons. Of all REEs, Neodymium (Nd), an REE pathfinder, exhibits narrow absorption features centred at ~583, ~744, ~802 and ~871nm (Neave et al., 2016). Neave et al. (2016) measured the spectral reflectance of REE-bearing carbonatite rocks in a laboratory setup and concluded that Nd absorption features appear when Nd concentration in their samples is more than 1000µg/g. However, such high Nd concentration is difficult to be encountered in Earth's surface.

Apart from being low in REE concentrations, REE-bearing rock is susceptible to chemical weathering, reducing REE concentration in it. Carbonatite, for examples, is known as the primary source of REEs and subject to chemical weathering (Chen et al., 2017). With the passage of time, REEs in Carbonate could be leached by water. In a case of tailings, the likelihood of leaching process taken places is even greater. It is because tailings are associated with acid materials and fine particles (Lottermoser, 2010). According to Myers (2013), acid condition and large surface area can increase the rate of the chemical process.

Another reason accountable for difficulty in targeting REEs with satellite remote sensing is the presence of iron. Iron also has absorption feature in the visible and near-infrared (VNIR) wavelength range (Ben-Dor et al., 1999). Further, iron is more abundant than REEs in the Upper Continental Crust (UCC) (Taylor & McLennan, 1995). A study conducted by Wang et al. (2017) exemplifies this case. In their study, iron oxide absorption features dominated their sample spectra, and REE absorption features were not detected - even though the total REE is as high as 1624.5µg/g.

In this study, tailing suspected to contain REEs were collected from abandoned tin mine sites in Bangka Island, Indonesia. REE concentrations in tailing samples were quantified, and the leachability of REE by water was tested. REE concentrations in the tailing samples were linked to variations in their spectral reflectance in the VNIR wavelength range. Iron concentration was also quantified to observe the effect of its presence in spectral variation. At the end of this study, spectral and spatial specifications of a satellite sensor for targeting REE containing tailings were defined.

1.2. Research objectives

The main objectives of this research was to characterize and derive spectral parameters of REE-absorption features and determine sensor specifications required to target REEs in tailings of abandoned mine sites on Bangka Island, Indonesia.

1. To investigate which REEs can be found in the study area and to quantify the concentration of REEs and iron using geochemical analysis.
2. To investigate absorption features related to REEs in the study area that can be detected using an ASD spectrometer.
3. To derive spectral parameters (depth, ratio, and area) of REE-absorption features and to relate changing shape parameters to different combinations of REE elements.
4. To investigate whether REEs within the surface soil are leachable by water.
5. To determine what sensor specifications are needed to detect REEs in the study area.
6. To evaluate which of currently available satellite sensors will qualify for detecting REEs in the study area.

1.3. Research questions

1. What REEs can be found in tailing samples?
2. How significant is the effect of water leaching on the total concentration of REE?
3. Which of REE absorption features can be detected in the VNIR wavelength range?
4. How do the absorption features in the VNIR wavelength range change with changing the concentration of REE?
5. What are spectral and spatial specifications needed for a sensor to detect REEs in this study area?
6. Which of currently available sensors qualify for detecting REEs in the study area?

1.4. Thesis structure

Chapter 1: Introduction

Chapter 2: Research background

Chapter 3: Material and Methodology

Chapter 4: Results

Chapter 5: Discussion

Chapter 6: Discriminating three absorption features

Chapter 7: Conclusion and Recommendation

2. RESEARCH BACKGROUND

2.1. Study area

The study area consists of three abandoned mine sites located in Bangka Island, Indonesia (Figure 1). The size of location 1, 2, and 3 is approximately 450m x 500m, 450m x 250m, and 750m x 500m respectively. Bangka Island has been mined for tin since 1711 (Ko, 1986). Hydraulic mining method was applied in the study area. This method utilizes pressurized water to disintegrate tin placer deposit into slurry. Then, the produced slurry is directed to the in situ sluice box. Based on differences in specific gravity, tin ore, which is heavy grain, ends up in the bed of sluice box, while other light grains are washed away. These washed away grains are directly dumped back into the mine pit and called tailings.

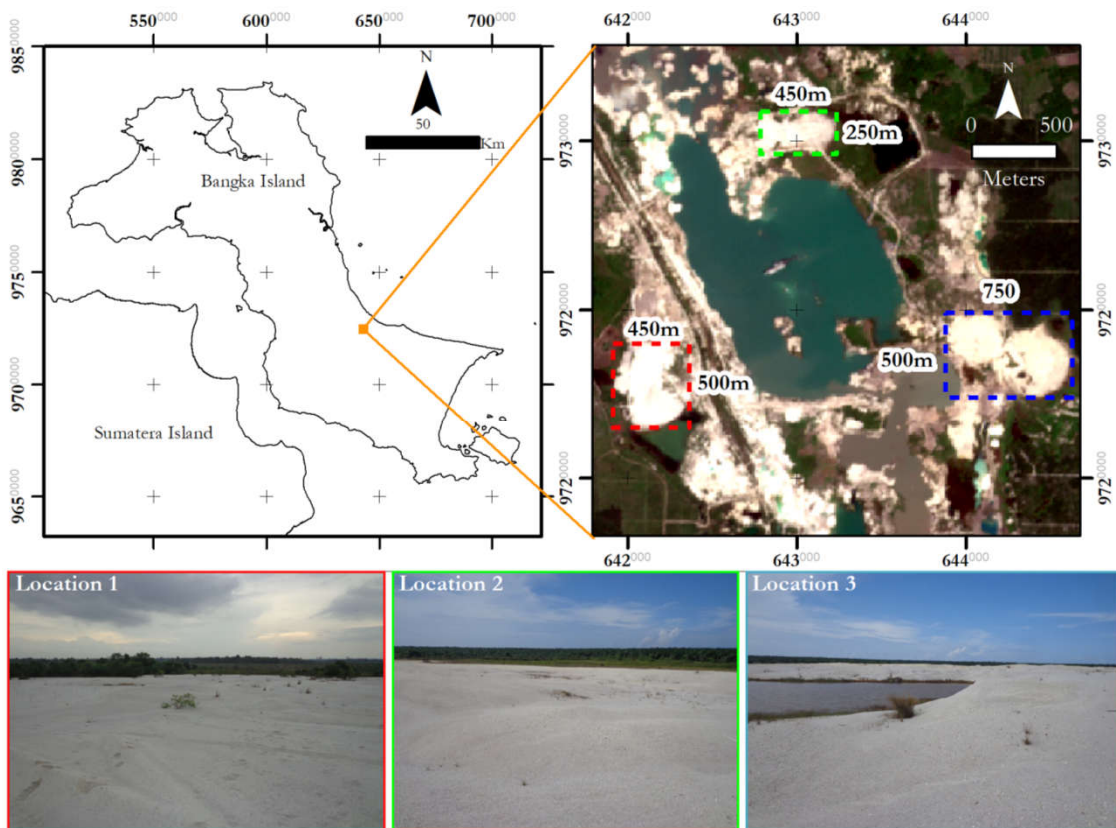


Figure 1 Top-Left: Orange box indicates the location of the study area. Top-Right: The boundary of location one (a red-dashed box), location two (a green-dashed box), and location three (a blue-dashed box) are shown with a natural colour Sentinel-2 MSI image as background. All areas, in fact, are tailings. The differences are that some areas are covered by water, and some are covered by vegetation. Bottom: Images from location one, two and three are displayed in order from left to right.

Tailings in Bangka Island are mainly Quartz grains (Narendra & Pratiwi, 2016). In the three abandoned mine sites, tailings mainly consist of coarse-grained sand ($>0.1\text{mm}$) (Appendix A). In these tailings, there is a possibility to contain REE; however, there is a paucity of literature concerning REE exploration in Bangka Island. To date, we only found a study of REE exploration in Bangka Island that was conducted by Szamalek et al. (2013). They revealed that tailings in Bangka Island contain REEs within Monazite ((Ce, La, Nd, Th)PO₄) and Xenotime (YPO₄), with an average of 3.93%wt and 2.48%wt respectively.

2.2. Rare earth elements

REEs refer to lanthanides in the periodic table including Lanthanum (La), Cerium (Ce), Praseodymium (Pr), Neodymium (Nd), Promethium (Pm), Samarium (Sm), Europium (Eu), Gadolinium (Gd), Terbium (Tb), Dysprosium (Dy), Holmium (Ho), Erbium (Er), Thulium (Tm), Ytterbium (Yb) and Lutetium (Lu) as well as Scandium (Sc) and Yttrium (Y). All REEs occur in nature except for Promethium (MacMillan et al., 2017; Massari & Ruberti, 2013).

REEs are divided into Light Rare Earth Elements (LREEs) including La, Ce, Pr, Nd, Sm, Eu, and Sc and Heavy Rare Earth Elements (HREEs) including Gd, Tb, Dy, Ho, Er, Tm, Yb, Lu, and Y (Haque et al., 2014). This classification was made because they have similar physical and chemical properties (Van Gosen et al., 2014). Because of these similarities, several REE-bearing minerals tend to be rich in LREEs or HREE. For example, Monazite (REE-PO₄) is composed primarily of LREE, and Xenotime (REE-PO₄) is composed primarily of HREE (Turner et al., 2016).

China is the World's leading country in the production of REE, monopolizing about 95% of the REE global market in 2003-2011 (Van Gosen et al., 2014), and still dominating the global supply by 85% in 2016 (USGS, 2017). In 2011, a surge in REE prices happened due to China's industrial policies on export quota (Wübbecke, 2013).

2.3. Existing studies on REE spectral reflectance

Adams (1965) studied spectroscopy of REE-bearing mineral five decades ago. However, only recently was a potential use of remote sensing technique for targeting REE-bearing minerals studied in lab scale or situ measurement. It is because mapping REEs-bearing minerals using satellite or airborne remote sensing data was supplementary to the main objective of the study (e.g., Rowan et al. (1995) and Bowers & Rowan (1996)).

Turner et al. (2014, 2016) studied in depth the spectroscopy of pure REE fluorocarbonate and phosphate minerals. Their study increased the number of spectroscopy data of REE-bearing minerals. In their study, probable origins of an absorption feature in the spectral reflectance of REE-bearing minerals were discussed.

Boesche et al. (2016), Boesche et al. (2015) and Boesche et al. (2015) used a different approach in investigating the spectroscopy of an REE-bearing outcrop. Instead of analysing the spectroscopy of the outcrop in the lab, they brought a hyperspectral camera. Then, the hyperspectral camera was positioned near the outcrop to scan it. Their study attempted to develop new technologies and algorithm to establish a link between exploration tools and hyperspectral mapping.

As reviewed by Turner (2015), the existing studies mainly focus on REE-rich carbonatite. For example, Rowan & Mars (2003) conducted a lithologic mapping study in the Mountain Pass, California using Advanced Spaceborne Thermal Emission and Reflection Radiometer (ASTER) imagery. They identified carbonatite complexes and noted that Nd³⁺ accounts for low reflectance in ASTER bands 1-3. In their study, they also extracted spectra of REE-bearing minerals as endmembers and classified REE mining area on their airborne image data acquired using the hyperspectral Airborne Visible-Infrared Imaging Spectrometer (AVIRIS) instrument.

In comparison, by using the same instrument but different locations, Rowan et al. (1995) and Bowers & Rowan (1996) were unable to extract a spectral signature of REE-bearing minerals as an endmember from AVIRIS images, even though they observed absorption features related to Nd³⁺ in laboratory spectra. Unfortunately, the authors did not explain the reason behind this. The similarity of these two studies is that they used fresh specimens during measurement in the laboratory.

A similar result was also reported by Bedini (2009) at an REE-mineralized Sarfartoq carbonatite complex using a hyperspectral airborne imaging sensor HyMap. Nd³⁺ related absorptions were observed in laboratory spectra but not in the HyMap image. The author suspected that the concentration of REE is the reason, but their study did not involve geochemical analysis.

In addition to the absorption feature of REE being difficult to detect using remote sensing technology, it is debatable whether absorption features related to REEs shift or not when their ions are attached to another mineral. Clark (1995) claimed it does not shift, but Turner (2015) argued this statement is false. In Wang et al. (2017) study, the peak of Nd absorption feature was at 796nm compared to 798nm obtained by Rodionova et al. (2015). Turner et al. (2014, 2016) studied spectroscopy of several pure REE-bearing minerals and reported that the absorption features related to Nd³⁺ could shift due to differences in the mineralogy and REE concentration of REE-bearing minerals.

3. MATERIAL AND METHODOLOGY

3.1. Material

3.1.1. Field samples

3.1.1.1. Natural water samples

To assess the concentration of REEs in natural water in the surrounding of the study area, ten 20ml bottles of natural water samples were taken from ponds in the vicinity of the study area (Appendix B). The bottles of natural water samples were also sealed with paraffin paper before taken to the laboratory.

3.1.1.2. Tailing samples

Tailing samples were taken by pushing a 2-cm deep, 2.2-cm diameter sample container into the surface (0-2cm) of three abandoned mine sites (Figure 2a). The reason why tailing sailing samples were taken at the surface is because VNIR satellite remote sensing is only able to acquire the spectral reflectance of tailings at the surface. Figure 2b exhibits the appearance of collected samples.

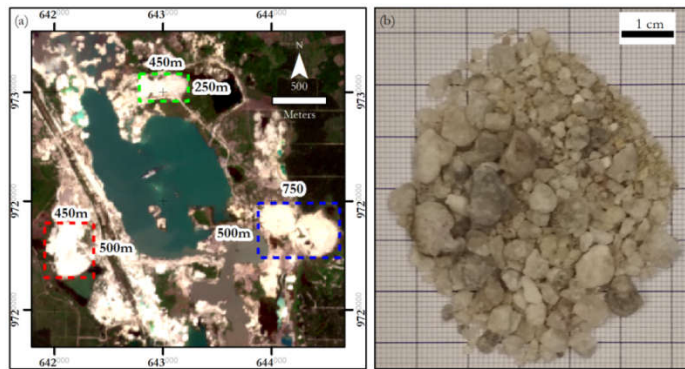


Figure 2 a) The boundary of location 1 (a red-dashed box), location 2 (a green-dashed box), and location 3 (a blue-dashed box) shown with a Sentinel-2 MSI natural colour image as background. b) The collected samples were loose material, and at a quick glance, the contents look like Quartz grains. The smaller grains were beneath the bigger grain.

From location 1, 69 tailing samples were taken according to a grid sampling pattern with 30m spacing. During preparation for the fieldwork campaign, we observed an absorption feature at band 5 (704nm) of Sentinel-2 MSI image (Figure 3). Because of this, five additional tailing samples were taken corresponding to the location of pixels that have the absorption feature at band 5 of the Sentinel-2 MSI image.

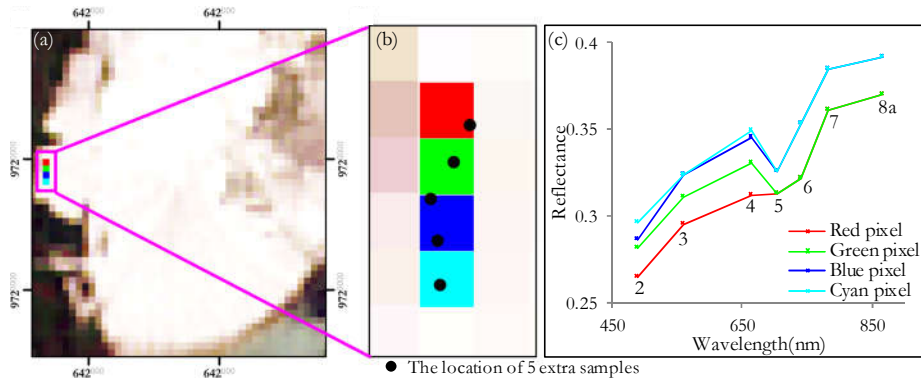


Figure 3 a) Subset of Sentinel-2 MSI natural colour image (shown in Figure 2a) showing location 1. b) A zoom-in view of region in (a), showing the position of 5 extra tailing samples (indicated by black dots) as well as pixels with absorption feature at band 5 of Sentinel-2 MSI image (indicated by red, green, blue, and cyan pixels). c) A graph plotting the spectral reflectance of the colour pixels displayed in (b). Numbers next to line graphs indicate band number.

From location 2, 45 tailing samples were taken according to a grid sampling pattern with 21m spacing. From location 3, 41 tailing samples were taken according to random sampling pattern. The choice of whether to follow a grid or random sampling pattern depended on the terrain condition of location 1, 2, and 3. The terrain of location 1 and 2 was relatively flat, thus allowing a grid sampling pattern. Meanwhile, location 3 consisted of undulating dunes. Therefore, a random sampling pattern was applied because applying a grid sampling pattern in location 3 was difficult. The distribution maps of taken tailing samples are shown in Appendix B.

In this study, tailing samples were divided into two data sets. The first data set is tailing samples from location 1. They were prepared for investigating the chemical composition and spectroscopy of the samples as received. Second, samples from combined location 2 and 3 were prepared for investigating a possibility that REEs are present in particular grain size. Figure 4 demonstrates the general treatments that were given to the tailing samples.

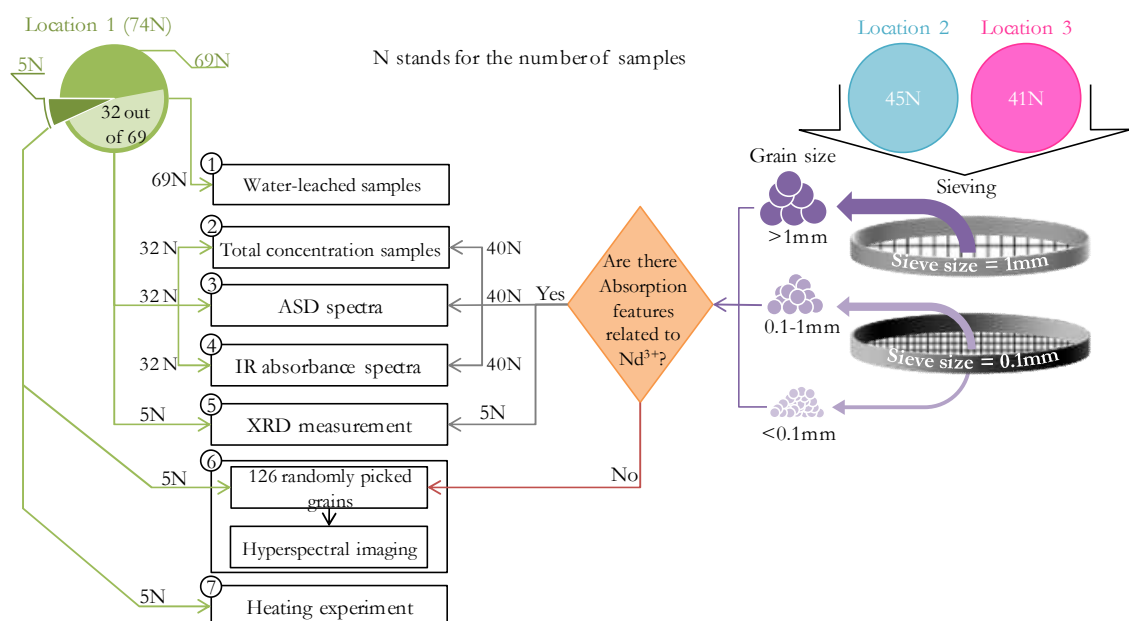


Figure 4 The collected tailing samples were divided into two data sets, namely samples from location 1, and samples from combined location 2 and 3. They were differently treated to fit their purposes, namely water-leached samples, total concentration sample, ASD spectra, Infrared absorbance spectra, X-ray Diffraction (XRD) measurement, Hyperspectral imaging, and Heating experiment.

From Figure 4, different treatments were given to tailing samples, and below are the details of the treatments (the following numbering refers to Figure 4):

1. Water-leached samples

Water-leached samples were prepared for investigating the leachability of REEs in tailing samples by water. This investigation is imperative because if water can mobilize REE leaving tailings, it will in turn cause depletion in REE concentrations. When this case is true, satellite remote sensing will not detect REEs, because no REEs remain in tailing. 69 tailing samples from location 1 were prepared for water-leached samples.

2. Total concentration samples

To determine the total concentration of REEs, tailing samples were fused using a borate fusion technique, and the product of the borate fusion technique is called “total concentration sample”. The total concentration of REEs was linked to variations in the VNIR spectral reflectance of tailing samples.

For location 1, 32 samples were prepared for total concentration samples. The 32 tailing samples were chosen based on an assumption that if REEs were present at higher area, then there should be REEs at lower area and these 32 samples were located at higher location than other samples in location 1.

For location 2 and 3, 40 tailing samples were prepared for total concentration samples. The 40 tailing samples were chosen following procedures; Firstly, tailing samples from location 2 and 3 were sieved and classified into three groups based on their particle sizes (big >1mm, medium 1-0.1mm, and small <0.1mm). These fractions were chosen as Szamalek et al. (2013) indicated that Xenotime and Monazite could be found in medium and small particle. Secondly, every sieved sample was scanned using ASD spectrometer, and the result can be seen in Appendix C. Lastly, 40 tailing samples with three Nd absorption features centred at 745nm, 801nm, and 873nm in their spectra were selected.

3. ASD spectra

The tailing samples that were prepared for the total concentration samples were also measured using ASD spectrometer. This measurement was done to acquire the VNIR spectral reflectance of tailing samples. The spectral variations in the obtained VNIR spectral reflectance were related to the concentration of REEs for investigating the origin of an absorption feature. Also, the obtained spectra were used for investigating the spectral capability of satellite remote sensing to target REEs by resampling the obtained spectra.

4. Infrared absorbance spectra

Fourier Transform Infrared - Attenuated Total Reflectance (FTIR-ATR) analysis was performed to acquire infrared absorbance spectra of the tailing samples that were prepared for the total concentration samples. FTIR-ATR was chosen because it measures functional groups. Also, it only requires a small amount of samples (about 0.1g).

5. XRD measurement

To investigate the mineralogy of tailing samples that were prepared for the total concentration samples, 5 samples from location 1 as well as 5 samples from location 2 and 3 were analysed using XRD technique. These numbers of samples were chosen because the amount of samples is not enough.

6. Hyperspectral imaging

To check the VNIR spectral reflectance of a single grain, 126 grains varied in shape, size, and colour were scanned by using a hyperspectral camera. These 126 grains were picked from tailing samples that were not used for preparing the total concentration samples.

7. Heating experiment

To check whether the absorption feature of collected tailing samples changes or not, 5 tailing samples were measured using ASD spectrometer while the tailing samples were being heated by a hot plate. These 5 tailing samples were taken corresponding to the location of pixels that have the absorption feature at band 5 of the Sentinel-2 MSI image (Figure 3).

This experiment was performed because Adams (1965) reported that radioactive REE-bearing minerals tend to experience metamictization. By heating an REE-bearing mineral, he observed changes in the spectral reflectance of his sample. Metamictization is a process in which the crystal structure of a mineral was totally or partially destroyed as a result of the decay of Uranium or Thorium.

3.1.2. A mixture of Quartz and Xenotime

In this study, the spectral reflectance of Xenotime was used as guidance in interpreting the spectral reflectance of obtained samples. Xenotime was chosen because it has absorption features centred at around 651nm related to Er as well as absorption features centred at around 744nm, 802nm and 871nm related to Nd, Sm, and Dy.

Before measurement, Xenotime was diluted by using Quartz. The justifications for diluting Xenotime were first to observe changes in the spectral reflectance of Xenotime as the proportion of Xenotime decrease and second to adjust REE concentrations in a mixture of Xenotime and Quartz comparable to REE concentrations in tailing samples. Quartz was chosen because it has weak to non-existent absorption in the VNIR wavelength range (Adams, 1965; Hunt, 1977), and also, obtained samples consist of quartz.

Quartz and Xenotime is obtained from the mineral showcase of ITC GeoScience laboratory. The total concentration of REEs in the mixture was quantified. The VNIR spectral reflectance of the mixture was measured using ASD spectrometer, and the mineralogy of Quartz and Xenotime was checked using XRD technique.

3.1.3. Satellite remote sensing images

This study only used a Landsat-8 OLI and Sentinel-2 MSI image as they are cloud-free data. An on-demand product of Landsat 8 OLI surface reflectance was ordered via EarthExplorer (<https://earthexplorer.usgs.gov/>), and the ID of the used Landsat 8 OLI is LC081230622017101401T1. Meanwhile, an on-demand product of Sentinel-2 MSI surface reflectance image was ordered via <https://s2.boku.eodc.eu/>. Compared to the on-demand of Landsat 8 OLI surface reflectance image which is readily used, the on-demand of Sentinel-2 MSI surface reflectance image is required to be downloaded and processed in RStudio using a Sentinel-2 package (<https://github.com/IVFL-BOKU/sentinel2>). The Sentinel-2 package is using the ESA's Sen2Cor algorithm. The final product of this processing is a bottom-of-atmosphere, atmospherically corrected Sentinel-2 image. The ID of the used Sentinel-2 image is S2A_MSIL1C_20171121T030011_N0206_R032_T48MXC_20171121T081729.

Figure 5 shows the band position of WorldView2, Sentinel-2 MSI, and Landsat 8 OLI and compares their spatial resolution. This figure only shows the band position and spatial resolution of WorldView2, Sentinel-2 MSI, and Landsat 8 OLI whose bands were used in this study. As shown in Figure 5b, the spatial resolutions of Sentinel-2 MSI band used in this study were 10m and 20m. To enable computation, the spatial resolution of the used Sentinel-2 MSI band was resampled to 10m with the nearest neighbour technique. The nearest neighbour technique was used because it does not change the pixel value.

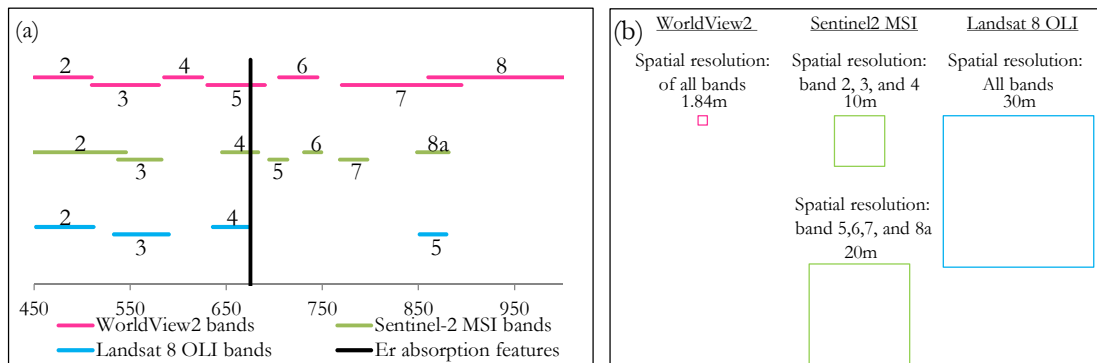


Figure 5 a) Showing the band position of WorldView2, Sentinel-2 MSI, and Landsat 8 OLI, indicated by horizontal color lines. Numbers above the horizontal lines indicated the number of the band. A vertical black line indicates the position of Er absorption features. b) A comparison between the spatial resolution of WorldView2, Sentinel-2 MSI, and Landsat 8 OLI.

3.1.4. Software used

The software used during this study is listed below:

1. RStudio

In this software, scripts were created to ease computation. This software was used for averaging the obtained VNIR spectral reflectance and correlating the VNIR spectral reflectance data and the total concentration of REEs. RStudio is free software that was downloaded via ITC software manager. All scripts that were created for this study can be found in Appendix D.

2. SPSS

This software was used for modelling the quantitative relationships between the VNIR spectral reflectance data and the total concentration of REEs. SPSS is commercial software, and the use of this software was under ITC license.

3. ENVI

This software was used for displaying the satellite remote sensing images. ENVI is commercial software, and the use of this software was under ITC license.

4. EVA (Bruker) software

EVA is software that is shipped with the Bruker D2 Phaser XRD. This software was used for help in interpreting the result of XRD.

3.2. Methodology

3.2.1. Sample preparation

3.2.1.1. Natural water samples

The preparation of natural water samples was done by filtering water samples using a 0.45 μ m filter. Filtering the water samples was aimed to avert clogging problems in ICP-OES.

3.2.1.2. Water-leached samples

To assess the leachability of REEs by water, 69 tailing samples from location 1 were used. The following describes the procedure of preparing leachability of REEs by water:

1. 69 tailing samples from location 1 were pulverized with a Retsch ball mill and sieving to <0.25mm.
2. 4 gram of each sample was mixed with 20ml of ultra-pure water produced by Direct-Q®3 UV.
3. Every mixture was stirred for 30 seconds and leached for 18 hours.
4. Liquid was extracted from every mixture by using a syringe equipped with a 45 μ m filter for ICP measurements.

3.2.1.3. Total concentration samples

To quantify the total concentration of REEs in the tailing samples using ICP-OES, the bond between REEs and other elements in the tailing samples must be broken, and all samples must be in liquid phase. To fulfil these conditions, a borate fusion technique was used. The following describes the procedure of fusing the samples:

1. The samples of location 2 and 3 were pulverized with a Retsch ball mill and sieving to <0.25mm. The samples of location 1 were already pulverized when preparing water-leached samples.
2. 0.1gr of each pulverized sample was mixed with 0.8gr of an X-Ray flux, a mixture of 66% Li tetra- and 34% meta-borate (made by XRF Scientific Europe SPRL) in a platina crucible.
3. The platina crucible was held for 6 minutes at 1150°C inside the xrFuse 2 machine. These 6 minutes were divided into 3 minutes for melting the samples and 3 minutes for homogenizing melted samples by shaking the crucible.
4. Then, the melted sample was dissolved in 50ml of 10% (v/v) supra pure HNO₃, ready for quantifying the total concentration of REEs in ICP-OES. Each sample was duplicated.

3.2.1.4. ASD, FTIR-ATR, and XRD measurements

To perform ASD, FTIR-ATR and XRD measurements, the samples of location 1, 2, and 3 were pulverized and sieved <0.25mm.

3.2.1.5. Hyperspectral Imaging

126 grains were randomly picked from 5 extra tailing samples of location 1 and not-selected samples from location 2 and 3. The 126 grains were placed on 4 sheets of black paper. The arrangement of the 126 grains can be seen in Appendix E.

3.2.1.6. Heating experiment

The 5 extra tailing samples were not pulverized to keep their condition as received. They were contained in a watch glass before measurement.

3.2.2. Data acquisition

3.2.2.1. Chemical composition

The chemical composition of liquid samples was analysed with a Perkin Elmer 8300DV ICP-OES. The calibration standards for natural water sample and water-leached sample were prepared by diluting a multi-REE standard solution with ultra-pure water produced by Direct-Q® 3 UV. Meanwhile, the calibration standards for total concentration samples were made by diluting a multi-REE standard solution with 10% (v/v) HNO₃ and 1.6gr (w/v) flux (1.6gr in 100ml). Multi-element (Mg, Ca, Al, and Fe) calibration standards were made by diluting a multi-element standard solution with ultra-pure water. The standard solution was TraceCERT reference material. Quality control was performed by measuring two known REE concentration solutions measured at the middle and end of sample measurement.

In ICP-OES, the quantification of chemical elements was done by detecting the intensity of emission of a particular element at wavelengths characteristic of that element. However, determining wavelength for REEs is challenging because the signal intensities of REEs interfere among themselves (Makombe et al., 2017; Navarro et al., 2002). Zuleger & Erzinger (1988) recommended to use the most sensitive wavelength line, but this line experienced severe interferences specially at samples that have a low concentration of REE (Eid et al., 1994). To decide which wavelengths were used, several candidate wavelengths were tested by measuring calibration standards. Candidate wavelengths which experienced less interference were used for quantifying signal intensities measured in ICP-OES.

Figure 6 illustrates how the signal intensity of REEs appears. Table 1 summarizes the used wavelengths for ICP-OES determination. The Limits of Detection (LOD) were 0.001µg g⁻¹ for water and leached samples and 5µg g⁻¹ for total concentration samples.

Table 1 The list of candidate and used wavelengths for REEs

Elements	Code	Wavelength	Elements	Code	Wavelength	Elements	Code	Wavelength
Sc	C1*	357.253	Sm	C1*	442.434	Er	C1*	337.271
	C2	361.383		C2	359.260		C2	339.200
Y	C1*	371.029	Eu	C1*	381.967	Tm	C1	313.126
	C2	324.227		C2	412.97		C2	346.220
La	C1*	379.478	Gd	C3	393.048	Yb	C1*	328.937
	C2	408.672		C1*	335.047		C2	369.419
	C3	407.735	Tb	C1*	350.917	Lu	C1*	261.542
	C4	384.902	Dy	C1*	353.170		C2	291.139
Ce	C1*	413.764		C2	394.468	Pr	C3	219.554
	C2	418.66	C3	396.839	C1		414.311	
Nd	C1*	430.358	Ho	C1*	345.600	Tm	C1	313.126
	C2	406.109		C2	339.898		C2	346.220

* indicates a wavelength that was used to quantify the signal of REEs in ICP-OES.

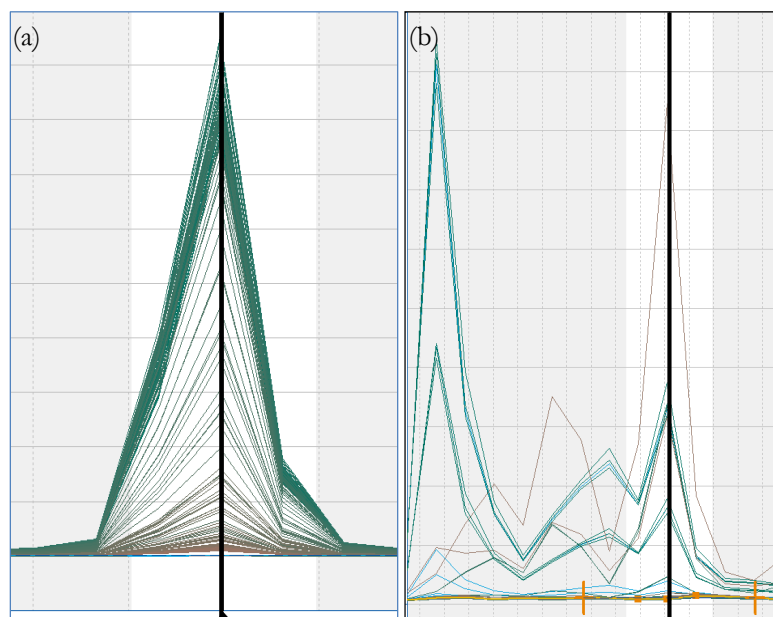


Figure 6 Graphs illustrating the signal intensity of element being measured in ICP-OES. A black vertical line in both graphs indicates the peak position of the corresponding element being measured. a) The signal intensity for Silicon without interferences. When measuring heavy metal, silicon, or other elements, except for REEs, the signal intensity will have a nice peak with the same pattern and peak position. The height of the peaks is varied according to the concentration of corresponding element being measured. The higher concentration is, the higher the peak will be. b) The signal intensity for Lanthanum with severe interferences. There is more than one peak in the vicinity of Lanthanum peak, and these peaks are the peaks of other REEs which interfere each other signal.

3.2.2.2. Spectral reflection data

Pulverized samples were contained in a 40x15mm dish and their VNIR spectral were measured in a dark room using an ASD FieldSpec 3 with a high-intensity contact probe. The spectrometer has three detectors covering the VNIR (350-1000), SWIR1 (1000-1800), and SWIR2 (1800-2500) wavelength ranges. Every sample was measured six times using the contact probe which has an internal light source, and the sample being measured was shaken in between the measurements. To process the obtained spectra, a script was created in RStudio software. The created script automatically calculated the mean spectra of a sample. Repeated measurements and shaking the sample in between measurements were performed to compensate for compositional heterogeneity on the sample.

3.2.2.3. FTIR-ATR analysis

Before measuring infrared absorbance of each pulverized sample, the probe and crystal of FTIR-ATR were cleaned, and background measurement was run. FTIR-ATR analysis was performed using a Bruker Vertex FTIR spectrometer equipped with Pt-ATR-diamond accessory. The range of FTIR-ATR analysis was between 4000cm^{-1} to 600cm^{-1} . The resolution and sample scan time are 4cm^{-1} and 16 scans respectively.

3.2.2.4. XRD analysis

Pulverized sample were put in XRD specimen holder. XRD measurements were carried out on a Bruker D2 Phaser XRD. 2θ was started from 6 to 80 degrees with an increment of 0.012° . The effective total time was set at 662.5seconds, and the measurement was repeated. Divergence slit, knife, and detector slit were adjusted at 1mm, 1mm, and 8mm respectively. EVA software was used to interpret the result of measurement.

3.2.2.5. Hyperspectral camera imaging

A total of 126 grains were scanned using a SPECIM hyperspectral camera to investigate the spectral reflectance of a single grain. The camera was measured in a VNIR (350-1000) wavelength range with 768 bands and 110 μ m pixel resolution. A Region of Interest (ROI) was drawn inside each grain to calculate the mean spectra of each sample. A filter with a width of 30 bands or 46nm was applied to smooth the mean spectra in ENVI software.

3.2.2.6. Heating experiment

The spectral reflectance of the 5 extra samples was measured using ASD spectrometer; however, only an absorption feature centred at around 674nm were observed. Heating the 5 extra samples was a method for confirming the possibility of the 674nm absorption feature undergoing a band shift to around 705nm or a possibility of appearing a new absorption feature at around 705nm. Every sample was measured using ASD spectrometer while it was being heated by a hotplate at the same time. The maximum temperature was set at 50°C. It was because the temperature of tailing during daytime in the field was almost 50°C.

3.2.3. Data analysis

3.2.3.1. Identifying anomaly of REE concentration

In nature, the distribution of REEs follows the Oddo-Harkins rule, which appears to be a zigzag pattern in a diagram of REE concentrations as shown in Figure 7 (Ramos et al., 2016). The Oddo-Harkins rule states that an even atomic number (Ce, Nd, Sm, Gd, Dy, Er, and Yb) are more abundant than elements with an odd atomic number (La, Pr, Eu, Tb, Ho, Tm, and Lu). To detect anomaly concentrations, REE concentrations are plotted after normalization to chondritic abundance (O'Neill, 2016). Chondritic abundance refers to the theoretical abundance of an element date back to when the universe is formed (Rollison, 1993).

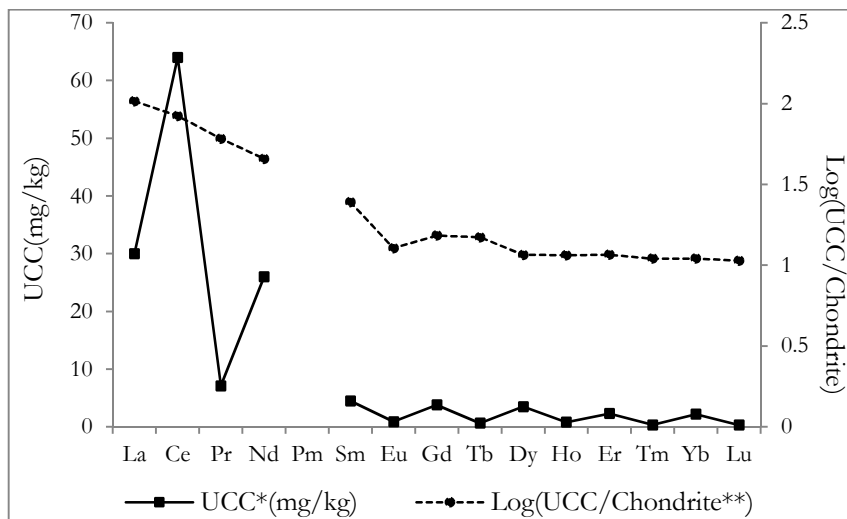


Figure 7 REE concentration in the UCC and chondrite normalization of REE in UCC. Data source: (*) from Taylor and McLennan (1995) and (**) from Anders and Grevesse (1989)

3.2.3.2. Derivation of spectral parameters

In deriving spectral parameters, three spectral parameters were defined, namely, band ratio, absorption band depth, and absorption band area. A script was created in RStudio to compute the spectral parameters. In this study, we observed two absorption features centred at around 500nm and 674nm, and they were explored further by calculating spectral parameters.

In the 500nm absorption feature, the band ratio is the value of band 550 divided by the value of band 500. The band depth is the depth of the absorption feature at band 500, and the band area is the area under curve of continuum-removed spectral reflectance between 450nm and 550nm. Band 450nm and 550nm were chosen as the left and right continuum interval because at these bands no absorption was observed. Band 500nm was chosen as variable in the band ratio and the band depth because it is the deepest depth of absorption feature of the 500nm absorption feature that we observed in this study. Also, among bands in the 500nm absorption feature, it has the strongest correlation with Fe and Er in our data set.

In the 674nm absorption feature, band ratio is the value of band 712 divided by the value of band 600. The band depth is the depth of the absorption feature at band 674, and the band area is the area under curve of continuum-removed spectral reflectance between 600nm and 712nm. Band 600nm and 712nm were chosen as the left and right continuum interval because at these bands no absorption was observed. Band 674nm was chosen as variable in the band ratio and the band depth because it is the deepest depth of absorption feature of the 674nm absorption feature that we observed in this study. Also, among bands in the 674nm absorption feature, it has the strongest correlation with Fe and Er in our data set.

Band ratio is a straightforward method to detect the presence of diagnostic absorption feature by dividing one band with another band. Band ratio used original spectra because it is designed to detect diagnostic absorption features while minimizing spectral variation due to albedo (Crowley et al., 1989; Rowan et al., 1974).

To compute band depth and band area, obtained spectra were normalized first by applying a continuum-removal technique proposed by (Clark et al., 1987). This normalization is important because the obtained spectra tended to show variation in overall reflectance. After normalization, the obtained spectra will have the same based line. As illustrated in Figure 8a, four spectra shows variation in overall reflectance, and after continuum-removed, they have the same based line at 1.

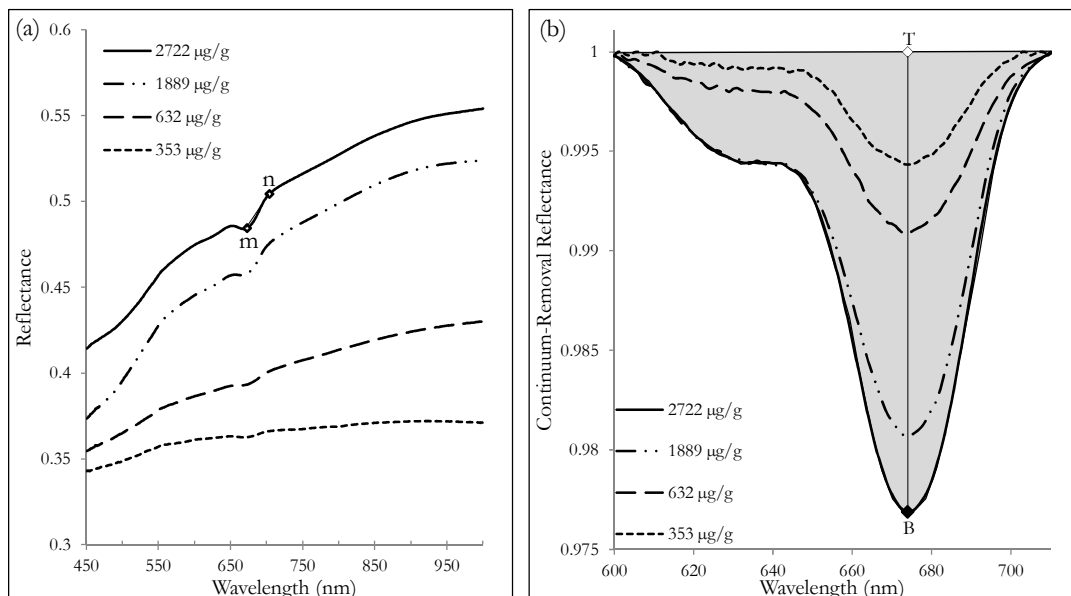


Figure 8 Spectral variations in sample spectra in the VNIR wavelength range with Er concentration ranging from 353 to 2722µg/g. a) Band ratio is a ratio between the reflectance values at 712nm and 674nm. b) Band depth (T, B) is the distance between T and B, and band area is the grey shaded colour.

3.2.3.3. Statistical analysis

To explore the possible correlation between REE concentration and all absorption features in obtained spectra, the obtained spectra were continuum-removed, and the depth of absorption features was calculated. A correlation value between the depth of absorption features and REE concentrations was defined using Pearson correlation coefficient with a 99% confidence level (2-tail). A script was created in RStudio to compute the correlation value.

Stepwise and enter multiple linear regression analyses were performed in SPSS software to observe the quantitative relationship between spectral parameter values and REE concentrations. In stepwise multiple linear regression analysis, a number of multi regressions were performed to remove spectral parameters that have the weakest correlation and keep the spectral parameters that explain the distribution best. In enter multiple linear regression, all spectral parameters are forced to be in the model. Residual Prediction Deviation (RPD) and the coefficient of determination (R^2), and were selected to evaluate the accuracy of the two multiple linear regression. In a model with high accuracy, R^2 should be as close as to 1 (Camacho-Tamayo et al., 2014). An RPD value of 10 or greater is excellent in predicting whereas an RPD value of 1 means that a model is not capable of predicting accurately (Williams & Sobering, 1993).

Samples whose REE concentrations were below Limit of Detection (LOD) were removed from the computation of statistical analysis. Removing these data lead to loss some information. Nevertheless, it is better to avoid fabrication because substituting values below LOD with zero, one-half the detection limit, or the limit itself is a flawed method (Helsel, 2010). To assess homogeneity between duplicated samples, the precision between REE concentrations in a pair of duplicated samples were calculated using a relative percentage difference proposed by Popek (2013).

3.2.4. Evaluating the feasibility of targeting REEs using satellite remote sensing

3.2.4.1. Resampling laboratory spectra

To evaluate whether REE absorption features are detectable or not by satellite remote sensing sensors, the obtained spectra were resampled to Landsat 8 OLI, Sentinel-2 MSI and WorldView2 spectral resolution using the “hsdar” package in RStudio. This package incorporated the spectral response functions of Landsat 8 OLI, Sentinel-2 MSI and WorldView2. Regarding spatial resolution, satellite remote sensing images were plotted to display the study area, and the pixel size of the images was visually evaluated to the size of the study area.

Band ratio, band depth, and band math derived from resampled spectra were used to target an absorption feature related to REE. The linear correlation between spectral parameters and REE concentrations was defined using Pearson’s correlation coefficient.

Band ratios were calculated by dividing the value of M by the value of N as illustrated in Figure 9a. Band ratio used the resampled spectra directly without applying continuum removal because band ratio already minimized the effect of albedo (Crowley et al., 1989; Rowan et al., 1974). Meanwhile, a continuum-removal technique proposed by (Clark et al., 1987) was applied to the resampled spectra before computing band depth and math. Applying the continuum-removal technique was necessary to normalize different albedo in resampled spectra. Band depth was the different value between the values of T and B, and band math was calculated by $(L-B)/(R-B)$ as illustrated in Figure 9b. After applying continuum-removal, the value of T was expected to be 1. B, L, and R refer to the value of band B, L, and R respectively in continuum-removed, resampled spectra.

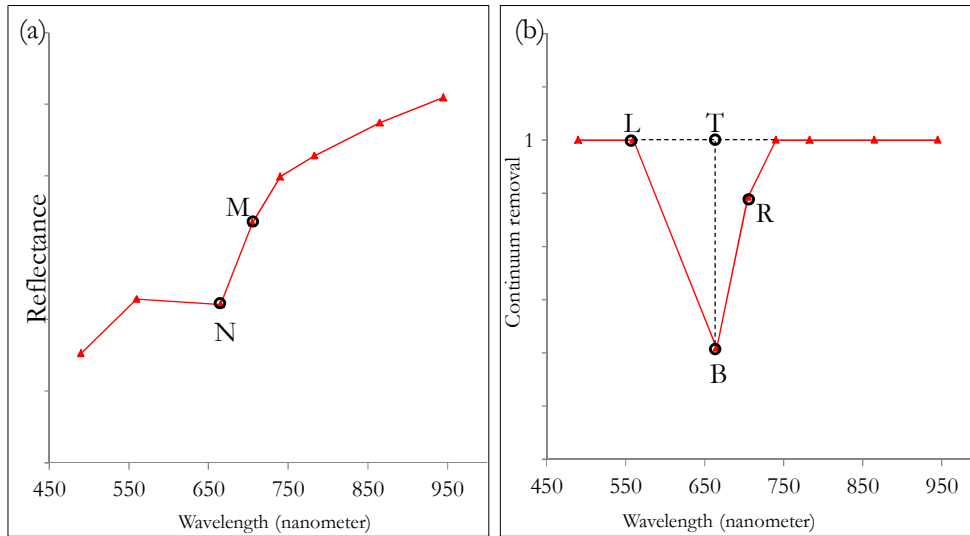


Figure 9 Illustration of calculating band ratio, band depth, and band math. a) Band ratio was calculated by divided M by N. b) Band depth was the distance between T and B, while band math was calculated by $(L-B) \times (R-B)$

3.2.4.2. Identifying possible satellite remote sensing sensors

The spectral reflectance of obtained samples showed an absorption feature centred at 674nm. Because of this, three satellite remote sensing sensors were suspected to be capable spectrally of discriminating the absorption feature because they have a band that lays in the absorption feature. The three satellite remote sensing sensors are WorldView2, Sentinel-2 MSI, and Landsat 8 OLI.

3.2.4.3. Masking satellite remote sensing images

Normalized Difference Vegetation Index (NDVI) was used to mask vegetation area in the images as vegetation has the same spectral reflectance with the spectral reflectance of the obtained samples. Vegetation areas in location 1 and 3 were used to calibrate the threshold for NDVI. Below is the NDVI formula:

$$NDVI = \frac{(NIR - Red)}{(NIR + Red)}$$

Where NIR is the value of band 7 for Sentinel-2 image and band 5 for Landsat 8 OLI image, and Red is the value of band 4 for both Sentinel-2 MSI and Landsat 8 OLI images.

Sentinel-2 MSI band 8a and Landsat 8 OLI band 5 were used to mask water area. These bands were chosen because they lay in infrared wavelength range. In this range, most of the sunlight is absorbed, so that water has a low value of reflectance. Water area in location 3 was used to calibrate the threshold for masking water.

3.2.4.4. Targeting Er absorption features using satellite remote sensing images

To identify a pixel with an absorption feature at band 4 of Landsat 8 OLI and Sentinel-2 MSI images, an RGB colour composite of band ratio, band depth, and band math was generated. A linear stretch was applied to the colour composite image. Pixels with a high value of band ratio, band depth, and band math were pixels with the highest possibility to have an absorption feature at band 4.

3.2.4.5. Targeting absorption features at band 5 and 6 in Sentinel-2 MSI image

In addition to the absorption feature at band 4 of Sentinel-2 MSI image, two absorption features at band 5 and band 6 were observed. To discriminate the three absorption features, band math with improvement was used to target an absorption feature. It was improved because it can give a false indication when it is used solely (Previously, band math was combined with band ratio and band depth to target one absorption feature, and the improved band math was enough to target one absorption feature). To overcome this false indication, band math was defined as the equation below:

$$\text{band math} = \begin{cases} \text{Not available} & \text{If } L < B \text{ and } B > R \\ (L - B) \times (R - B) & \text{otherwise} \end{cases}$$

where L and R are bands on the left and right shoulders of absorption feature. B is the peak band of absorption feature, as illustrated in Figure 9b. Not available value will be given if the value of B is higher than that of L and R.

4. RESULTS

4.1. Chemical composition

69 samples from location 1 were leached by water in the laboratory to assess the leachability of REEs by water. The concentration of REEs in water-leached samples and natural water samples are summarized in Table 2.

Table 2 The concentration of REE in water-leached samples from location 1 and natural water samples taken from the surrounding study area. Bold-style numbers indicate mean REE concentrations.

Elements	Natural water samples ($\mu\text{g/L}$) $\Sigma\text{N}=10$				Water-leached samples ($\mu\text{g/kg}$) $\Sigma\text{N} = 69$			
	Min	Max	Mean	N > LOD	Min	Max	Mean	N > LOD
Sc	5.65	5.92	5.77	10	14.44	70.97	25.94	69
Y	1.65	5.16	2.05	10	3.31	4.54	3.5	69
Ce	2.12	14.71	4.34	10	LOD	6.62	2.96	59
Nd	1.28	5.16	2	10	LOD	5.02	2.36	61
Sm	3.35	5.79	4.22	10	18.32	30.28	25.43	69
Eu	1.79	1.89	1.82	10	2.68	3.21	3.06	69
Dy	1.5	2	1.71	10	LOD	1.38	0.63	5
Ho	1.55	1.98	1.72	10	LOD	LOD	LOD	0
Er	1.09	3.83	1.98	10	2.12	29.52	6.93	69
Yb	1.68	1.94	1.74	10	1.08	3.2	2.6	69
Lu	1.57	1.64	1.6	10	3.31	40.2	11.91	69

Based on the mean values, REE concentrations in water-leached samples are higher than natural water samples, except for Dy and Ho concentrations that are lower. LOD is less than $1 \mu\text{g kg}^{-1}$.

Table 2 summarizes a small fraction of REEs that were carried away by water; however, the rest fraction of REEs was still bound by other elements in a solid phase that water was not able to break this bond. To quantify the total concentration of REEs, another sample treatment was performed by using the borate fusion technique to break the bond between REEs and other elements. The results of the total concentration of REEs are summarized in Table 3.

Table 3 REE concentrations in total concentration samples. Many REEs are below LOD ($< 5 \mu\text{g g}^{-1}$). Bold-style numbers indicate the mean concentration of Nd, Sm, Dy, and Er.

REE concentration	Location 1 $\Sigma\text{N} = 32$ (unit in $\mu\text{g/g}$)				Location 2 and 3 $\Sigma\text{N} = 40$ (unit in $\mu\text{g/g}$)			
	Min	Max	Mean	N > LOD	Min	Max	Mean	N > LOD
Sc	12.2	98	33.0	32	LOD	238	36.2	37
Y	7.48	260	52.3	32	LOD	256	51.5	26
La	LOD	99.5	28.4	28	LOD	5502	285	24
Ce	LOD	197	60.6	30	LOD	10700	368	39
Nd	LOD	62.1	20.1	16	LOD	3903	150	34
Sm	LOD	7.5	6.98	2	LOD	687	119.0	7
Eu		LOD		0	LOD	16.3	16.3	1
Gd		LOD		0	LOD	297	113.1	3
Tb	LOD	11.8	8.52	3	LOD	24.0	11.4	5
Dy	LOD	17.0	11.6	7	LOD	119	23.3	12
Ho		LOD		0	LOD	13.3	13.3	1
Er	286	2884	1005	32	112	3768	667	40
Yb	LOD	13.4	8.58	5	LOD	29.1	12.8	7
Lu		LOD		0	LOD	7.82	6.62	2

Nd, Sm, and Dy concentrations in the samples of location 2 and 3 are higher compared to the samples of location 1. This high concentration of Nd, Sm, and Dy is the result of the selection which is based on Nd absorption features. Er concentration exceeds LOD in all samples, and the mean value of Er in the samples of location 1 is higher than the samples of location 2 and 3.

Figure 10 compares the mean concentrations of REEs in water-leached samples and total concentration samples from location 1. In general, the mean concentrations of total concentration samples were 200 times or higher than the mean concentration of water-leached samples.

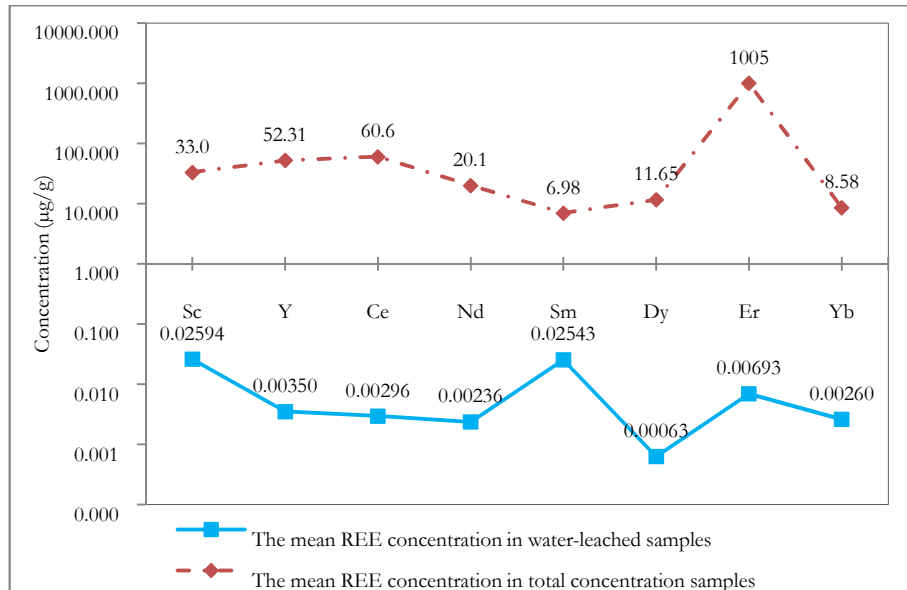


Figure 10 A comparison between the mean REE concentrations of water-leached REEs and total concentration samples from location 1. The mean REE concentrations in total concentration samples are 200 times or higher than in water-leached samples. For examples, the mean Er concentration in total concentration samples 1005µg/g, compared to 0.00693µg/g for Er concentration in water-leached samples, while the mean concentration of Sm is 6.98µg/g for total concentration samples compared to 0.025µg/g for water-leached samples.

To identify possible concentration anomalies, REE concentrations were normalized to chondrite values provided by Anders and Grevesse (1989) and compared to UCC provided by Taylor et al. (1995) and mean concentration of Mount Pass concentrates (Castor, 2008). Figure 11 indicated enrichment of mean REE concentrations in samples compared to UCC. Also, a distinct anomaly was shown by Er concentration in the samples that exceeded the Er concentration in the processed ore of Mount Pass deposit.

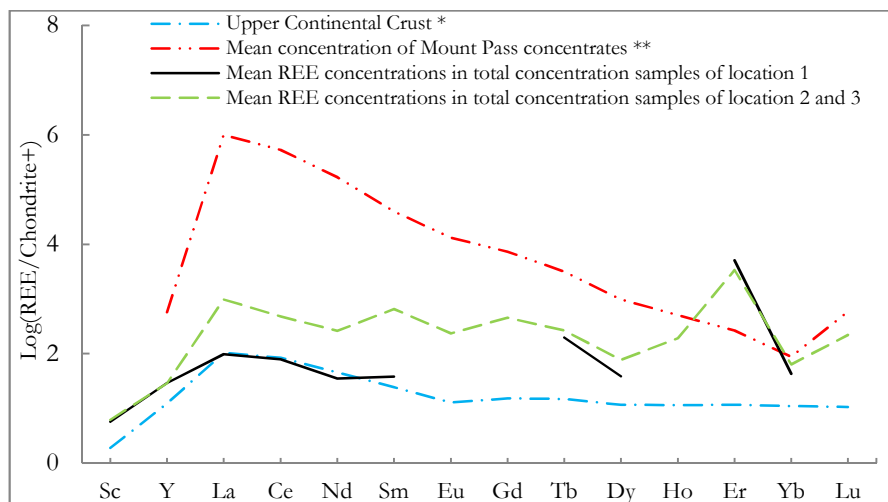


Figure 11 Chondrite-normalized REE distribution of mean REE concentrations in total concentration samples compared to the upper continental crust and the mean concentration of Mount Pass concentrates. Er concentration in total concentration samples exceeds Er concentration in processed REE ore from Mount Pass REE mining. Data sources: (†) from Anders and Grevesse (1989), (‡) from Taylor and McLennan (1995), (**) from Castor (2008).

Iron concentration and other major elements (Mg, Ca, and Al) were analysed because iron oxide is commonly found in soils and has absorption features in the VNIR wavelength range (Ben-Dor et al., 1999). Table 4 summarized the concentration of major elements found in the Earth's crust. Compared to the mean concentration of Er (1005 $\mu\text{g/g}$) in total concentration samples of location 1, only Al and Fe concentrations in the samples of location 2 and 3 were high and other elements were significantly low.

Table 4 The concentrations of major elements. The mean concentrations of Mg, Ca, Al, and Fe was significantly low. Bold-style numbers indicate the highest mean concentration.

Elements unit in $\mu\text{g/g}$	The samples of location 1 ($\Sigma N = 32$)			The samples of location 2 and 3 ($\Sigma N = 40$)		
	Min	Max	Mean	Min	Max	Mean
Mg	1.91	28.9	10.6	20.2	456	148
Ca	33.1	75.6	42.0	86.5	462	261
Al	21.5	1141	317	833	14451	4562
Fe	9.40	167	57.8	135	3839	897

The highest mean value is 4565 $\mu\text{g/g}$ for Al concentration and 897 $\mu\text{g/g}$ for Fe concentration in total concentration samples of location 2 and 3, and the mean value for other major elements is lower than the 1005 $\mu\text{g/g}$ which is the mean concentration of Er in total concentration samples of location 1 (Table 3).

A total of 72 samples were analysed using FTIR-ATR technique. The infrared absorbance spectra of the samples were compared to published infrared absorbance spectra by Lafuente et al. (2015) and matched with Quartz absorbance spectra. Ten randomly-picked samples were analysed using XRD technique, and their diffractogram was matched with the diffractogram in the database of EVA (Bruker) software. All samples had the same peak positions Quartz, only varied in intensity. Figure 12 shows the diffractogram and infrared absorbance spectra of the samples.

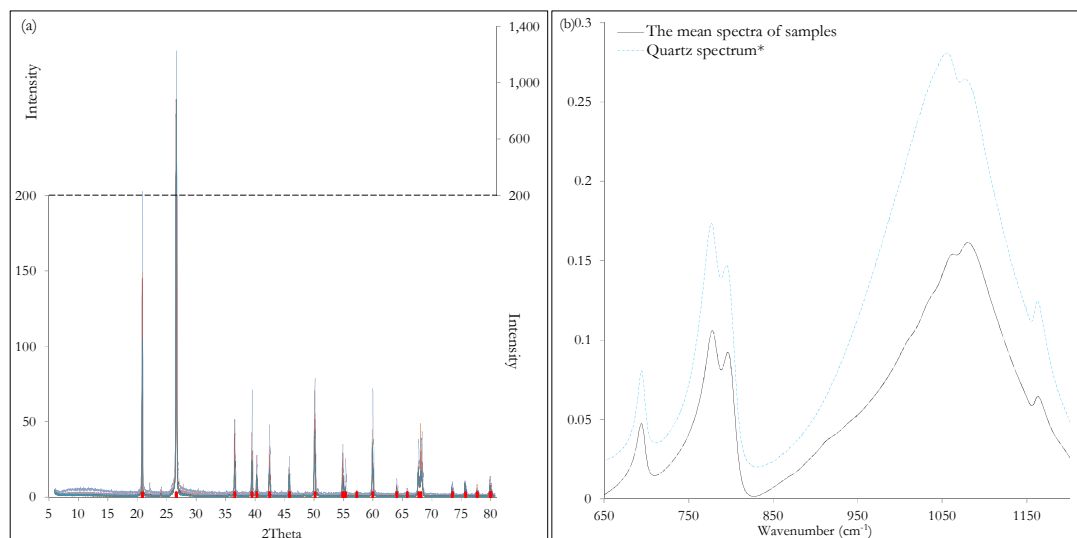


Figure 12 a) Showing the diffractogram of 10 samples. The peak positions of quartz are indicated by red bars that match with the peak positions of the sample. b) The mean FTIR-ATR infrared absorbance spectra of a sample compared to that of Quartz. Data sources: (*) from Lafuente et al. (2015).

4.2. Spectral reflectance data

The VNIR spectral reflectance of a mixture of Quartz and Xenotime was used as a help in interpreting the spectra of obtained samples. Figure 13 the VNIR spectral reflectance of a mixture of Quartz and Xenotime, and their REE concentrations are tabulated in Table 5. As can be seen from Figure 13 and Table 5, the depth of these absorption features decreased as REE concentrations in the mixtures decreased.

Table 5 REE concentrations in the mixture of Quartz (Q) and Xenotime (X). The numbers inside the brackets next to the letters indicates the proportion of Quartz and Xenotime in the mixture

Element unit in $\mu\text{g/g}$	Q(95):X(5)	Q(99):X(1)	Q(99.5):X(0.5)	Q(99.7):X(0.3)
Sc	21.8	27.5	14.3	12.1
Y	9248	4846	2222	1769
La	2047	1087	536	468
Ce	4414	2303	1073	928
Nd	1780	939	453	395
Sm	550	303	131	110
Eu	2.14	1.15	0.67	0.54
Gd	796	426	190	153
Tb	197	107	51.6	41.1
Dy	1387	751	370	302
Ho	355	182	82.6	67.4
Er	1532	938	562	479
Yb	1096	578	290	219
Lu	161	85.3	39.6	32.0

The concentrations of REE in the mixture decrease as the amount of xenotime in the mixture reduces.

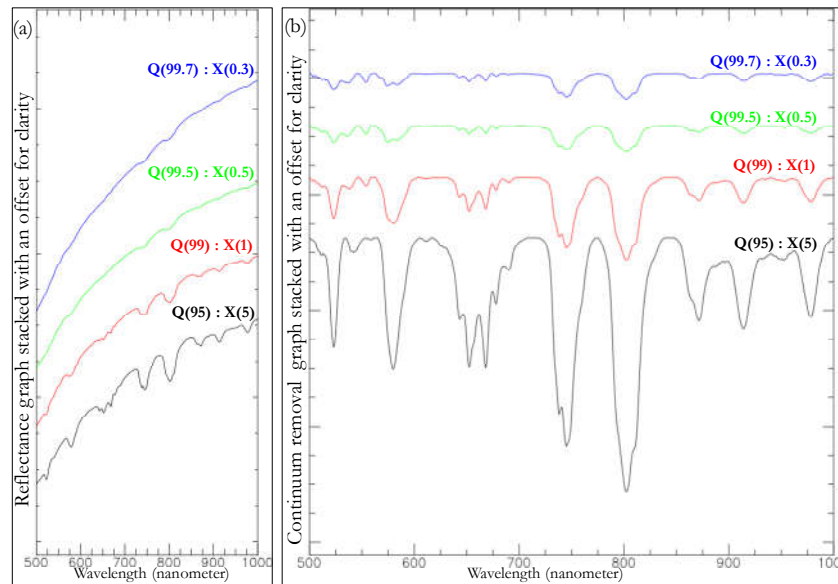


Figure 13 a) The spectral reflectance of a mixture of Quartz and Xenotime. The letters, “Q” and “X”, stand for Quartz and Xenotime respectively. The numbers inside the brackets next to the letters indicates the proportion of Quartz and Xenotime in the mixture. b) The depth of absorption features decreases as the proportion of Quartz increases. Absorption features centred at around 740nm, 802, and 871nm are due to Nd, Sm, and Dy, while absorption features centred at 651nm was due to Er (Turner et al., 2016). REE concentrations of the mixture are shown in Table 5.

The mean VNIR spectra of samples are shown in Figure 14. As mentioned by Neave et al (2016) and Turner et al (2016), in Monazite and Xenotime VNIR spectra, absorption features centred at ~ 583 , ~ 744 , ~ 802 and ~ 871 nm are related to Nd, Sm, and Dy, while absorption features centred at ~ 651 are related to Er. These features are noticeable at the spectra of the mixture; however, such features are not present in the sample spectra. Instead, an absorption feature centred at 674nm was found in sample spectra.

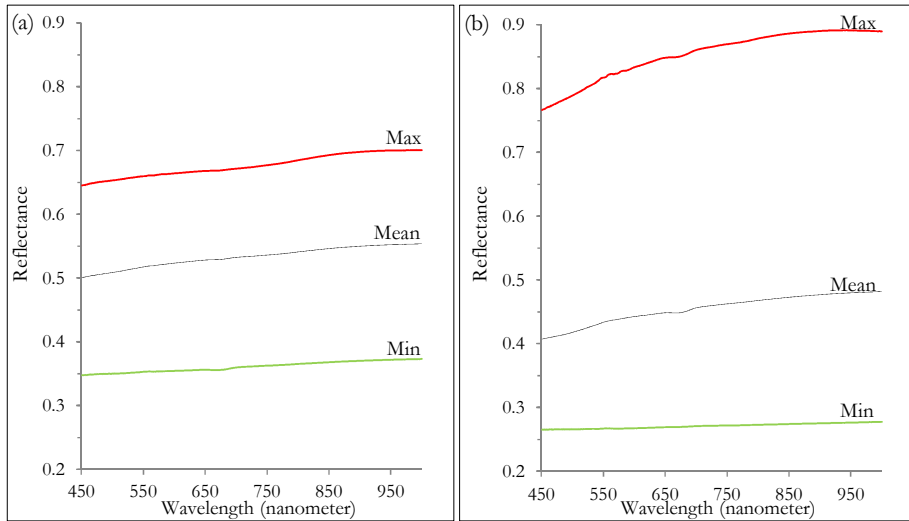


Figure 14 The min, mean, and max spectra of the samples of location 1(a), and location 2 and 3 (b) An absorption feature is visible centred at 674nm.

To observe the effects of grinding samples during preparation on their spectra, the mean spectra of the samples from location 2 and 3 before and after grinding were plotted in Figure 15. The absorption feature centred at 674nm appears deeper in the spectra of the samples before grinding than after grinding. However, the spectral albedo of the samples after grinding shows an overall increase compared to that of the samples before grinding.

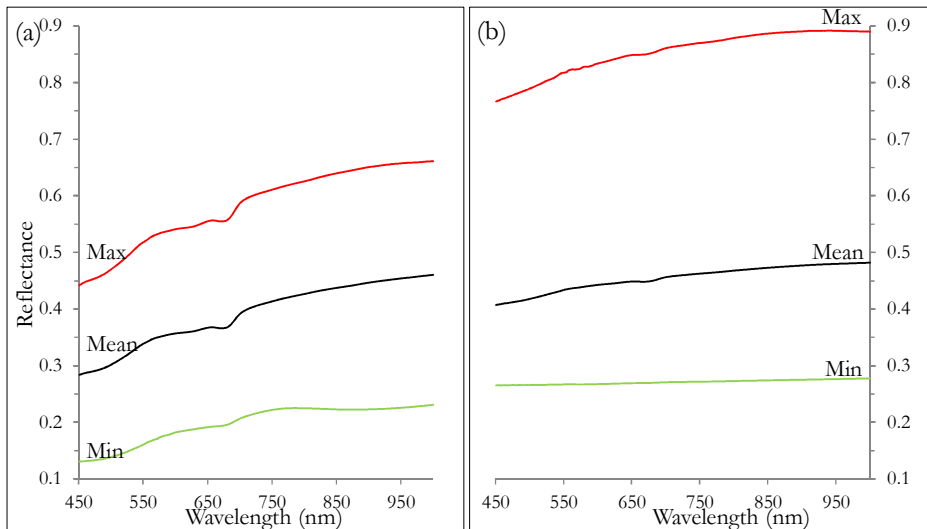


Figure 15 A comparison of the mean spectra of the samples from location 2 and 3. a) before pulverization (original grain size) and b) after pulverization and sieved to $<0.25\text{mm}$. The absorption feature centred at 674nm appears clearer and deeper in the sample spectra before pulverization. After pulverization, the absorption feature becomes less deep and overall albedo increased.

Figure 16 shows an example of hyperspectral imaging result. An ROI was drawn inside grain samples, and the mean spectra were calculated. All grain samples had an absorption feature at 674nm. The mean spectral reflectance of the ROI was filtered due to noise. Figure 16b compares the spectral reflectance before and after filtering.

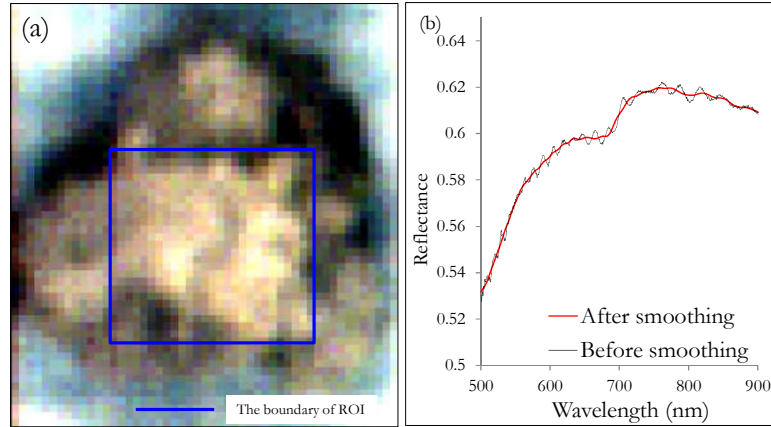
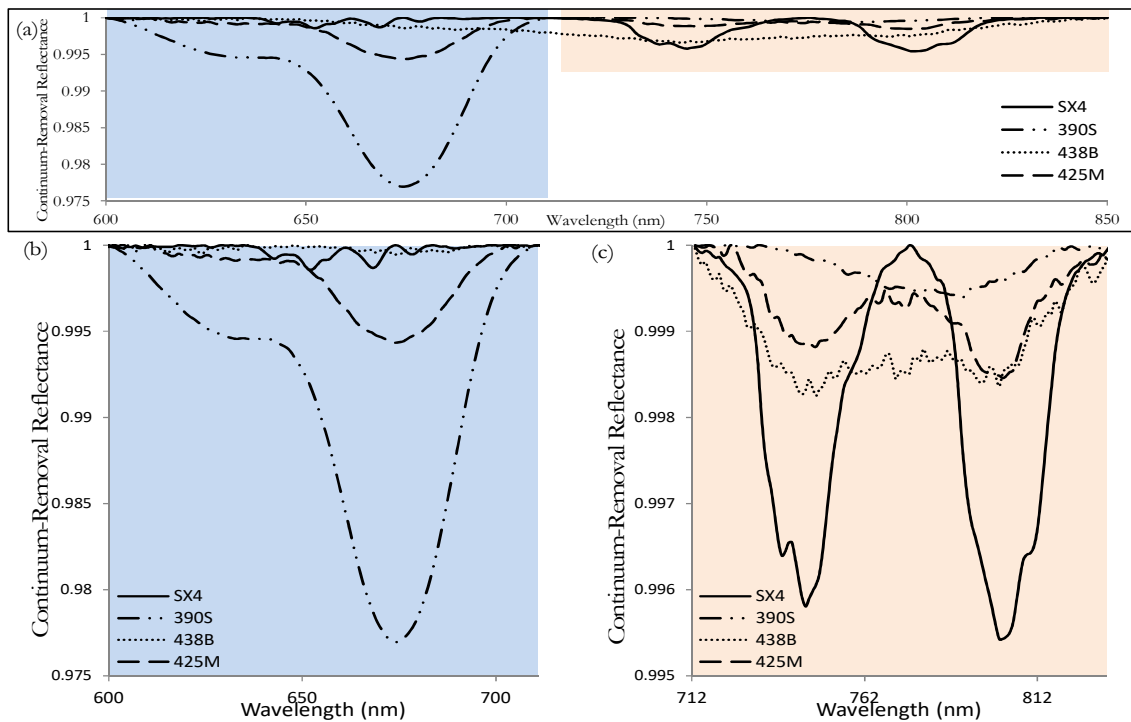


Figure 16 An illustration of ROI and its mean spectra. a) A region of interest (a blue rectangle) was drawn on a hyper-spectral image with ID sample of 1A3. The spatial resolution of the image is $110\mu\text{m}$ pixel resolution. b) The mean spectra of the ROI before smoothing (a black line) and after smoothing (a red line).

Figure 17 shows spectral variation in the depth and shape of absorption features. The position of the 674nm absorption feature in the spectra of obtained samples is next to the absorption feature related to Er in the spectra of Xenotime.



Sample ID	Nd concentration	Sm Concentration	Dy Concentration	Er Concentration
SX4	453 ppm	131 ppm	370 ppm	562 ppm
390S	62 ppm	14 ppm	17 ppm	2722 ppm
438B	505 ppm	86 ppm	19 ppm	178 ppm
425M	3903 ppm	686 ppm	118 ppm	352 ppm

Figure 17 a) Spectral variation varying in REE concentrations in the wavelength range between 600nm and 850nm after applying continuum removal. b) As 674nm absorption feature goes deeper, the absorption feature becomes double. c) A high concentration of Nd and Sm in sample 425M results in a distinct absorption feature centred at $\sim 745\text{nm}$ and $\sim 802\text{nm}$ related to Nd, Sm, and Dy. Apparently, these two absorption features merge and/or overlap into one absorption feature centred at $\sim 771\text{nm}$ as Nd, Sm, and Dy concentration decreases.

4.3. Statistical correlation between REE concentration and spectral reflectance

A linear statistical relationship among Sc, Y, La, Ce, Nd, Er, and Fe was defined using Pearson correlation coefficient. No statistics were computed for Sm, Eu, Dy, Ho, Yb, and Lu, as most of their concentration in samples was below LOD. Figure 18 shows Pearson correlation among REE and Fe concentration on a log scale. The correlation among Sc, La, Ce, and Nd was stronger compared to when they are in pairs with Y or Er. Meanwhile, Y and Er showed a stronger correlation compared to when they are in pairs with Sc, La, Ce, or Nd.

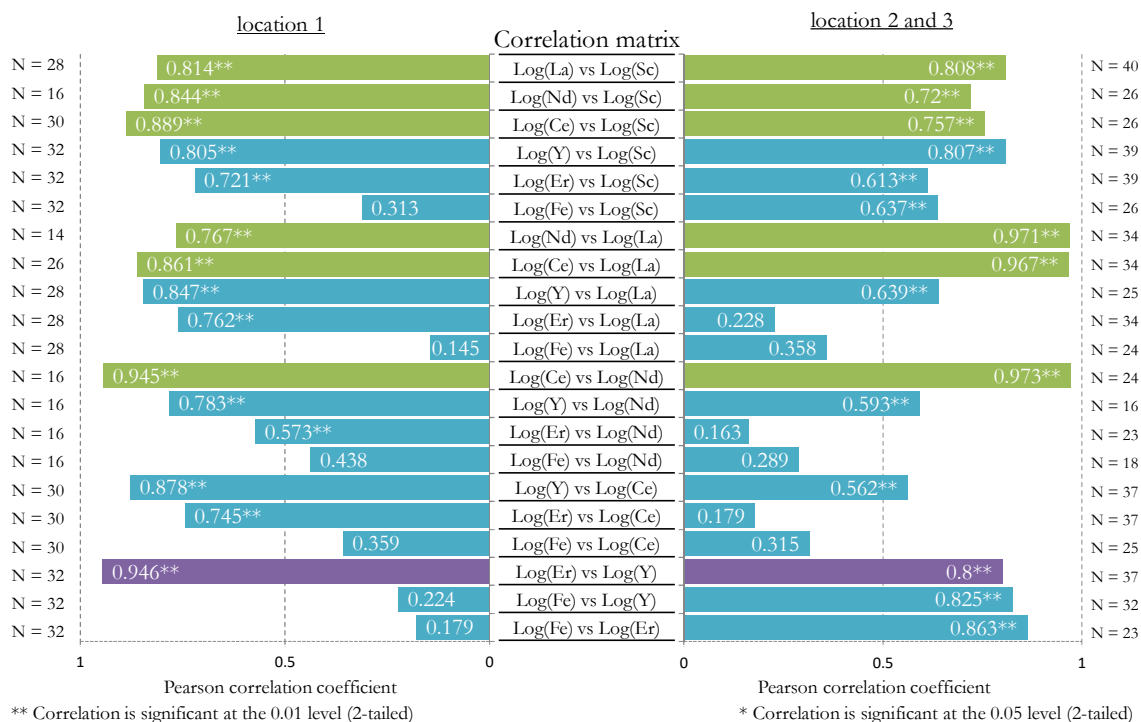


Figure 18 Pearson correlation coefficient among REE and Fe concentrations. La, Ce, Nd, and Sm had the highest correlation coefficient when they are in pairs among La, Ce, Nd, and Sm. Similarly, Y and Er had the strongest correlation coefficient when they are in pairs. Green charts indicate a correlation between a pair of LREE, purple charts between a pair of HREEs, and blue charts between a pair of LREEs, HREEs or Fe.

All samples were duplicated when their REE concentrations were measured in ICP-OES, and Table 6 summarizes the different concentrations in between a pair of duplicated samples. As can be seen from Table 6, the estimation of precision for Sc, Y, La, Ce, Nd, and Er concentrations in the samples of location 1 is higher than in the samples of location 2 and 3. A high value indicated that samples are not homogeneous.

Table 6 The Estimation of Precision (EOP) between duplicated samples as an indication of sample homogeneity. Bold-style numbers indicated the EOP values more than 30%, meaning they are not homogeneous.

EOP	Sc	Y	La	Ce	Nd	Er
Total concentration samples of location 1	37%	54%	44%	60%	68%	68%
Total concentration of location 2 and 3	18%	24%	27%	27%	28%	18%

EOP is given by $[\text{Absolute}(a - b) / ((a + b) / 2)] \times 100$, where a and b are the concentration of a pair of duplicated samples. In general, the calculated values for the samples of location 1 are double than the EOP value for the samples of location 2 and 3. Dindal et al. (1999) recommend the EOP value is less than 30%.

To explore which of absorption features correlate with REE concentration, the obtained spectra were continuum-removed, and the depth absorption feature of each band was related to REE concentrations. Figure 19 shows the Pearson correlation coefficient value between the depths of absorption features and REE concentrations in total concentration samples of location 1, 2, and 3.

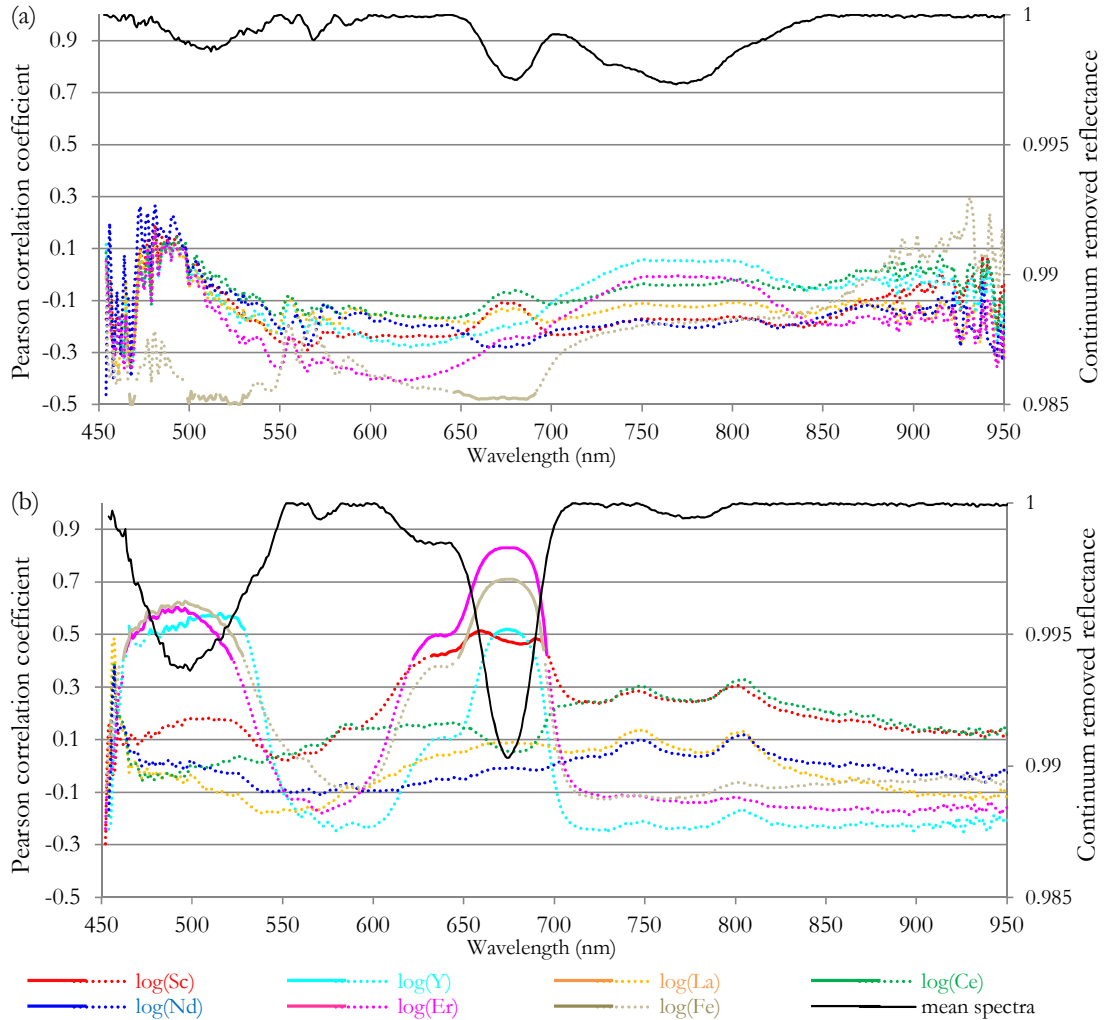


Figure 19 Pearson correlation value between the depth of continuum-removed spectra and REE concentrations. a) Band depth of continuum-removed spectra and REE concentrations in total concentration samples of location 1 do not have correlation. b) Regarding location 2 and 3, Y, Er, and Fe show a correlation with several band depth around absorption features centred at 500nm and 674nm and their r-value is more than 0.4, and the p-value is less than 0.01. In the graph, solid lines indicate a correlation with a p-value less than 0.01, and dash lines indicate a correlation with a p-value more than 0.01.

A linear statistical relationship between spectral parameters and REE concentrations was defined using Pearson correlation coefficient as plotted in Figure 20 and Figure 21. In location 1, the correlation value between spectral parameters and REE concentrations was lower than 0.5, and the strongest correlation was between $\text{Ratio}_{550/500}$ and Er concentration with an r-value of only 0.462 and a p-value less than 0.01 (Figure 20).

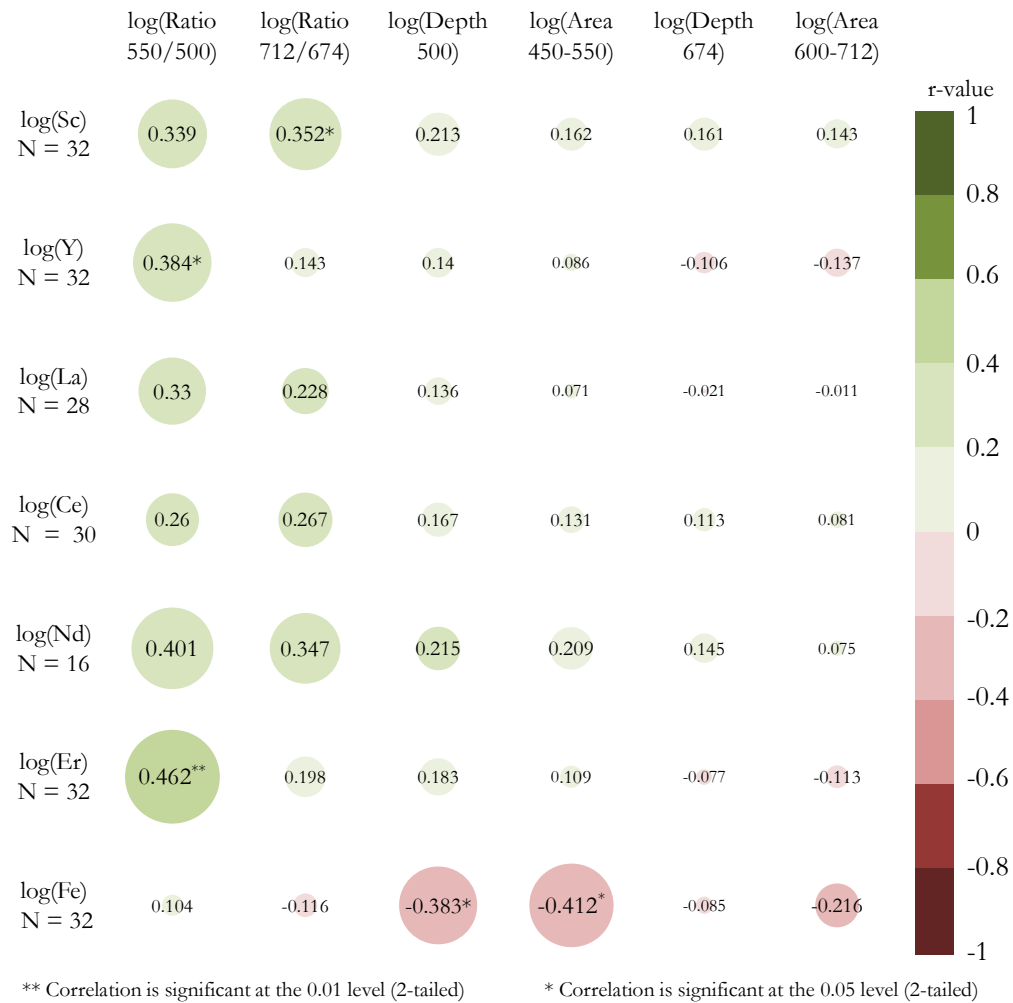


Figure 20 Location 1: Pearson correlation coefficients between spectral parameters and REE concentrations (on a logarithmic scale). The highest r-value is 0.462 calculated from log(Er) and log (Ratio_{550/500}).

In location 2 and 3, all parameters had no significant correlation with Sc, La, Ce, and Nd concentrations; only Ce and band area₇₁₂₋₈₃₂ show a weak correlation (0.320) with a p-value less than 0.05 (Figure 21). In contrast, Er concentration showed the strongest relationship (0.829) with band ratio_{712/674} and a significant correlation with ratio_{550/500}, depth₅₀₀, area₄₅₀₋₅₅₀, depth₆₇₄, and area₆₀₀₋₇₁₂. Fe was suspected to be the cause of absorption features centred at ~500nm and had a strong correlation with band ratio_{550/500}, band depth₅₀₀, and band area_{550/500} (0.683, 0.552, and 0.593 respectively); however, its correlations were weaker than Er with band ratio_{550/500}, band depth₅₀₀, and band area_{550/500} (0.685, 0.604, and 0.640 respectively). Regarding Y, it was expected not to have an absorption features in the VNIR wavelength range (Turner et al., 2014), yet had a significant correlation with band ratio_{550/500}, band ratio_{712/674}, band depth₅₀₀, and band area₄₅₀₋₅₅₀.

A linear correlation between the infrared absorbance spectra and REE concentration was also defined using Pearson correlation coefficient. Three spectral parameters (band area₈₇₃₋₁₂₁₇, band area₇₀₉₋₈₁₁, and band area₆₇₇₋₇₀₉) were correlated to REE concentration, and the results are summarized in Table 7. All spectral parameters had a strong correlation (>0.6) with La, Ce, and Nd concentration, and a weak correlation (<0.4) with Sc concentration. Meanwhile, Y, Er, and Fe concentration did not correlate with the three spectral parameters.

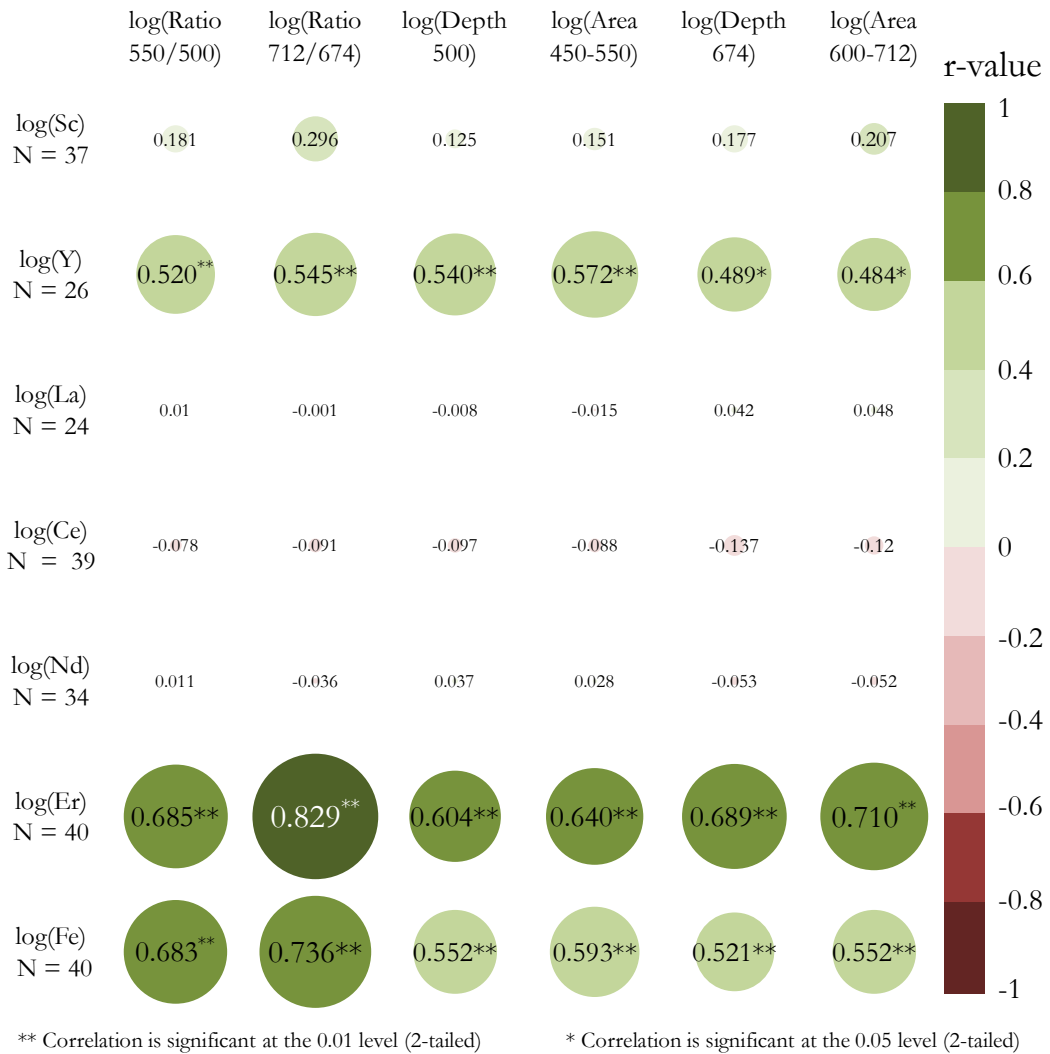


Figure 21 Location 2 and 3: Pearson correlation coefficients between spectral parameters and REE concentrations (on a logarithmic scale). Of REEs and Fe, Er had the highest correlation, followed by Fe and Y. LREE (Sc, La, Ce, and Nd) do not have a significant correlation with all spectral parameters.

Table 7 Pearson correlation coefficients between three spectral parameters of FTIR-ATR infrared absorbance and REE concentrations. Bold-style numbers indicate an r-value higher than 0.5.

The samples of location 1 (ΣN = 32)							
Area	Sc (N = 32)	Y (N = 32)	La (N = 28)	Ce (N = 30)	Nd (N = 16)	Er (N = 32)	Fe (N = 32)
873-1217	0.080	-0.081	-0.053	0.053	-0.211	-0.154	0.311
709-811	0.084	-0.065	-0.038	0.053	-0.158	-0.138	0.256
677-709	0.062	-0.078	-0.056	0.035	-0.148	-0.179	0.355*
The samples of location 2 and 3 (ΣN = 40)							
Area	Sc (N = 37)	Y (N = 26)	La (N = 24)	Ce (N = 39)	Nd (N = 34)	Er (N = 40)	Fe (N = 40)
873-1217	0.398*	0.308	0.798**	0.753**	0.750**	-0.286	-0.159
709-811	0.376*	0.255	0.719**	0.670**	0.666**	-0.274	-0.155
677-709	0.376*	0.225	0.692**	0.644**	0.641**	-0.287	-0.175

In location 1, the highest correlation coefficient is only 0.355 for a correlation between Fe and Area 677-709. In location 2 and 3, La, Ce, and Nd concentrations had a strong correlation with a p-value less than 0.01, while Sc had a weak correlation with the three spectral parameters.

4.4. Quantitative relationships

The quantitative relationship between Er and spectral parameter values is listed in Table 8 and Table 9. The values of R² and RPD were used to evaluate the performance of multilinear regressions. As shown in Table 8, the two multilinear regressions for predicting Er concentration in the samples of location 1 had R² < 0.6 and RPD < 1. In comparison, the two multilinear regressions for predicting Er concentration in the samples of location 2 and 3 had higher R² and RPD. Both regressions had R² > 0.6 and RPD > 1.

Table 8 Statistical summary of stepwise and enter multilinear regressions for location 1. The two regressions have an RPD-value less than 1.

Regression	Predictor	F	p-value	R ²	RPD
Stepwise multilinear regression					
log(Er)	log (Ratio _{550/500}), log(Area ₇₁₂₋₉₃₂)	12.777	0.008	0.432	0.752
Enter multilinear regression					
log (Er)	log (Area ₇₁₂₋₈₃₂), log (Area ₆₀₀₋₇₁₂), log (Depth ₇₇₂), log (Area ₄₅₀₋₅₅₀), log (Ratio _{550/550}), log (Ratio _{712/674}), log (Depth ₆₇₄), log (Depth ₅₀₀)	3.42	0.010	0.543	0.734

Table 9 Statistical summary of stepwise and enter multilinear regressions for location 2 and 3. The two regressions have an R²-value more than 0.6 and an RPD-value more than 1.

Regression	Predictor	F	p-value	R ²	RPD
Stepwise multilinear regression					
log(Er)	log (Ratio _{712/674})	83.278	0.000	0.687	1.763
Enter multilinear regression					
log (Er)	log (Area ₇₁₂₋₈₃₂), log (Area ₆₀₀₋₇₁₂), log (Depth ₇₇₂), log (Area ₄₅₀₋₅₅₀), log (Ratio _{550/550}), log (Ratio _{712/674}), log (Depth ₆₇₄), log (Depth ₅₀₀)	15.558	0.000	0.801	1.996

4.5. REE detectability by satellite remote sensing sensors

To determine whether the 675nm absorption feature could be detected spectrally by satellite remote sensing, laboratory spectra were resampled to Landsat 8 OLI, Worldview2, and Sentinel-2 MSI spectral resolution. The three satellites were chosen because they have three bands in the vicinity of the 674nm absorption feature. Figure 22 compares the result of resampling sample spectra (Figure 22a) and Xenotime spectra (Figure 22b).

As can be seen in Figure 22a, the 674nm absorption feature related to Er is retained in Sentinel-2 MSI, WorldView2, and Landsat 8 OLI resampled spectra. Despite having a lower spectral resolution compared to Sentinel-2 MSI and WorldView2, Landsat 8 OLI showed an indication to be able to detect the 674 absorption feature at band 4. Absorption features of Xenotime are not present in Landsat 8 OLI resampled spectra (Figure 22b). Likewise, Neave et al. (2016) demonstrated a similar result when resampling Monazite spectra to Landsat 8 OLI spectral resolution. The absorption feature related to Nd, Sm, and Dy at ~745nm in Xenotime spectra was retained in Sentinel-2 resampled spectra, but not in WorldView2 resampled spectra.

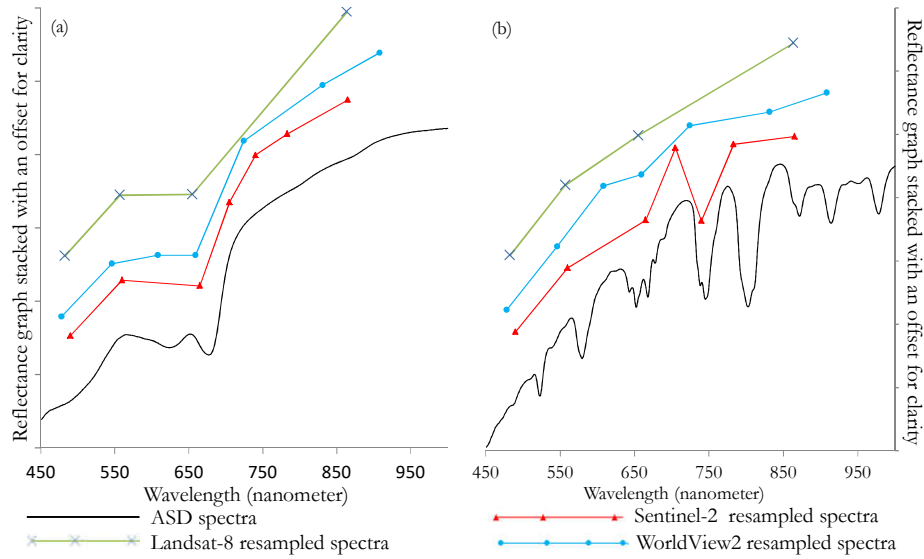


Figure 22 Plots showing the result of resampling spectra to the spectral response functions of Landsat 8 OLI, Sentinel-2 MSI and WorldView2. a) The REE-related absorption feature in sample spectra at $\sim 674\text{nm}$ is still retained in Landsat 8 OLI, Sentinel-2 MSI and WorldView2 resampled spectra. b) Regarding resampling Xenotime spectra to Sentinel-2 MSI, WorldView2, and Landsat 8, most spectral information is lost in Landsat 8 OLI resampled spectra, whereas Sentinel-2 MSI resampled spectra retain two absorption features at $\sim 651\text{nm}$ related to Er and $\sim 745\text{nm}$ related to Nd, Sm, and Dy. Dots in resample spectra indicated each band of corresponding sensors.

Regarding spatial resolution, Landsat 8 OLI and Sentinel-2 MSI images were evaluated by displaying the study area. The feasibility of WorldView2 spatial resolution was not evaluated due to lack of cloud-free data. Nevertheless, the spatial resolution of WorldView2 is higher than that of Sentinel-2 MSI. As shown in Figure 23a-c, the 10m spatial resolution of Sentinel-2 MSI image was sufficient to discriminate between tailing and vegetation area. Meanwhile, the boundary between tailing and vegetation area was not distinct in Landsat 8 OLI image with 30m spatial resolution (Figure 23d-f).

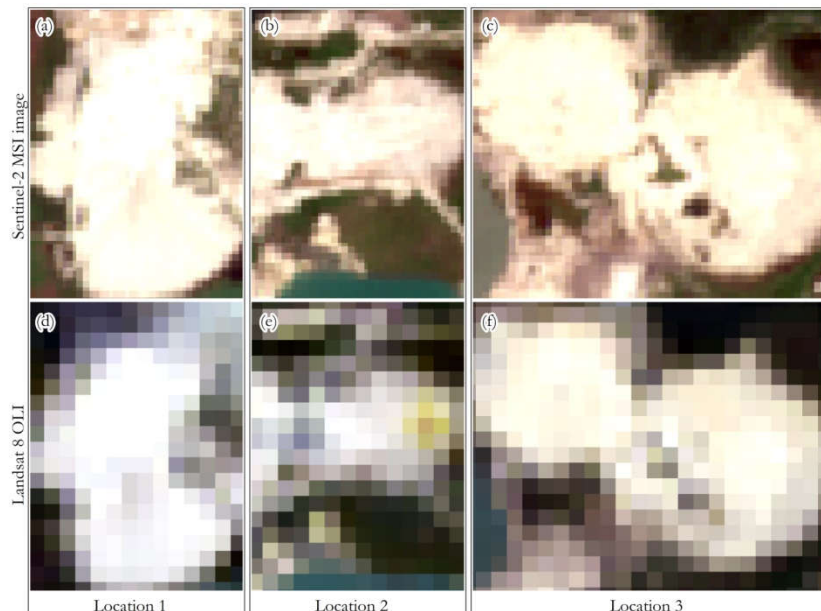


Figure 23 A comparison of Sentinel-2 MSI and Landsat 8 OLI spatial resolution. Location 1(a, d), location 2 (b, e), and location 3 (c, f) shown in natural colour of Sentinel-2 MSI (a, b, c) and Landsat 8 OLI (d, e, f) images. The spatial resolution of shown images is 10m for band 2, 3, and 4 of Sentinel-2 MSI and 30m for Landsat 8 OLI.

Three spectral parameters (band ratio, band depth, and band math) were used to target the 674 absorption features, and statistical correlation between the spectral parameters and REE concentrations are shown in Table 10 and Table 11.

In the samples of location 1, most of the three spectral parameters in all resampled spectra showed a weak (r -value <0.5) to non-existent correlation with Sc, Y, La, Ce, Nd, Er, and Fe concentration in the samples of location 1, as shown in Table 10. Only band ratio of Landsat 8 OLI resampled spectra, and Nd showed a significant correlation with an r -value of 0.519 and p -value less than 0.05.

In the samples of location 2 and 3, only Er and Fe concentrations showed a weak to strong correlation with three spectral parameters calculated from Sentinel-2 MSI resampled spectra and WorldView2 resampled spectra, with r -value varied from 0.486 to 0.738 and a p -value less than 0.01. Of three spectral parameters calculated from Landsat 8 OLI resampled spectra, only band ratio had a significant correlation with Er and Fe concentration with an r -value of 0.723 and 0.692 respectively, and a p -value less than 0.01 for both concentrations.

Table 10 Pearson correlation coefficients between spectral parameters and REE concentrations in the samples of location 1. Only Nd concentration and Band ratio (B5/B4) of Landsat 8 OLI resampled spectra have an r -value more than 0.5 indicated by bold-style numbers. In table, B stands for band.

Elements	Sentinel-2 MSI resampled spectra			WorldView2 resampled spectra			Landsat 8 OLI resampled Spectra		
	B5/B4	Depth B4	(B3 - B4) x (B5 - B4)	B6 /B5	Depth B5	(B4 - B5) x (B6 - B5)	B5/B4	Depth B4	(B3 - B4) x (B5 - B4)
Sc (N=32)	0.421*	-0.219	0.026	0.417*	-0.184	-0.013	0.428*	-0.232	-0.159
Y (N=32)	0.330	-0.222	-0.090	0.316	-0.225	-0.129	0.365*	-0.267	-0.243
La (N=28)	0.326	-0.182	-0.013	0.322	-0.144	-0.031	0.320	-0.197	-0.123
Ce (N=30)	0.359	-0.177	-0.052	0.361*	-0.158	-0.081	0.347	-0.213	-0.178
Nd (N=16)	0.459	-0.302	-0.062	0.418	-0.365	-0.186	0.519*	-0.295	-0.279
Er (N=32)	0.355*	-0.277	-0.102	0.340	-0.279	-0.138	0.441*	-0.326	-0.301
Fe (N=32)	-0.118	-0.348	-0.152	-0.123	-0.360*	-0.213	-0.159	-0.367*	-0.378*

** Correlation is significant at the 0.01 level (2-tailed)

* Correlation is significant at the 0.05 level (2-tailed)

Table 11 Pearson correlation coefficients between spectral parameters and REE concentrations in the samples of location 2 and 3. In the table, B stands for band. Bold-style numbers indicate an r -value more than 0.5.

Elements	Sentinel-2 MSI resampled spectra			WorldView2 resampled spectra			Landsat 8 OLI resampled Spectra		
	B5/B4	Depth B4	(B3 - B4) x (B5 - B4)	B6 /B5	Depth B5	(B4 - B5) x (B6 - B5)	B5/B4	Depth B4	(B3 - B4) x (B5 - B4)
Sc (N=37)	0.071	0.157	0.130	0.051	0.160	0.138	0.065	0.052	0.047
Y (N=26)	0.321	0.197	0.220	0.306	0.166	0.276	0.288	-0.211	-0.059
La (N=24)	-0.197	-0.189	-0.151	-0.217	-0.207	-0.152	-0.237	-0.182	-0.117
Ce (N=39)	-0.119	-0.114	-0.098	-0.134	-0.125	-0.104	-0.154	-0.126	-0.080
Nd (N=34)	-0.130	-0.139	-0.115	-0.145	-0.156	-0.122	-0.163	-0.154	-0.093
Er (N=40)	0.738**	0.644**	0.567**	0.728**	0.641**	0.630**	0.723**	0.193	0.187
Fe (N=40)	0.713**	0.567**	0.486**	0.704**	0.577**	0.571**	0.692**	0.125	0.173

** Correlation is significant at the 0.01 level (2-tailed)

* Correlation is significant at the 0.05 level (2-tailed)

Er and Fe concentrations show a consistent correlation with three spectral parameters of Sentinel-2 MSI and WorldView2 resampled spectra.

4.6. Application to multispectral images

Sentinel-2 MSI and Landsat 8 OLI images were first masked for vegetation and water. Vegetation and pond in tailing area were used as a calibration to determine thresholds for masking. The NDVI threshold for Sentinel-2 MSI was 0-0.09697. The value of 0.09697 was the NDVI value of a pixel inside a cyan box in Figure 24a. Meanwhile, the NDVI threshold for Landsat 8 OLI images was 0-0.1883. Pixels with NDVI values outside the NDVI threshold value were masked and remove from the images because they were vegetation.

In the location 3, water and vegetation are mixed in some area, and this area was masked by using Sentinel-2 MSI band 8a and Landsat 8 OLI band 5. Pixels with reflectance value less than 0.4 were remove from the images. The value of 0.4 was chosen to mask water area in location 3 indicated by a cyan box in Figure 24b. The Images of NDVI products and masked water can be found in Appendix F. Figure 25 displays the final images after masking vegetation and water.

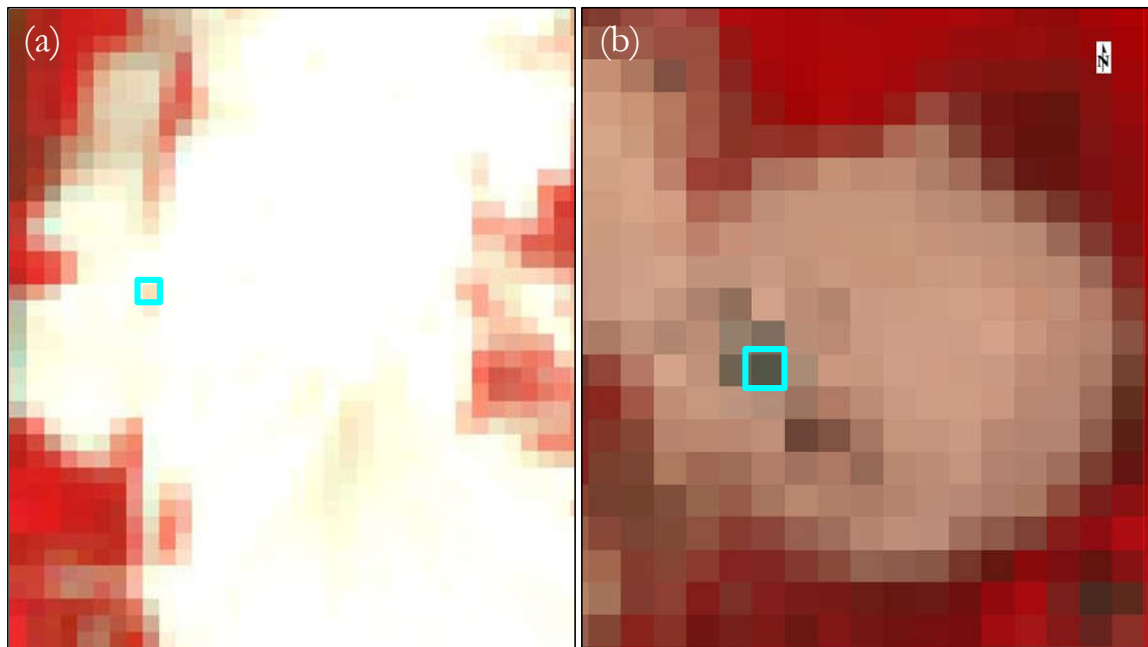


Figure 24 a) A false colour composite of Sentinel-2 MSI band 6, 4, 3 (R-G-B) in a 2-98% linear stretch. A cyan box indicates a pixel of trees in tailing area. The NDVI value of the pixel is 0.09697. b) A false colour composite of Landsat 8 OLI band 5, 4, 3 (R-G-B) in a 2-98% linear stretch. Reddish colour indicates the presence of vegetation. A cyan box indicates a pixel of water in tailing area. The NDVI value for the pixel is 0.1883. The spatial resolutions of the shown images are 10m for Sentinel-2 MSI and 30m for Landsat 8 OLI.

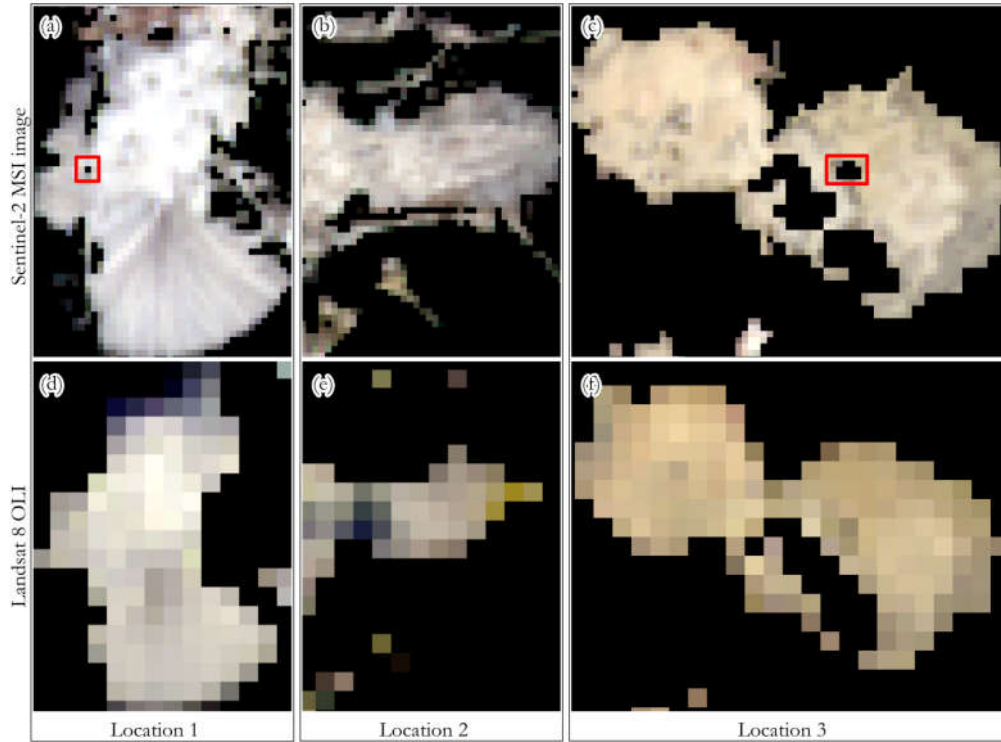


Figure 25 Image products after removing vegetation and water areas. Location 1(a, d), location 2 (b, e), and location (c, f) shown in natural colour of Sentinel-2 MSI (a, b, c) and Landsat 8 OLI (d, e, f) image in a 2-98% linear stretch. The spatial resolution of Landsat 8 OLI and Sentinel-2 MSI is 30m and 10m respectively. Red-coloured boxes indicate areas that are masked in Sentinel-2 MSI image, but not in Landsat 8 OLI image.

Images of spectral parameters (band ratio, depth, and math) products derived from Sentinel-2 MSI and Landsat 8 OLI images are in Appendix G. Colour composite images of spectral parameter products are shown in Figure 26. A white-coloured pixel in composite images (Figure 26) indicated that there is an absorption feature at Band 4 of the Sentinel-2 MSI and Landsat 8 MSI image. However, all pixels of Landsat 8 MSI image appeared white.

A linear stretch was applied to the colour compose of spectral parameter images. The threshold values of 0-0.02 for band depth was based on a hypothetical case where an absorption feature at band 4 should have a depth of more than 0.02. If the absorption feature formed a symmetrical absorption feature with a band depth of 0.02, then the value for band math should be 0.0004 given by $((B3-B4) \times (B5-B4))$, where B3 and B5 are equal to 1, and B4 is equal to 0.98. A spectral reflectance with an absorption feature centred at band 4 will have a higher reflectance value in band 5 compared to band 4. Thus, the value of band ratio should be more than 1. The high value (1.05) of band ratio was chosen based on trial and error when displaying the three spectral parameter products as a RGB colour image.

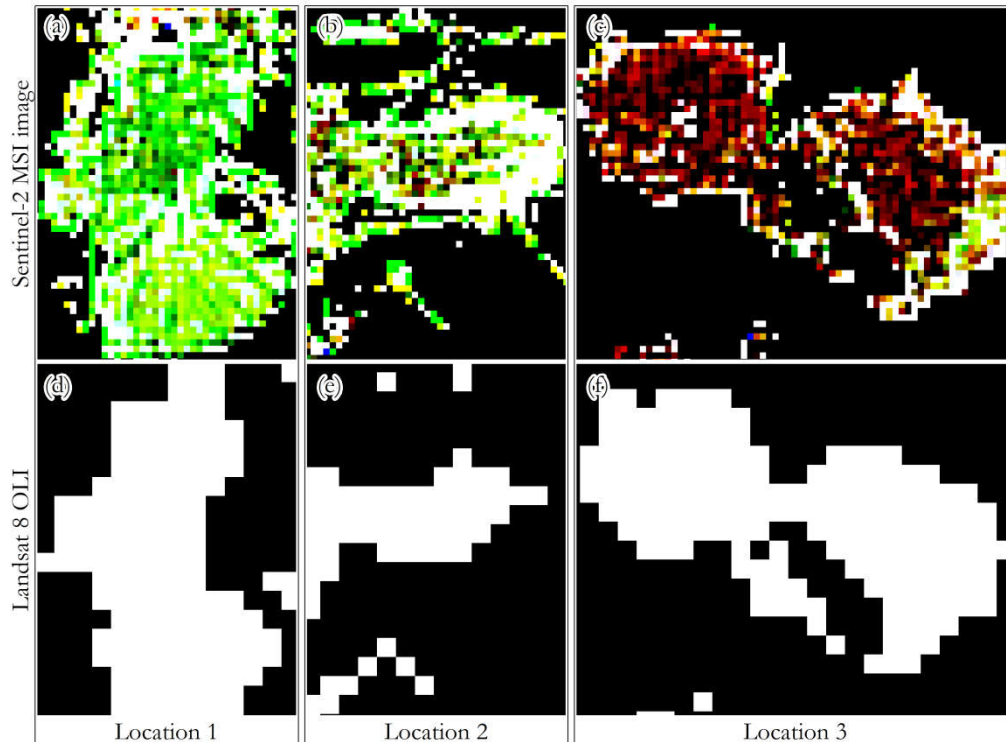


Figure 26 Colour composite images of band ratio, depth, and math derived from Sentinel-2 MSI (a-c) and Landsat 8 OLI (d-f) images showing location 1 (a, d), location 2 (b, e) and location 3 (c, f). A linear stretch was applied to the images, and the thresholds value for band ratio was (1.0001) ■ *high* (1.05) , for band depth was *low* (0) ■ *high* (0.02) , for band math was *low* (0) ■ *high* (0.0004) . A white-coloured pixel indicates a combination of high value for the three bands, meaning that there is an absorption feature at Band 4 of the Sentinel-2 MSI and Landsat 8 MSI image

The spectral reflectance of the colour composite of spectral parameter products was checked. Figure 27 compares the spectral reflectance of Sentinel-2 MSI and Landsat 8 OLI images. Three absorption features at band 4 (665nm), band 5 (704nm), and band 6 (740nm) were observed in the Sentinel-2 MSI image. Meanwhile, only one absorption feature at band 4 (654nm) was observed in the Landsat 8 OLI image.

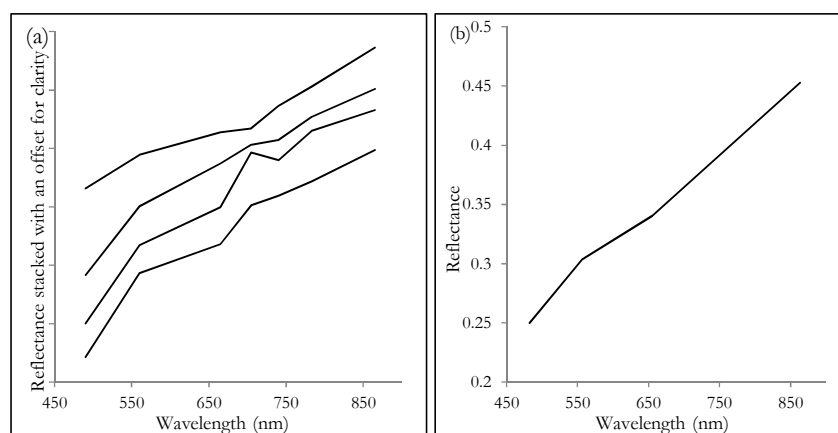


Figure 27 Comparing spectral variations in absorption features detected in the Sentinel-2 MSI image compared to the Landsat 8 OLI image. a) In the Sentinel-2 MSI image, three absorption features are detected at band 4 (665nm), band 5 (704nm), and band 6 (740nm). b) In the Landsat 8 OLI image, only one absorption feature is observed at band 4. White pixels in Figure 26 indicate the presence of the absorption feature at band 4 of both Sentinel-2 MSI and Landsat 8 OLI images, and yet, white pixels in the Sentinel-2 MSI image can possess two absorption features at band 4 and band 6.

5. DISCUSSION

5.1. Chemical compositions

All REEs were detected in samples (Table 2 and Table 3) except for Promethium because it does not occur in nature (MacMillan et al., 2017; Massari et al., 2013). Thulium and Praseodymium were also not reported because their candidate wavelengths in ICP-OES experienced signal intensity (Table 1).

REE concentrations of the leached samples were slightly higher than that of the water samples (Table 2). This might be due to grinding and stirring processes. As stated by Myers (2013) and Upadhyay (2006), stirring and increasing the surface area of samples increase the rate of the chemical process. From Figure 10, the mean REE concentrations were 200 times or higher than in leached samples. These results are in agreement with Zawisza et al. (2011) findings that showed a low solubility of REEs. These results can be interpreted as such that rainwater will barely wash away REEs in tailings.

Regarding environmental aspects, the concentration of REEs in leached samples and water samples were slightly higher than that of natural water that ranges from ng/g to µg/g (Zawisza et al., 2011). However, no thresholds for REEs to the environment have been defined by the European Union, World Health Organization, or United States Environmental Protection Agency. This is because most attention has been paid to heavy metal toxicology (Rim et al., 2013) and only few REE toxicology data are available (Hatje et al., 2016; MacMillan et al., 2017; Tepe et al., 2014). However, REEs have been recognized as new, emerging contaminants, and possible negative effects on the human body (Hatje et al., 2016; MacMillan et al., 2017; Rim et al., 2013; Tepe et al., 2014).

The mean Er concentration in the samples showed an indication of enrichment that surpasses the mean Er concentration in the processed REE ore of Mount Pass deposit (Figure 11). However, it remained unclear as to the reason of the enrichment. There is no study that discussed Er anomaly whether in the study area or elsewhere. From Table 4, we can see that the concentration of major elements was low. Tailing samples were identified as Quartz, and Fe, Mg, Ca, and Al were present as impurities in Quartz lattices (Flem et al., 2002).

5.2. Spectral reflectance

When dealing with Monazite or Xenotime spectra, it was expected to encounter absorption features centred at 583, 744, 802 and 871nm that are related to Nd, Dy, and Sm and absorption features centred at ~651nm are related to Er (Neave et al., 2016; Turner et al., 2016). These features are noticeable at the spectra of the mixture; however, these features are noticeable in the sample spectra (Figure 14). This might be because of low Nd, Sm, and Dy concentration in the samples.

ICP-OES, XRD and FTIR-ATR analysis confirmed that the samples mainly consisted of Quartz. As Quartz, they should have weak to non-existent absorption in the VNIR wavelength range (Adams, 1965; Hunt, 1977), and yet, we observed a distinct, narrow absorption feature centred at ~674nm in the sample spectra. A comparison with United States Geological Survey (USGS) mineral spectral library (Clark et al., 2007) and published spectra of REE-oxide and REE-bearing minerals was made, but to date, no spectra matched the 674nm absorption feature of the sample spectra.

The absorption features centred at ~500nm might be due to the presence iron oxide. As shown in Figure 14, the 500nm absorption feature in the mean spectra of samples from location 2 and 3 was more clear than that of samples from location 1 since the mean Fe concentration in the samples of 2 and 3 was higher than in the samples of location 1. A possible explanation for the 674nm absorption feature might be due to the presence of Er, considering Er concentration in samples and the band position of Er around 651nm in Xenotime spectra (Figure 17a and b). Regarding the absorption features around 700nm (Figure 17c), it might be due to either too low REE concentrations and/or the overlap of REE absorption features, and this result was in line with a hypothesis stated by Turner et al. (2014).

5.3. The effect of samples preparation

In this study, we observed that sample preparation influenced the results of the chemical composition measurements and the spectral reflectance. Also, it played a significant role in achieving a homogeneous sample that is the key in relating geochemical values and the spectral parameters.

In the samples of location 2 and 3, candidate samples were selected when they have three absorption features centred at 745nm, 801nm, and 873nm. These absorption features are due to Nd, Sm, and Dy. Because of this, the mean concentration of Nd (150 $\mu\text{g/g}$), Sm (119 $\mu\text{g/g}$), and Dy (23.3 $\mu\text{g/g}$) in the samples of location 2 and 3 is higher than that of Nd (20.1 $\mu\text{g/g}$), Sm (6.98 $\mu\text{g/g}$), and Dy (11.6 $\mu\text{g/g}$) in the samples of location 1 (Table 3).

To quantify REE concentration, samples were duplicated, and the precision of duplicate samples was estimated. From Table 6, the samples from location 2 and 3 were indicated that they were homogeneous. However, the samples from location 1 were heterogeneous. To cope with heterogeneous samples, Dasher (2014) removed them from the computation. However, in this research they were incorporated into the computation. As a result of heterogeneous samples, geochemical values and spectral reflectance of samples from location 1 had low-to-no correlation.

The heterogeneity of samples from location 1 can be explained by the fact that they were prepared by grinding all samples without sorting the grain size, and this grains are varied in size and REE concentrations. A study to establish a statistical correlation between Nd-related absorption features and Nd concentration conducted by Neave et al. (2016) indicated that grain size could cause a low correlation value. Also, Navarro et al. (2002) reported that the pulverized mineral grains such as zircon and apatite which are REE-bearing minerals are difficult to homogenize completely. Furthermore, only 0.1g of each sample was analysed in ICP-OES, and this amount might not be representative for the entire sample.

Sample pulverization was expected to enhance the spectral contrast of the spectral reflectance data. However, it gave a counter-intuitive effect in which the depth of absorption feature becomes less. We also observed that the overall albedo of sample spectra increases as the grain size of the samples decrease. In this case, a study conducted by Hapke (1993) might be the explanation. In his study, the strength of absorption features increases with decreasing grain size; however, further decreases in grain size will lead the strength of absorptions to weaken as volume scattering plays a diminishing role relative to first surface interactions.

Adams & Filice (1967) studied the spectral reflectance of silicate rock powders, and some result was noted. In large grain size, the overall albedo of sample spectra is low because the incident light was strongly absorbed, only specular and diffuse components from the surface of the particle were recorded. The diminution of particle size cause some light to penetrate some particle and bounce back to the sensor, and hence, cause an increase in reflection.

5.4. Statistical correlation between REE concentration and spectral reflectance

From Figure 18, Sc, La, Ce, and Nd show a tendency to have a high correlation when they are in pairs among themselves. Meanwhile, Y and Er showed a strongest correlation compared to when they are in pairs. This tendency is related to the fact that Sc, La, Ce, and Nd are in the same group of LREE, while Y and Er are in HREE.

From Figure 19, Y, Er, and Fe showed a significant correlation with the absorption features centred at ~500nm and ~674nm so that these two absorption features were explored further in deriving spectral parameters. The weak correlation between spectral parameters and REE concentrations of the samples of location 1 may be explained by the fact that they are not homogeneous (Table 6).

Er concentration in the samples of location 2 and 3 showed the strongest relationship (0.829) with band ratio_{712/674} (Figure 21). This relationship is further supported by the presence of Er, being the origin of the 674nm absorption feature. Y and Fe concentration also showed a correlation with band ratio_{712/674} with the Pearson correlation coefficient of 0.545 and 0.736 respectively. According to Turner et al. (2014), Y does not have absorption features in the VNIR wavelength range. However, in this study, Y had a correlation with band ratio_{550/500}, band ratio_{712/674}, band depth₅₀₀, and band area₄₅₀₋₅₅₀. The reason for the significant correlation of Y and Fe with band ratio_{712/674} might have something to do with the strong correlation between Y and Er with an r-value of 0.8, and Fe and Er with an r-value of 0.863 (Figure 18). Also, Y was associated with Er being an HREE.

5.5. Quantitative relationship

Stepwise and enter multiple linear regressions were used for modelling a quantitative relationship between Er and spectral parameters. Sample heterogeneity also became an issue in the samples of location 1, when we established a quantitative relationship between Er and spectral parameters (Table 8). The RPD value of both multiple linear regressions was less than 1, meaning that spectral parameters are not capable of predicting Er concentration (Williams et al., 1993).

Regarding predicting Er concentration in the samples of location 2 and 3, stepwise multiple linear regression had an R² of 0.687 and RPD of 1.763. Meanwhile, enter multiple linear regression showed an R² of 0.801 and RPD of 1.996. According to Wang et al. (2017) who also tried to predict REE concentrations using spectroscopy data, these R² and RPD values of stepwise multiple linear regression indicate a reasonable prediction, while these R² and RPD values of multiple linear regression indicate a good prediction.

5.6. Probable origin of the 674 absorption feature and material carrying REEs

The absorption feature centred at 674nm was suspected to be originated from Er, and several results verified this idea. First, Pearson correlation coefficients between Er and spectral parameters (band ratio_{712/674}, band depth₆₇₄, and band area₆₀₀₋₇₁₂) in a logarithmic scale show a positive correlation (0.829, 0.689, and 0.710 respectively). Second, the absorption features related to REEs were characterized by a narrow absorption feature, as a result of 4f-4f intraconfigurational electron transitions (Turner et al., 2014), and the width of the 674 absorption feature is about 50nm. Also, the concentration of Er was remarkably higher than that of other REEs. Silicon, albeit the main constituent of samples, does not have diagnostic features in the VNIR wavelength range (Sabins, 1999). It is also possible that Er absorption feature centred at 651nm in Xenotime spectra shifts to 674nm when Er is incorporated into Quartz, given the fact that Turner et al. (2014, 2016) encountered a shift in the depth of absorption feature in different REE-bearing minerals.

Regarding the question of which grains carry REE, several conditions could be explained. The first condition is that REEs are coating Quartz grains. However, REE concentrations in water-leached samples were significantly low compared to REE concentrations in total concentration samples. If REEs coat Quartz grain, REE concentrations in water-leached and total concentration samples should be comparable. The second condition is that samples might mainly consist of pure Quartz grains and few unknown grains that carry REEs. As different grains were pulverized, they are mixed. During ASD spectrometer, XRD, FTIR-ATR and ICP-OES measurements, they are measured as a mixed powder of different grains.

However, this condition is unlikely because the 674nm absorption feature that is caused by Er is present in all 126-grain samples measured with the hyperspectral imaging camera. From Table 7, it appeared that Sc, Y, La, Ce, and Nd concentrations had a significant correlation with FTIR-ATR absorbance spectra. A possible explanation for this high correlation between La, Ce Nd, and three peaks of absorbance spectra (Figure 12b) is that REEs might be incorporated into Quartz lattice. This also explains the low solubility of REEs because they are possibly bound by Silicon.

5.7. REE detectability by satellite remote sensing sensors

Laboratory spectra were resampled to WorldView2, Landsat 8 OLI, and Sentinel-2 MSI spectral resolution and the results were visually inspected (Figure 22). In the WorldView2 and Sentinel-2 MSI resampled spectra, the absorption feature at 674nm related to Er was still retained at band 5 of WorldView2 and band 4 of Sentinel-2 MSI. Although the 674nm absorption feature caused a low value at band 4 of the Landsat 8 OLI resampled spectra, it was not as distinct as the absorption feature in WorldView2 and Sentinel-2 MSI resampled spectra.

From Table 11, the spectral parameter values calculated from the WorldView2 and Sentinel-2 MSI resampled spectra had a significant correlation with Er concentration in the samples of location 2 and 3 with an r-value between 0.486 and 0.738. Meanwhile, only the band ratio of the Landsat 8 OLI resampled spectra had a significant correlation with Er concentration in the samples of location 2 and 3 with an r-value of 0.723. It is the low spectral resolution of Landsat 8 OLI with 4 bands covering the VNIR wavelength range that is suspected to be the reason for band depth and band math having no correlation with Er concentration. Given this result, a satellite sensor with the spectral specification as same as Landsat 8 OLI is not likely to be able to discriminate the 674nm absorption feature related to Er.

In this case, a satellite sensor with the spectral specification the same as or higher than WorldView2 and Sentinel-2 MSI is needed to target the 674nm absorption feature. It is because WorldView2 and Sentinel-2 MSI with 8 bands laid in the VNIR wavelength range were able to isolate the 674nm absorption feature, as shown in Figure 22a. However, having 8 bands in the VNIR wavelength range, a satellite sensor is not guaranteed to be able to target another REE absorption feature. Figure 22b exemplified this case. In the WorldView2 resampled spectra of Xenotime, the Nd absorption feature at around 745nm was not detected, while in the Sentinel-2 MSI resampled spectra of Xenotime, both absorption features of Er and Nd were detected. It is the position and bandwidth of Sentinel-2 MSI band that coincidentally fit with the position of REE absorption features in the spectra of tailing samples and Xenotime. Thus, it preserves the REE absorption features.

Figure 23 compares the spatial resolution of the Sentinel-2 MSI and Landsat 8 OLI by displaying location 1, 2, and 3. In this study, location 2 was the smallest area with the size of 450m x 250m, and the Landsat 8 OLI had the lowest spatial resolution with a 30m spatial resolution. The spatial resolution of the Sentinel-2 MSI band 1, 9, and 10 is 60m, but these bands were not used, and the 20 spatial resolution of the

Sentinel-2 MSI band 5, 6, 7, and 8a was resampled to 10m. As shown in Figure 23e, several pixels of the Landsat 8 OLI image were located inside the location 2. Considering this, it was expected that a 30m spatial resolution of the Landsat 8 OLI should suffice; however, in a case where vegetation is present, a higher spatial resolution might be required for this study.

5.8. Application to multispectral images

As shown in Figure 25, the vegetation area in location 1 and 3 was masked in the Sentinel-2 MSI image, but not in the Landsat 8 OLI image. Compared to the 10m spatial resolution of Sentinel-2 MSI, Landsat 8 OLI image has a 30m spatial resolution. Because of this, Landsat 8 OLI was unable to detect vegetation area whose size is around 10m (Sentinel-2 MSI spatial resolution). This result confirmed that a satellite sensor with the spatial resolution higher than 30m is required. A 10m spatial resolution can be a guide to determine the minimum specification of a satellite sensor to discriminate vegetation in the study area as Sentinel-2 MSI with the 10m spatial resolution demonstrated to be able to mask a tree (Figure 24).

The NDVI threshold could also be the reason for the inability of Landsat 8 OLI to mask the vegetation area. Landsat 8 OLI image had an NDVI threshold of 0.1883, which is almost double the NDVI threshold in Sentinel-2 MSI image (0.09697). When the NDVI threshold for Landsat 8 OLI was lowered, however, not only was vegetation masked but also tailing area was. Similar to vegetation, tailing has an absorption feature at band 4 due to REE and the low spectral resolution of Landsat 8 OLI is unable to discriminate them.

Figure 26 compares the colour composite images of band ratio, depth, and math derived from the Sentinel-2 MSI and Landsat 8 OLI. In this image, a white colour indicates a pixel with absorption in the Sentinel-2 MSI and Landsat 8 OLI band 4, which is related to Er. Another absorption feature was also detected at band 6 (740nm) present together with the absorption feature at band 4 in the spectral reflectance of several white pixels of the Sentinel-2 MSI composite images. In the composite images of spectral parameters derived from the Landsat 8 OLI image, all pixels were white, meaning an absorption feature is present at band 4 of Landsat 8 OLI. However, this absorption feature was probably originated from not only the Er absorption feature, but also other absorption feature.

Figure 27 shows that three absorption features can be found at band 4(665nm), band 5(704nm), and band 6(740nm) of the Sentinel-2 MSI image. These three absorption features were suspected to cause the absorption feature at band 4 of Landsat 8 OLI. For example, in the absence of the absorption feature at band 4(665nm) of the Sentinel-2 MSI image, the shoulder of the absorption feature at band 5 (704nm) of Sentinel-2 MSI could be recorded as an absorption feature at band 4 (654nm) of Landsat 8 OLI image.

These results ascertained that a satellite sensor with the spectral and spatial resolution as same as Landsat 8 OLI is not designed for this study. A satellite sensor with the spectral and spatial resolution (10m) identical to Sentinel-2 MSI is adequate. A satellite sensor with the spatial resolution (1.84m) of WorldView2 will perform better than that of Sentinel-2 MSI; however, in terms of spectral capability, the spectral resolution of Sentinel-2 MSI is superior to that of WorldView2 for this study.

To discriminate the absorption feature at band 4 of the Sentinel-2 MSI image, three spectral parameters (band ratio, depth, and math) were defined, and the images of spectral parameter products were displayed as a colour composite image. This algorithm successfully indicated a pixel with an absorption feature at band 4 of the Sentinel-2 MSI image that appears white. However, this algorithm was not able to identify two other absorption features at band 5 and 6 of Sentinel-2 MSI as it was designed not for this purpose. Another algorithm was developed, and the results are discussed in Chapter 6.

5.9. The origin of absorption features at band 4, 5, and 6 of the Sentinel-2 MSI image

The absorption feature at band 4 of the Sentinel-2 MSI image is originated from the presence of Er as the results of this study already showed. The absorption feature at band 6 (740nm) of the Sentinel-2 MSI image is most likely due to Nd, Sm, and Dy. In the spectral reflectance of the samples of location 2 and 3 before milling, we observed an absorption feature centred at 745nm related to Nd, Sm, and Dy. Unfortunately, no statistical correlation was established between the 745nm absorption feature and Nd, Sm, and Dy concentrations because Nd, Sm, and Dy concentrations were below the limit of detection in most of the samples. Nevertheless, the Sentinel-2 MSI resample spectra of Xenotime showed a distinct absorption feature at band 6. Regarding the absorption feature at band 5 (704nm) of the Sentinel-2 MSI image, it is discussed in Chapter 6.

6. DISCRIMINATING THREE ABSORPTION FEATURES

Chapter 4 showed that three absorption features at band 4, 5, and 6 can be found in the Sentinel-2 MSI image. However, the two of these absorption features were not discussed in the chapter 5, because the absorption feature at band 5 (704nm) was not present in laboratory spectra. Meanwhile, the absorption feature at band 6 (740nm) was suspected related to Nd, Sm, Dy, and Ho, but no linear statistical correlations were performed, because Nd, Sm, and Dy concentrations were below the limit of detection in most of the samples. In this chapter, the three absorption features in Sentinel-2 MSI image were further analysed.

The heating experiment was performed to confirm whether or not a possibility of the 674nm absorption feature undergoing a band shift to around 705nm or a possibility of appearing a new absorption feature at around 705nm is plausible. However, no change was observed in the spectral reflectance of the 5 extra samples. Therefore, the origin of the absorption feature at band 5 of the Sentinel-2 MSI image is still unidentified.

In the previous chapter, three spectral parameters (band ratio, band depth, and band math) were used simultaneously to target the absorption feature at band 4. However, these three spectral parameters could not discriminate the two other absorption features at band 5 and 6. For example, white color in Figure 28a indicated a pixel with an absorption feature at band 4 (Figure 28b), but it could not indicate whether or not the white pixel also has another absorption feature at band 6 in its spectra (Figure 28c).

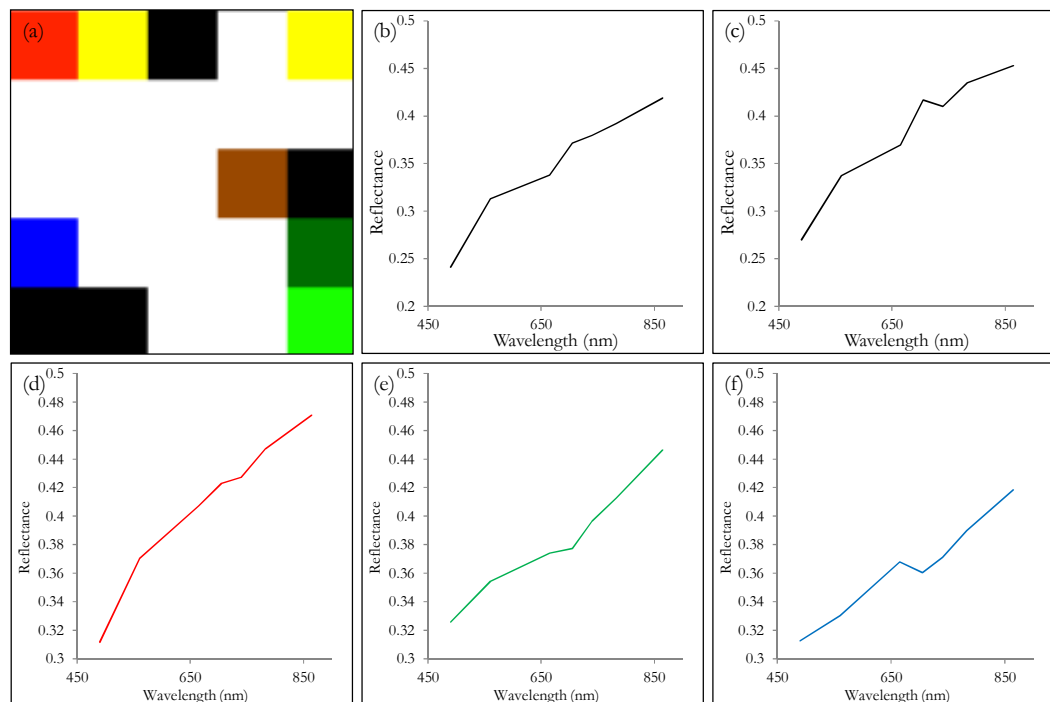


Figure 28 a) Subset Figure 26b. b) White colour indicated the spectral reflectance with an absorption feature at band 4. c) However, the white pixel could not indicate whether or not it has absorption features at band 4 and 6 in its spectra. The spectral reflectance of red, green, and blue pixels is shown in d), e) and f) respectively.

Another algorithm was developed by improving band math with a condition applied. Figure 29 compares the RGB colour composite of band ratio, band depth, and band math to the RGB colour composite of improved band math calculated from a Sentinel-2 MSI image. As shown in Figure 29a-c, a white colour

indicated a pixel with an absorption feature at band 4. Similarly, red colour in Figure 29d-f indicated a pixel with an absorption feature at band 4. However, several white pixels in Figure 29a-c were not indicated as red, but magenta in Figure 29d-f. This is because these white pixels in fact also had an absorption feature at band 4 and 6. In Figure 29d-f, a pixel with an absorption feature at band 6 in its spectral reflectance appeared blue. Meanwhile, a pixel with an absorption feature at band 5 in its spectral reflectance appeared green in Figure 29d-f, but green colour pixels in Figure 29a-c cannot be interpreted in that way.

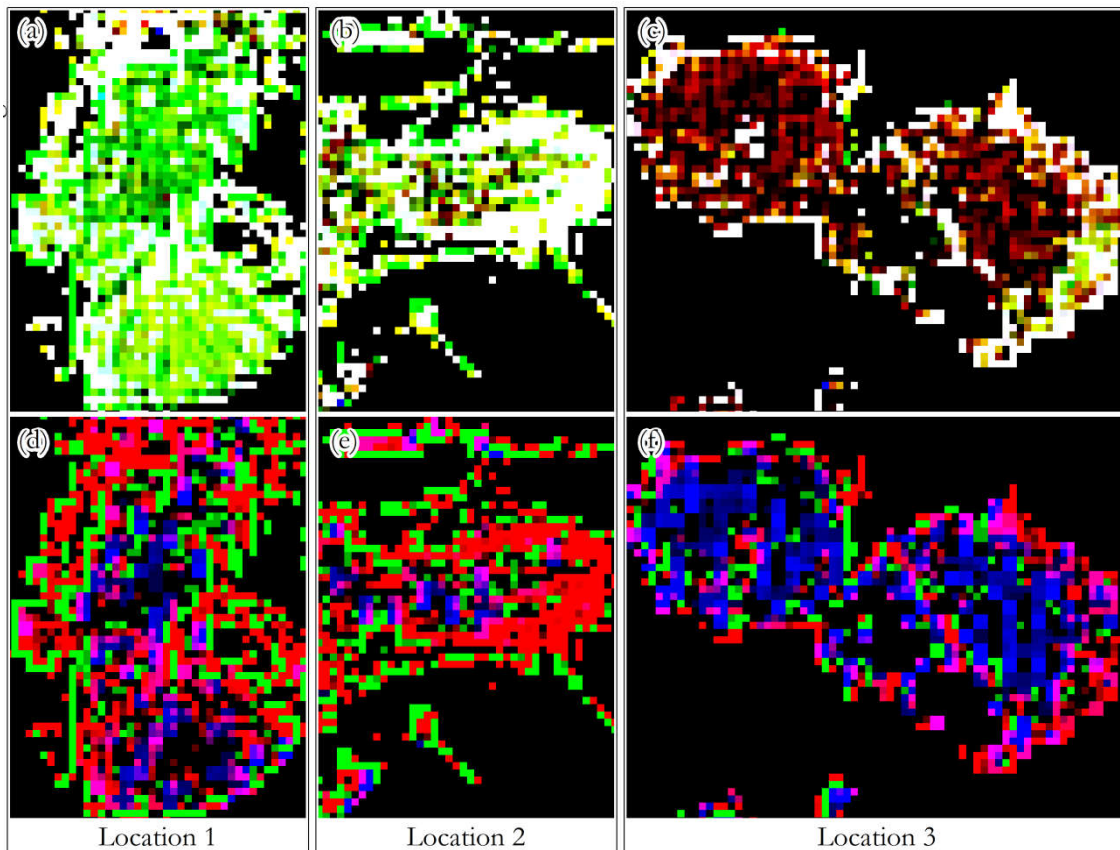


Figure 29 Colour composite images of band ratio, depth, and math derived from the Sentinel-2 MSI image (a-c). A linear stretch was applied to the images, and the thresholds value for band ratio was (1.0001) ■ *high* (1.05) , for band depth was *low* (0) ■ *high* (0.02) , for band math was *low* (0) ■ *high* (0.0004) . Colour composite of improved band math $((B_3-B_4) \times (B_5-B_4))$, $((B_4-B_5) \times (B_6-B_5))$, $((B_5-B_6) \times (B_7-B_6))$ (d-f). The thresholds values of the linear stretch for improved band math images are *low* (0) ■ *high* (0.0004) . In Figure 29a-c, white pixels indicate a pixel with an absorption feature at band 4. In Figure 29d-f, absorption features at band 4, 5, and 6 are represented by red, green, and blue colours respectively. Magenta pixel indicates a pixel with absorption features at band 4 and 6.

7. CONCLUSION AND RECOMMENDATION

7.1. Conclusion

In this research, the obtained samples were identified as Quartz; nevertheless, they contained a high amount of Er. As Quartz, the spectral reflectance of the obtained samples in the VNIR wavelength range should be featureless, yet an absorption feature centred at around 674nm was observed in all samples. It is Er that causes the 674nm absorption feature. A satellite remote sensing with the spectral and spatial resolution similar or higher than Sentinel-2 MSI is sufficient for this study. Algorithms were developed to identify a pixel with the 674nm absorption feature, and we found that they performed well. The following is the answers of the research.

1. What can REEs be found in tailing samples?
All REEs were found in collected tailing samples except for Promethium which does not naturally occur. Thulium and Praseodymium showed signal intensity during ICP-OES measurements but were not reported to signal interference.
2. How significant is the effect of water leaching on the total concentration of REE?
REE concentrations in leached samples were only a half percent or less than REE concentration in total concentrations – even though samples were pulverized and stirred.
3. Which of REE absorption features can be detected in the VNIR wavelength range?
A new REE absorption feature related to Er was observed centred at around 674nm. Absorption features related to Nd, Sm, and Dy were observed, but not distinct due to low concentration.
4. How do the absorption features in the VNIR wavelength range change with changing the concentration of REE?
The depth of the 674nm absorption feature becomes deeper as Er concentration in the analysed sample become higher. As 674nm absorption feature goes deeper, the absorption feature becomes double.
5. What are spectral and spatial specifications needed for a sensor to detect REEs in this study area?
After comparing the performance of Sentinel-2MSI and Landsat 8 OLI, the spectral and spatial specifications of a satellite sensor for detecting REEs were determined. A satellite sensor with the 10m spatial resolution and 8 detectors with equivalent to Sentinel-2 MSI are needed for this study.
6. Which of currently available sensors qualify for detecting REEs in the study area?
Sentinel-2 MSI meets both spectral and spatial qualifications, and we satisfied with the result of using Sentinel-2 MSI. WorldView2, albeit was not evaluated its image, will performed better than Sentinel-2 MSI in terms of spatial aspect, but its performance regarding spectral aspect is only enough to target the 674nm absorption feature but not the 745nm absorption feature. Meanwhile, Sentinel-2 MSI is able to discriminate both absorption features.

7.2. Recommendations

The similar physical and chemical properties of REEs impede their quantification with ICP-OE. No standard procedure was defined yet to quantify REEs in geological samples, especially our samples. Therefore, the first recommendation is to develop a better technique to quantify REE in tailing samples using ICP-OES.

The limit of detection and signal interference were the main issue when we quantified REEs in our samples using ICP-OES. To minimize this problem, it is recommend to utilize better equipment, for example, ICP-MS. In this study, we quantified REE concentrations by using a multi-REEs calibration standard which is a mix of all REE. For the next similar study, a single REE calibration standard will help in determining candidate wavelength of ICP-OES and will have signal intensity without interference.

This study successfully targeted REE-bearing mineral using satellite remote sensing data; however, this study was only a forerunner of the spectroscopy study of REE-bearing tailings in the study area. It is because the results of this study give us more questions than answers. Of two data sets, only one data set had a correlation with the 674 absorption feature. Therefore, another experiment is needed to confirm this result.

In the Sentinel-2 MSI image, we observed an absorption feature at band 5 (705nm), but not in laboratory spectra, even though five samples were taken corresponding to the location of pixels that have the absorption feature at band 5 of the Sentinel-2 MSI image. This absorption feature is worth to be explored further by bringing ASD spectrometer or hyperspectral camera to the study area. After identifying material causing this absorption feature, it should be further analysed their chemical composition.

LIST OF REFERENCES

- Adams, J. B., & Filice, A. L. (1967). Spectral reflectance 0.4 to 2.0 microns of silicate rock powders. *Journal of Geophysical Research*, 72(22), 5705–5715.
- Adams, J. W. (1965). The visible region absorption spectra of rare earth minerals. *American Mineralogist*, 50, 356–366.
- Anders, E., & Grevesse, N. (1989). Abundances of the elements: Meteoritic and solar. *Geochimica et Cosmochimica Acta*, 53(1), 197–214.
- Barakos, G., Gutzmer, J., & Mischo, H. (2016). Strategic evaluations and mining process optimization towards a strong global REE supply chain. *Journal of Sustainable Mining*, 15, 26–35.
- Bedini, E. (2009). Mapping lithology of the Sarfartoq carbonatite complex, southern West Greenland, using HyMap imaging spectrometer data. *Remote Sensing of Environment*, 113(6), 1208–1219.
- Ben-Dor, E., Irons, J. ., & Epema, G. F. (1999). Soil Reflectance. In A. N. Rencz (Ed.), *Remote sensing for the earth sciences: Manual of remote sensing* (p. 111–188). New York: John Wiley & Sons.
- Boesche, N. K., Rogass, C., Christian, M., Lubitz, C., Brell, M., Herrmann, S., Körtling, F., Papenfuss, A., Tonn, S., Altenberger, U., & Guanter, L. (2016). Rare earth element detection from near-field to space - samarium detection using the REEMAP algorithm. In *2016 IEEE International Geoscience and Remote Sensing Symposium (IGARSS)* (pp. 5414–5417).
- Boesche, N. K., Rogass, C., Lubitz, C., Brell, M., Herrmann, S., Mielke, C., Tonn, S., Appelt, O., Altenberger, U., & Kaufmann, H. (2015). Hyperspectral REE (rare earth element) mapping of outcrops-applications for neodymium detection. *Remote Sensing*, 7(5), 5160–5186.
- Boesche, N. K., Rogass, C., Mielke, C., Herrmann, S., Körtling, F., Papenfuß, A., Lubitz, C., Brell, M., Tonn, S., & Altenberger, U. (2015). Hyperspectral Rare Earth Element Mapping of Three Outcrops at the Fen Complex, Norway: Calcitic, Dolomitic, and Ankeritic Carbonatites. In *Rare Earths Industry: Technological, Economic, and Environmental Implications* (pp. 235–265). Elsevier.
- Bowers, T. L., & Rowan, L. C. (1996). Remote Mineralogic and Lithologic Mapping of the Ice River Alkaline Complex , British Columbia , Canada , Using AVIRIS Data. *Photogrammetric Engineering & Remote Sensing*, 62(12), 1379–1385.
- Camacho-Tamayo, J. H., Rubiano S., Y., & Hurtado S., M. del P. (2014). Near-infrared (NIR) diffuse reflectance spectroscopy for the prediction of carbon and nitrogen in an Oxisol. *Agronomía Colombiana*, 32(1), 86–94.
- Castor, S. B. (2008). The Mountain Pass rare-earth carbonatite and associated ultrapotassic rocks, California. *Canadian Mineralogist*, 46(4), 779–806.
- Chen, W., Honghui, H., Bai, T., & Jiang, S. (2017). Geochemistry of Monazite within Carbonatite Related REE Deposits. *Resources*, 6(4), 51. Retrieved from <http://www.mdpi.com/2079-9276/6/4/51>
- Clark, R. N. (1995). Reflectance Spectra. In T. J. Ahrens (Ed.), *Rock physics and phase relations: A handbook of physical constants* (pp. 178–188). Florida: American Geophysical Union.
- Clark, R. N., King, T. V., & Gorelick, N. S. (1987). Automatic Continuum Analysis of Reflectance Spectra. *JPL Proceedings of the 3rd Airborne Imaging Spectrometer Data Analysis Workshop*, 138–142.
- Clark, R. N., Swayze, G. A., Wise, R., Livo, K. E., Hoefen, T. M., Kokaly, R. F., Sutley, S. J., Survey, U. S. G., & Title, S. (2007). USGS Digital Spectral Library splib06a. Retrieved October 3, 2017, from <https://speclab.cr.usgs.gov/spectral.lib06/ds231/datatable.html>
- Crowley, J. K., Brickey, D. W., & Rowan, L. C. (1989). Airborne imaging spectrometer data of the Ruby Mountains, Montana: Mineral discrimination using relative absorption band-depth images. *Remote Sensing of Environment*, 29(2), 121–134.
- Dasher, D. H. (2014). Use of Regional Geochemical Survey Data and exploratory statistics to estimate natural condition concentrations for trace metals in stream sediments: a case study for the Cook Inlet watershed, Alaska. *Environmental Earth Sciences*, 72(11), 4335–4344.
- Dindal, A. B., Bayne, C. K., & Jenkins, R. A. (1999). *Environmental Technology Verification Report: Immunoassay Kit EnviroLogix, Inc. PCB in Soil Tube Assay*. Washington, DC.
- Eid, M. A., Naim, G., Mahdy, A. A., Nada, N., & Abdel Mongy, S. (1994). Application of ICP AES to the determination of REE in Egypt's black sand deposits. *Journal of Alloys and Compounds*, 207–208(C), 482–486.
- Falagán, C., Grail, B. M., & Johnson, D. B. (2017). New approaches for extracting and recovering metals

from mine tailings.

- Flem, B., Larsen, R. B., Grimstvedt, A., & Mansfeld, J. (2002). In situ analysis of trace elements in quartz by using laser ablation inductively coupled plasma mass spectrometry. *Chemical Geology*, 182(2–4), 237–247.
- Goetz, A. F. H., Rock, B. N., & Rowan, L. C. (1983). Remote sensing for exploration; an overview. *Economic Geology*, 78(4), 573–590.
- Hapke, B. (1993). *Theory of reflectance and emittance spectroscopy*. Cambridge: Cambridge University Press.
- Haque, N., Hughes, A., Lim, S., & Vernon, C. (2014). Rare Earth Elements: Overview of Mining, Mineralogy, Uses, Sustainability and Environmental Impact. *Resources*, 3, 614–635.
- Hatje, V., Bruland, K. W., & Flegal, A. R. (2016). Increases in Anthropogenic Gadolinium Anomalies and Rare Earth Element Concentrations in San Francisco Bay over a 20 Year Record. *Environmental Science & Technology*, 50(8), 4159–4168.
- Helsel, D. (2010). Much ado about next to nothing: Incorporating nondetects in science. *Annals of Occupational Hygiene*.
- Hunt, G. R. (1977). Spectral Signatures of Particulate Minerals in the Visible and Near Infrared. *GEOPHYSICS*, 42, 501–513.
- Ko, U. K. (1986). Preliminary synthesis of the geology of Bangka Island, Indonesia. In *GEOSEA* (pp. 82–96).
- Lafuente, B., Downs, R. T., Yang, H., & Stone, N. (2015). The power of databases: The RRUFF project. In T. Armbruster & R. M. Danis (Eds.), *Highlights in Mineralogical Crystallography* (pp. 1–30). Berlin: W. De Gruyter.
- Lottermoser, B. G. (2010). *Mine Wastes: Characterization, treatment, and environmental impacts* (3rd ed.). Heidelberg: Springer.
- MacMillan, G. A., Chételat, J., Heath, J. P., Mickpegak, R., & Amyot, M. (2017). Rare earth elements in freshwater, marine, and terrestrial ecosystems in the eastern Canadian Arctic. *Environ. Sci.: Processes Impacts*, 19(10), 1336–1345.
- Makombe, M., Horst, C. van der, Silwana, B., Iwuoha, E., & Somerset, V. (2017). Optimisation of Parameters for Spectroscopic Analysis of Rare Earth Elements in Sediment Samples. In J. E. A. Orjuela (Ed.), *Rare Earth Element*. InTech.
- Mancheri, N. A. (2012). Chinese Monopoly in Rare Earth Elements: Supply–Demand and Industrial Applications. *China Report*, 48(4), 449–468.
- Massari, S., & Ruberti, M. (2013). Rare earth elements as critical raw materials: Focus on international markets and future strategies. *Resources Policy*, 38(1), 36–43.
- Myers, R. (2013). *The Basics of Chemistry*. Westport: Greenwood Press.
- Narendra, B. H., & Pratiwi. (2016). Adaptability of some legume trees on quartz tailings of a former tin mining area in Bangka Island, Indonesia. *Journal of Degraded and Mining Lands Management*, 4(1), 671–674.
- Navarro, M. S., Ulbrich, H. H. G. J., Andrade, S., & Janasi, V. A. (2002). Adaptation of ICP-OES routine determination techniques for the analysis of rare earth elements by chromatographic separation in geologic materials: Tests with reference materials and granitic rocks. In *Journal of Alloys and Compounds* (Vol. 344, pp. 40–45).
- Neave, D. A., Black, M., Riley, T. R., Gibson, S. A., Ferrier, G., Wall, F., & Broom-Fendley, S. (2016). On the Feasibility of Imaging Carbonatite-Hosted Rare Earth Element Deposits Using Remote Sensing. *Economic Geology*, 111(3), 641–665.
- O'Neill, H. S. C. (2016). The Smoothness and Shapes of Chondrite-normalized Rare Earth Element Patterns in Basalts. *Journal of Petrology*, 57(8), 1463–1508.
- Paulick, H., & Machacek, E. (2017). The global rare earth element exploration boom: An analysis of resources outside of China and discussion of development perspectives. *Resources Policy*, 52, 134–153.
- Popek, E. . (2013). *Sampling and analysis of environmental chemical pollutants. Ecosystems and Human Well-being: A Framework for Assessment* (Vol. 12). Academic Press.
- Ramos, S. J., Dinali, G. S., Oliveira, C., Martins, G. C., Moreira, C. G., Siqueira, J. O., & Guilherme, L. R. G. (2016). Rare Earth Elements in the Soil Environment. *Current Pollution Reports*, 2(1), 28–50.
- Rim, K. T., Koo, K. H., & Park, J. S. (2013). Toxicological Evaluations of Rare Earths and Their Health Impacts to Workers: A Literature Review. *Safety and Health at Work*, 4(1), 12–26.
- Rodionova, O. Y., Tikhomirova, T. I., & Pomerantsev, A. L. (2015). Spectrophotometric determination of

- Rare Earth Elements in aqueous nitric acid solutions for process control. *Analytica Chimica Acta*, 869, 59–67.
- Rollison, H. R. (1993). *Using Geochemical Data: Evaluation, Presentation, Interpretation*. Harlow: Longman.
- Rowan, L. C., Bowers, T. L., Crowley, J. K., Anton-Pacheco, C., Gumiel, P., & Kingston, M. J. (1995). Analysis of airborne visible-infrared imaging spectrometer (AVIRIS) data of the Iron Hill, Colorado, carbonatite-alkalic igneous complex. *Economic Geology*, 90(7), 1966–1982.
- Rowan, L. C., & Mars, J. C. (2003). Lithologic mapping in the Mountain Pass, California area using Advanced Spaceborne Thermal Emission and Reflection Radiometer (ASTER) data. *Remote Sensing of Environment*, 84(3), 350–366.
- Rowan, L. C., Wetlaufer, P., Goetz, A., Billingsley, F., & Stewart, J. (1974). *Discrimination of rock types and altered areas in Nevada by the use of ERTS images*. Geological Survey Professional Paper 883.
- Sabins, F. F. (1999). Remote sensing for mineral exploration. *Ore Geology Reviews*, 14(3), 157–183.
- Szamalek, K., Konopka, G., Zglinicki, K., & Marciniak-Maliszewska, B. (2013). New Potential Source of Rare Earth Elements. *Gospodarka Surowcami Mineralnymi - Mineral Resources Management*, 29(4), 59–76.
- Taylor, S. ., & McLennan, S. . (1995). The geochemical evolution of the continental crust. *Reviews of Geophysics*, 33(2), 241–265.
- Tepe, N., Romero, M., & Bau, M. (2014). High-technology metals as emerging contaminants: Strong increase of anthropogenic gadolinium levels in tap water of Berlin, Germany, from 2009 to 2012. *Applied Geochemistry*, 45, 191–197.
- Turner, D. (2015). *Reflectance spectroscopy and imaging spectroscopy of rare earth element-bearing mineral and rock samples*. The University of British Columbia.
- Turner, D. J., Rivard, B., & Groat, L. A. (2014). Visible and short-wave infrared reflectance spectroscopy of REE fluorocarbonates. *American Mineralogist*, 99(7), 1335–1346.
- Turner, D. J., Rivard, B., & Groat, L. A. (2016). Visible and short-wave infrared reflectance spectroscopy of REE phosphate minerals. *American Mineralogist*, 101(10), 2264–2278.
- Upadhyay, S. K. (2006). *Chemical Kinetics and Reaction Dynamics*. New York: Springer.
- USGS. (2017). *Mineral Commodity Summaries*. <https://doi.org/10.3133/70180197>
- Van Gosen, B. S., Verplanck, P. L., Long, K. R., Gambogi, J., & Seal II, R. R. (2014). *The rare-earth elements—Vital to modern technologies and lifestyles*. U.S. Geological Survey Fact Sheet 2014–3078.
- Wang, C., Zhang, T., & Pan, X. (2017). Potential of visible and near-infrared reflectance spectroscopy for the determination of rare earth elements in soil. *Geoderma*, 306, 120–126.
- Wentworth, C. K. (1922). A Scale of Grade and Class Terms for Clastic Sediments. *The Journal of Geology*, 30(5), 377–392.
- Williams, P., & Sobering, D. (1993). Comparison of commercial near infrared transmittance and reflectance instruments for analysis of whole grains and seeds. *Journal of Near Infrared Spectroscopy*, 1(1), 25.
- Wübbecke, J. (2013). Rare earth elements in China: Policies and narratives of reinventing an industry. *Resources Policy*, 38(3), 384–394.
- Zawisza, B., Pytlakowska, K., Feist, B., Polowniak, M., Kita, A., & Sitko, R. (2011). Determination of rare earth elements by spectroscopic techniques: a review. *Journal of Analytical Atomic Spectrometry*, 26(12), 2373.
- Zuleger, E., & Erzinger, J. (1988). Determination of the REE and Y in silicate materials with ICP-AES. *Fresenius' Zeitschrift Für Analytische Chemie*, 332(2), 140–143.

8. APPENDIXES

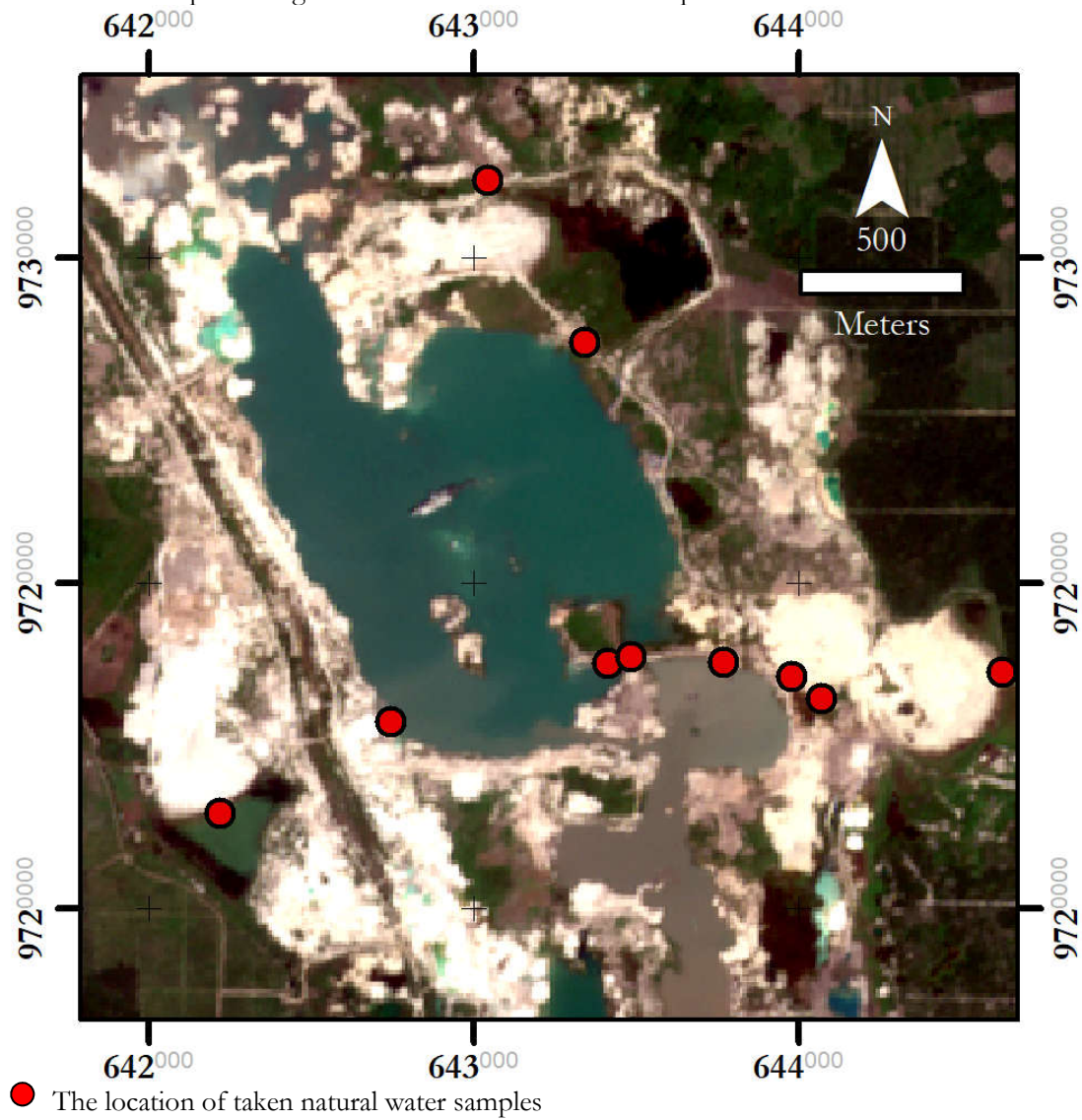
Appendix A Grain size

20 samples were divided into three groups based on their grain size, namely big grain size ($>1\text{mm}$), medium grain size ($1-0.1\text{mm}$), and small grain size (<0.1). According to a grain scale classification proposed by (Wentworth, 1922), big is equal to very coarse sand ($>1\text{mm}$), medium is equal to coarse-fine sand, and small is equal to very fine sand grain-clay particle (<0.1).

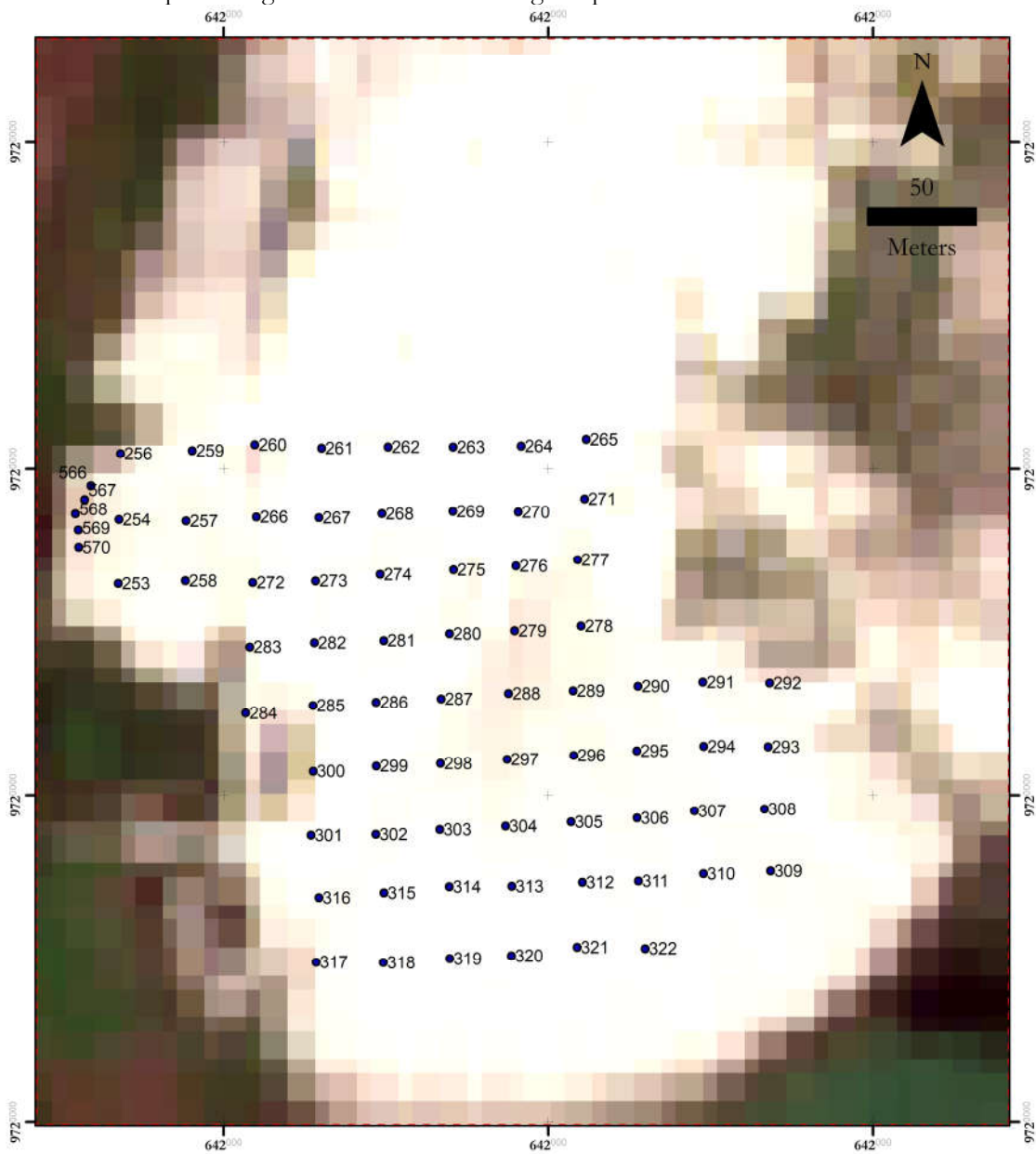
ID Sample	Weight (g)			Percentage		
	$>1\text{mm}$	$1-0.1\text{mm}$	$<0.1\text{mm}$	$>1\text{mm}$	$1-0.1\text{mm}$	$<0.1\text{mm}$
438	3.81	3.14	9.09	24%	20%	57%
425	5.80	3.14	8.26	34%	18%	48%
420	11.7	2.32	2.25	72%	14%	14%
418	10.4	1.87	3.42	66%	12%	22%
417	7.53	2.34	7.34	44%	14%	43%
416	4.48	2.56	9.31	27%	16%	57%
406	5.25	2.81	7.14	35%	18%	47%
404	5.29	2.81	7.14	35%	18%	47%
378	7.93	1.79	5.89	51%	11%	38%
377	5.61	3.11	6.32	37%	21%	42%
2	4.20	1.32	5.14	39%	12%	48%
379	9.10	2.34	5.51	54%	14%	33%
390	9.62	2.59	3.98	59%	16%	25%
395	5.85	3.74	5.08	40%	26%	35%
396	8.86	2.38	4.77	55%	15%	30%
399	2.86	3.01	8.76	20%	21%	60%
351	7.18	2.73	5.05	48%	18%	34%
375	7.87	2.72	5.30	50%	17%	33%
369	6.95	3.32	6.53	41%	20%	39%
349	7.50	3.34	6.44	43%	19%	37%
Average	6.89	2.67	6.14	44%	17%	39%

Appendix B Map showing the distribution of tailing and water sample

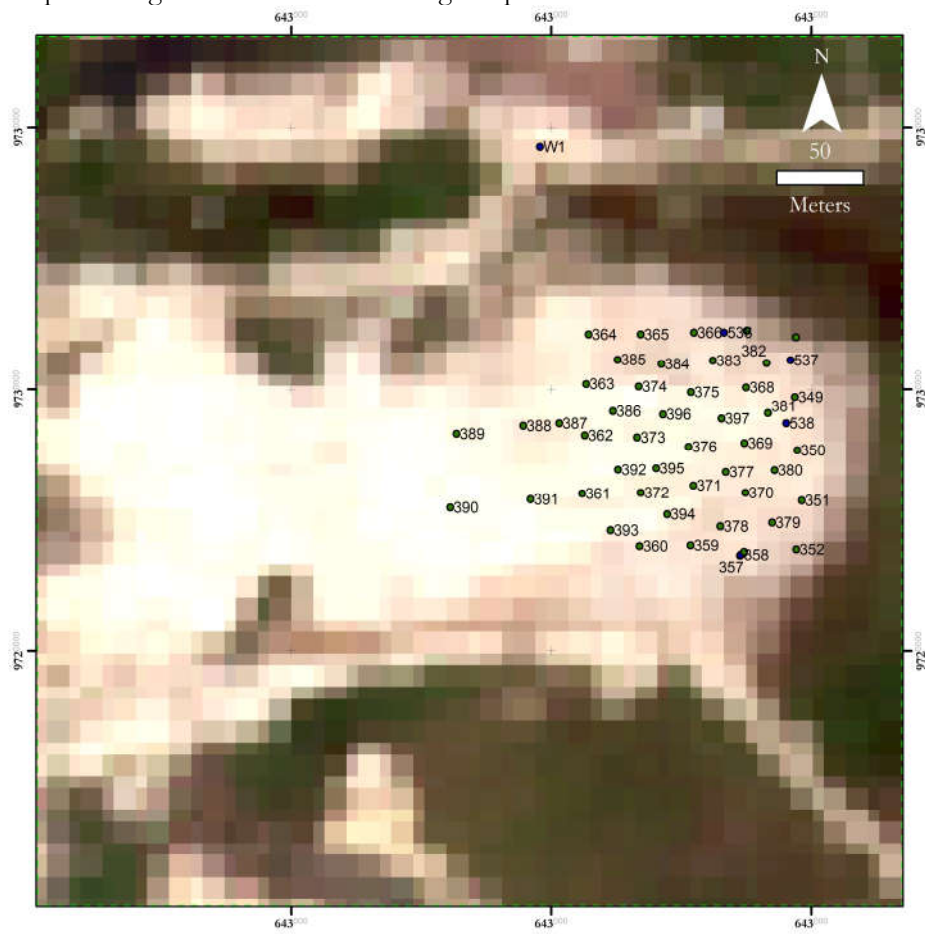
Below is the map showing the location of natural water samples.



Below is the map showing the distribution of tailing samples collected from location 1.

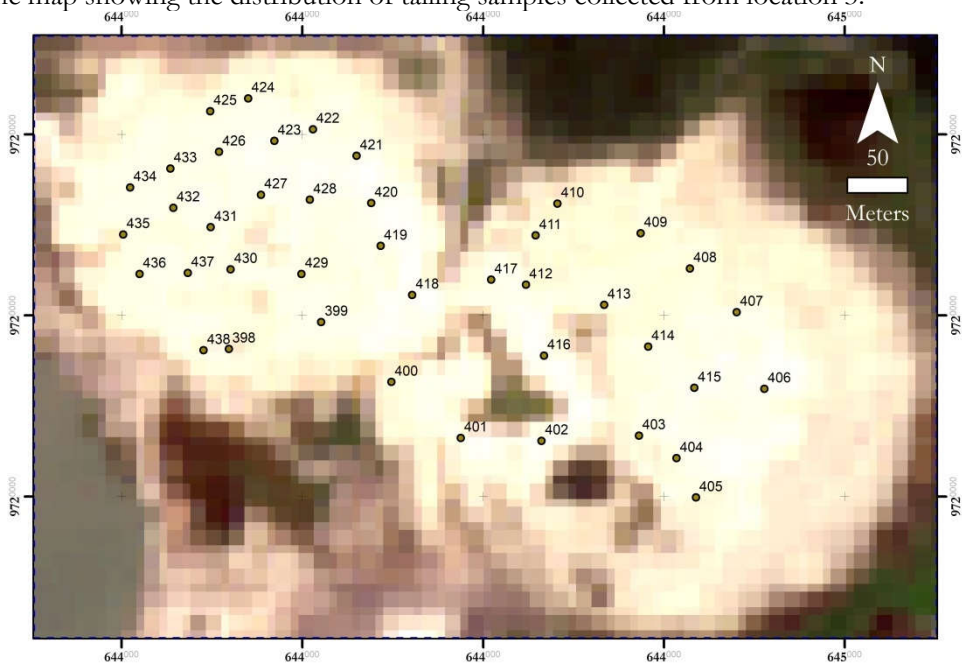


Below is the map showing the distribution of tailing samples collected from location 2.



● The location of taken natural water samples

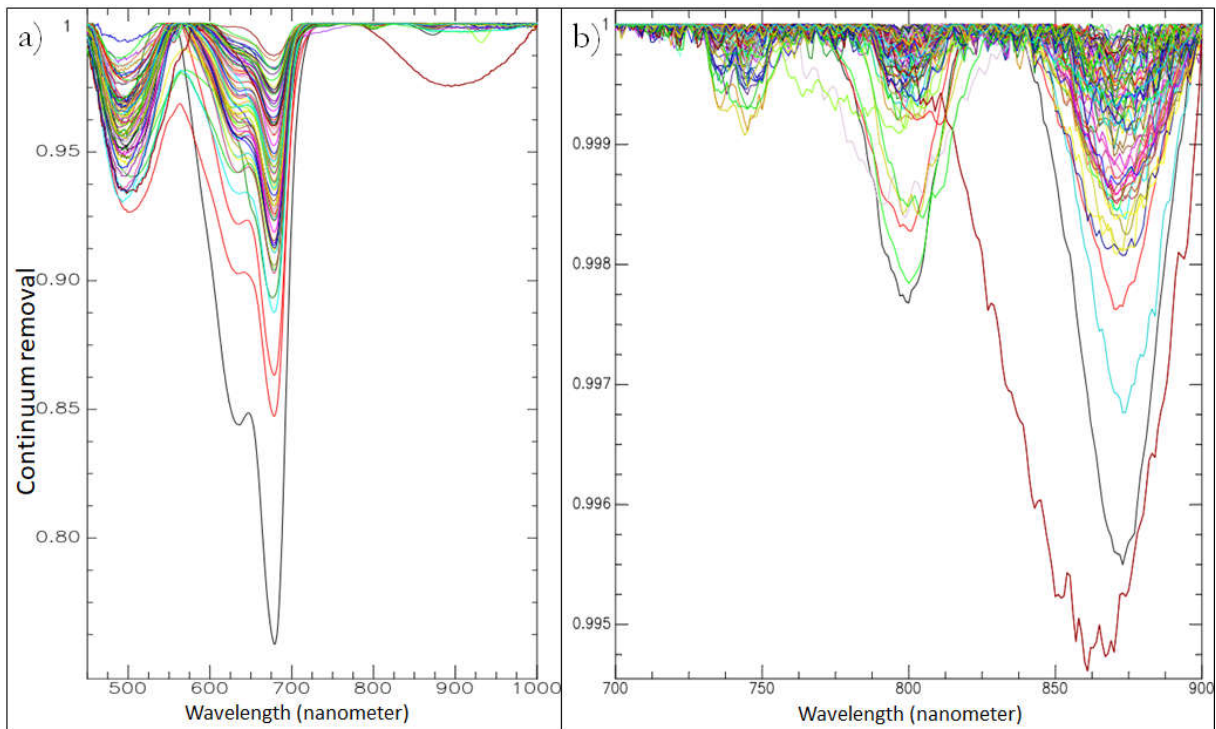
Below is the map showing the distribution of tailing samples collected from location 3.



● The location of taken natural water samples

Appendix C Procedure for selecting samples of location 2 and 3

Firstly, all samples were sieved and classified into three groups based on their particle sizes (big >1mm, medium 1-0.1mm, and small <0.1mm). These fractions were chosen because Szamalek et al. (2013) indicated that Xenotime and Monazite could be found in grain fraction <1mm. Secondly, every sieved sample was scanned using ASD spectrometer, and obtained spectra were directly continuum removed without any processing. Attention was paid to absorption features centred at 745nm, 801nm, and 873nm, because according to Neave et al. (2016), these three absorption features are due to Nd and Nd serves a pathfinder element for REEs. Lastly, 40 samples with three absorption features centred at 745nm, 801nm, and 873nm in their spectra were ground and sieved to <0.25mm.



Obtained spectra of coarse-grained samples from location 2 and 3 before pulverized. Continuum removal was applied from 450nm to 1000. a) Two absorption features centred at 500nm and 674nm are present in all spectra. The depth of the absorption feature centred at 674nm reaches 0.23. b) Three absorption features centred at 745nm, 801nm, and 873nm are suspected due to Nd, Sm, and Dy. The depth of the three absorption features is less than 0.005. Samples with the three absorption features centred at 745nm, 801nm, and 873nm in their spectra were chosen for the following analysis.

Appendix D The created scripts

The script for producing Figure 19.

```
m(list=ls())
library(RStoolbox)
library(readr)
library(MESS)
library(readxl)
library(psych)
library(xlsx) #load the package
library(hsdr) #spectral resample
library(prospectr)

a <- c("lib_450_1000_loc1", "lib_450_1000_loc23")

for(q in a){
  data_path <- "C:\\bangka\\lab\\Analysis5_overallspectravslCP"
  setwd("C:\\bangka\\lab\\Analysis5_overallspectravslCP")
  speclib <- paste0("C:/bangka/lab/Analysis5_overallspectravslCP/", q)
  sli <- readSLI(speclib)

  cr_wav <- data.frame(sli[1])
  cr_spec <- sli[-1]
  rownames(cr_spec) <- cr_wav[,1]
  rownames(sli) <- cr_wav[,1]

  cr_wav2 <- data.frame(sli[1])
  cr_spec2 <- sli[-1]
  for(z in 1:ncol(cr_spec2)){
    cr_spec2[z] <- data.frame(continuumRemoval(cr_spec2[[z]], cr_wav2[[1]], type = "R")) }
  for(y in 1:ncol(cr_spec2)){cr_spec2[y] <- log(cr_spec2[y]) }
  sli2 <- rbind(colnames(cr_spec2), cr_spec2)
  sli2 <- t(sli2)
  colnames(sli2)[1] <- "ID"

  labresult <- "C:/bangka/lab/Analysis5_overallspectravslCP/ICP.xlsx"
  labr <- read_excel(labresult, col_names = TRUE)
  labr2 <- labr[c(2:6, 13, 19)]
  labr2[labr2 == 0] <- NA
  for(x in 1:ncol(labr2)){labr2[x] <- log(labr2[x])}
  labr <- cbind(labr[1], labr2)
  join <- merge(labr, sli2)

  join_lab <- join[2:8]
  join_spectra <- join[c(2, 9:ncol(join))]
  nume <- join_spectra[2:ncol(join_spectra)] # convert all character to number
  for(t in 1:ncol(nume)){nume[t] <- as.numeric(as.character(nume[t]))}
  join_spectra[2:ncol(join_spectra)] <- nume

  for(u in 1:ncol(join_lab)){
    print(colnames(join_lab)[u])
    t <- corr.test(as.matrix(join_spectra), as.matrix(join_lab[u]),
      use = "pairwise", method = "pearson", alpha = .05, adjust = "none")

    data <- data.frame(t$n, t$p, (t$r*-1))
    write.xlsx(data, file = paste0(q, "_para.xls"), sheetName = colnames(join_lab)[u], append = TRUE, row.names = TRUE)
  }
}
```

The script for resampling spectra to WorldView2 spectral resolution

```
rm(list=ls())
library(hsdar)
library(RStoolbox)

data_path <- "C:\\bangka\\lab\\Analysis2"
setwd("C:\\bangka\\lab\\Analysis2")

z <- c("lib_450_1000_loc1", "lib_450_1000_loc23") #loading spectral library
for (q in z){
  flist <- paste0("C:/bangka/lab/Analysis2/",q)
  a <- paste0(data_path,"/",q,"_worldview2")
  sli <- readSLI(flist)
  tmp <- as.matrix(sli)
  lib <- specLib(tmp[,2:ncol(tmp)],tmp[,1])
  senti <- spectralResampling(lib, "WorldView2-8", rm.NA = TRUE, response_function = TRUE)
  senti_spec <- data.frame(senti@spectra@spectra_ma)
  senti_wav <- data.frame(senti@wavelength)
  colnames(senti_spec) <- t(senti_wav)
  senti_ID <- data.frame(senti@ID)
  rownames(senti_spec) <- t(senti_ID)
  senti_spec <- t(senti_spec[-c(11,12,13)])
  senti_wav <- data.frame(senti_wav[-c(11,12,13).])
  senti_resample <- data.frame(senti_wav, senti_spec)
  colnames(senti_resample)[1] <- "wavelength"
  na <- data.frame(colnames(senti_resample)[2:ncol(senti_resample)])
  na[] <- lapply(na, gsub, pattern='X', replacement='')
  colnames(senti_resample)[2:length(senti_resample)] <- t(na)
  senti_resample <- senti_resample[2:8,]
  writeSLI(senti_resample, path = a, wavl.units = "Nanometer")
}
```

The script for resampling spectra to Sentinel-2 MSI spectral resolution

```
rm(list=ls())
library(hsdar)
library(RStoolbox)
library(dplyr)
data_path <- "C:\\bangka\\lab\\Analysis2"
setwd("C:\\bangka\\lab\\Analysis2")
z <- c("lib_450_1000_loc1", "lib_450_1000_loc23")
for (q in z){
  flist <- paste0("C:/bangka/lab/Analysis2/",q)
  a <- paste0(data_path,"/",q,"_senti")
  sli <- readSLI(flist)
  tmp <- as.matrix(sli)
  lib <- specLib(tmp[,2:ncol(tmp)],tmp[,1])
  senti <- spectralResampling(lib, "Sentinel2", rm.NA = TRUE, response_function = TRUE)
  senti_spec <- data.frame(senti@spectra@spectra_ma)
  senti_wav <- data.frame(senti@wavelength)
  colnames(senti_spec) <- t(senti_wav)
  senti_ID <- data.frame(senti@ID)
  rownames(senti_spec) <- t(senti_ID)
  senti_spec <- t(senti_spec[-c(11,12,13)])
  senti_wav <- data.frame(senti_wav[-c(11,12,13).])
  senti_resample <- data.frame(senti_wav, senti_spec)
  colnames(senti_resample)[1] <- "wavelength"
  na <- data.frame(colnames(senti_resample)[2:ncol(senti_resample)])
  na[] <- lapply(na, gsub, pattern='X', replacement='')
  colnames(senti_resample)[2:length(senti_resample)] <- t(na)
  senti_resample <- senti_resample[c(2:7,9).]
  writeSLI(senti_resample, path = a, wavl.units = "Nanometer")
}
```

The script for resampling spectra to Landsat 8 OLI spectral resolution

```
rm(list=ls())
library(hsdar)
library(RStoolbox)
library(dplyr)
data_path <- "C:\\bangka\\lab\\Analysis2"
setwd("C:\\bangka\\lab\\Analysis2")
z <- c("lib_450_1000_loc1")
for (q in z){
  flist <- paste0("C:/bangka/lab/Analysis2/",q)
  a <- paste0(data_path,"/",q,"_Landsat8")
  sli <- readSLI(flist)
  tmp <- as.matrix(sli)
  lib <- speclib(tmp[,2:ncol(tmp)],tmp[,1])
  senti <- spectralResampling(lib, "Landsat8", rm.NA = TRUE, response_function = TRUE)
  senti_spec <- data.frame(senti@spectra@spectra_ma)
  senti_wav <- data.frame(senti@wavelength)
  colnames(senti_spec) <- t(senti_wav)
  senti_ID <- data.frame(senti@ID)
  rownames(senti_spec) <- t(senti_ID)
  senti_spec <- t(senti_spec[-c(11,12,13)])
  senti_wav <- data.frame(senti_wav[-c(11,12,13),])
  senti_resample <- data.frame(senti_wav, senti_spec)
  colnames(senti_resample)[1] <- "wavelength"
  na <- data.frame(colnames(senti_resample)[2:ncol(senti_resample)])
  na[] <- lapply(na, gsub, pattern='X', replacement='')
  colnames(senti_resample)[2:length(senti_resample)] <- t(na)
  senti_resample <- senti_resample[2:5,]
  writeSLI(senti_resample, path = a, wavl.units = "Nanometer")
}
```

The script for deriving spectral parameters

```
rm(list=ls())
library(RStoolbox)
library(tcltk)
library(readr)
library(MESS)
library(readxl)
library(psych)
library(xlsx) #load the package
library(hsdar) #spectral resample
library(prospectr)

a <- c("lib_450_1000_loc1", "lib_450_1000_loc23")

for(q in a){
  data_path <- "C:\\bangka\\lab\\Analysis"
  setwd("C:\\bangka\\lab\\Analysis")
  speclib <- paste0("C:/bangka/lab/Analysis/", q)
  sli <- readSLI(speclib)
  cr_wav <- data.frame(sli[1])
  cr_spec <- sli[-1]
  rownames(cr_spec) <- cr_wav[,1]
  rownames(sli) <- cr_wav[,1]

  #Band ratio
  para <- cr_spec[100,]/cr_spec[50,]
  row.names(para)[1] <- "Ratio 550,550"
  para[2,] <- cr_spec[262,]/cr_spec[224,]
  row.names(para)[2] <- "Ratio 712,674"

  # continuum removal 450-550 -----
  cr_wav2 <- data.frame(sli[1][1:100,])
  cr_spec2 <- sli[-1][1:100,]
  for (z in 1:ncol(cr_spec2)){cr_spec2[z] <- data.frame(continuumRemoval(cr_spec2[[z]],cr_wav2[[1]], type = "R"))}
```

```

sli2 <- data.frame(cr_wav2[1], cr_spec2)
colnames(sli2) <- colnames(sli)

#Band Depth
para[3,] <- 1- cr_spec2[50,]
row.names(para)[3] <- "Depth 500"

#Band Area
cr_wav_area <- sli2[1]
cr_spec_area <- sli2[-1]
cr_spec_area2 <- 1-cr_spec_area
area2 <- data.frame(cr_spec_area2[1,])
for (y in 1:ncol(cr_spec_area2)){area2[y]<-data.frame(auc(t(cr_wav_area), cr_spec_area2[,y], absolutearea = TRUE))}
rownames(area2)[1] <- paste0("Area 450,550")
para[4,] <- area2

# continuum removal 600-712 -----
cr_wav2 <- data.frame(sli[1][150:262,])
cr_spec2 <-sli[-1][150:262,]
for (z in 1:ncol(cr_spec2)){cr_spec2[z] <- data.frame(continuumRemoval(cr_spec2[[z]],cr_wav2[[1]], type = "R"))}

sli2 <- data.frame(cr_wav2[1], cr_spec2)
colnames(sli2) <- colnames(sli)

#Band Depth
para[5,] <- 1- cr_spec2[75,]
row.names(para)[5] <- "Depth 674"

#Band Area
cr_wav_area <- sli2[1]
cr_spec_area <- sli2[-1]
cr_spec_area2 <- 1-cr_spec_area
area2 <- data.frame(cr_spec_area2[1,])
for (y in 1:ncol(cr_spec_area2)){area2[y]<-data.frame(auc(t(cr_wav_area), cr_spec_area2[,y], absolutearea = TRUE))}
rownames(area2)[1] <- paste0("Area 600,712")
para[6,] <- area2

# continuum removal 712-832 -----
cr_wav2 <- data.frame(sli[1][262:382,])
cr_spec2 <-sli[-1][262:382,]
for (z in 1:ncol(cr_spec2)){cr_spec2[z] <- data.frame(continuumRemoval(cr_spec2[[z]],cr_wav2[[1]], type = "R"))}

sli2 <- data.frame(cr_wav2[1], cr_spec2)
colnames(sli2) <- colnames(sli)

#Band Depth
para[7,] <- 1- cr_spec2[61,]
row.names(para)[7] <- "Depth 772"

#Band Area
cr_wav_area <- sli2[1]
cr_spec_area <- sli2[-1]
cr_spec_area2 <- 1-cr_spec_area
area2 <- data.frame(cr_spec_area2[1,])
for (y in 1:ncol(cr_spec_area2)){area2[y]<-data.frame(auc(t(cr_wav_area), cr_spec_area2[,y], absolutearea = TRUE))}
rownames(area2)[1] <- paste0("Area 712,832")
para[8,] <- area2
para[9,] <- colnames(para)
rownames(para)[9] <- "ID"

labresult <- "C:/bangka/lab/Analysis/ICP.xlsx" #upload ICP result
labr <- read_excel(labresult, col_names = TRUE)
para <- data.frame(t(para))
join <- merge(para, labr, by="ID") # merge ICP result and the calculated spectral parameters.
write.xlsx(join, file = paste0(q, "_para.xls"),sheetName = "response",append=TRUE,row.names = TRUE)
}

```

The script for calculating the mean spectra

```
m(list=ls())
library(readr)
library(tcltk)
library(data.table)
data_path <- "C:\\bangka\\lab\\df analysis\\different size"
setwd("C:\\bangka\\lab\\df analysis\\different size")

flist <- tk_choose.files()
filepath <- flist[1]
my.data <- lapply(flist,
  read_delim,
  "\t", escape_double = FALSE, trim_ws = TRUE)
B <- Reduce("+", my.data) / length(my.data)

Bname <- sub(pattern = "(.*)\\.", replacement = "\\1", basename(filepath))
Bname <- gsub("\\.", "", Bname, fixed=FALSE)

samp <- substr(colnames(m2)[2], 1, 3)
ab <- strsplit(Bname, split='.', fixed=TRUE)
a <- colnames(m2)[2]
samp <- gsub("\\.", "", Bname)

colnames(m2)[2]<- samp
write.table(m2, paste0(samp, ".txt"), sep="\t", row.names=FALSE)
```

The script for generating the improved band math images

```
m(list=ls())
library(RStoolbox)
library(tcltk)
library(readr)
library(MESS)
library(readxl)
library(psych)
library(xlsx) #load the package
library(hsdr) #spectral resample
library(prospectr)
library(raster)

data_path <- "C:\\bangka\\lab\\Analysis4Senti\\senti\\r"
setwd("C:\\bangka\\lab\\Analysis4Senti\\senti\\r")

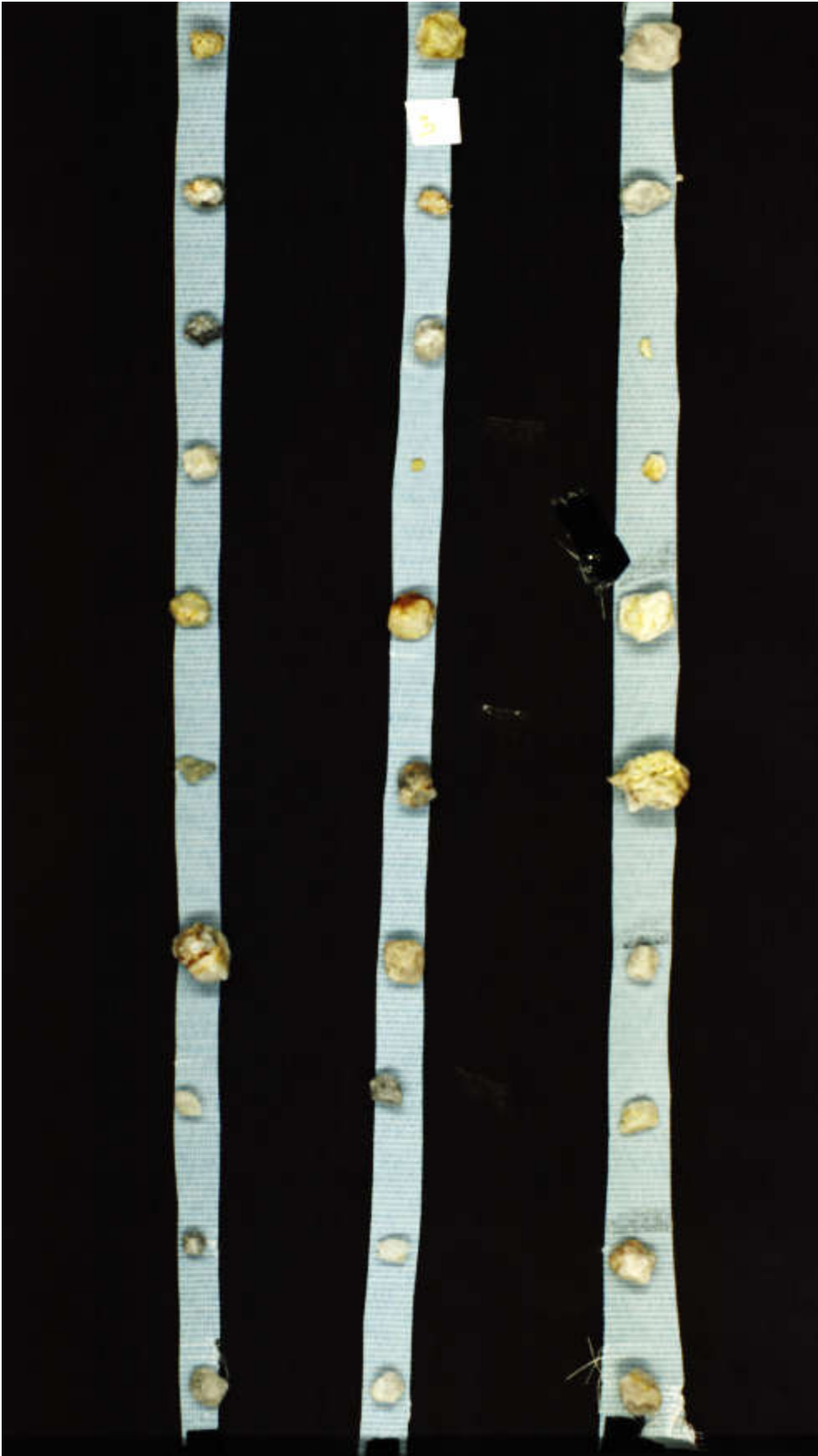
t1 <- readGDAL(paste0(data_path, "\\senti_conti"), band = c(2,3,4))
t2 <- readGDAL(paste0(data_path, "\\senti_conti"), band = c(3,4,5))
t3 <- readGDAL(paste0(data_path, "\\senti_conti"), band = c(4,5,6))
ts1 <- stack(t1)
ts2 <- stack(t2)
ts3 <- stack(t3)

rc <- function(x1,x2,x3) {
  ifelse(x1 < x2 & x2 > x3, -1, ifelse(((x1-x2)/(x3-x2))<0, -1,((x1-x2)*(x3-x2))))
}
r.class1 <- overlay(ts1, fun=rc)
r.class2 <- overlay(ts2, fun=rc)
r.class3 <- overlay(ts3, fun=rc)
plot(r.class1)
r.class1[is.na(r.class1)] <- -1
r.class2[is.na(r.class2)] <- -1
r.class3[is.na(r.class3)] <- -1
# writeRaster(r.class, "665.envi", drivename="ENVI", type="Float32", overwrite = TRUE)
# writeRaster(r.class, "705.envi", drivename="ENVI", type="Float32", overwrite = TRUE)
writeRaster(r.class1, "665.envi", drivename="ENVI", type="Float32", overwrite = TRUE)
writeRaster(r.class2, "705.envi", drivename="ENVI", type="Float32", overwrite = TRUE)
writeRaster(r.class3, "740.envi", drivename="ENVI", type="Float32", overwrite = TRUE)
```

Appendix E The arrangement of 126 grains

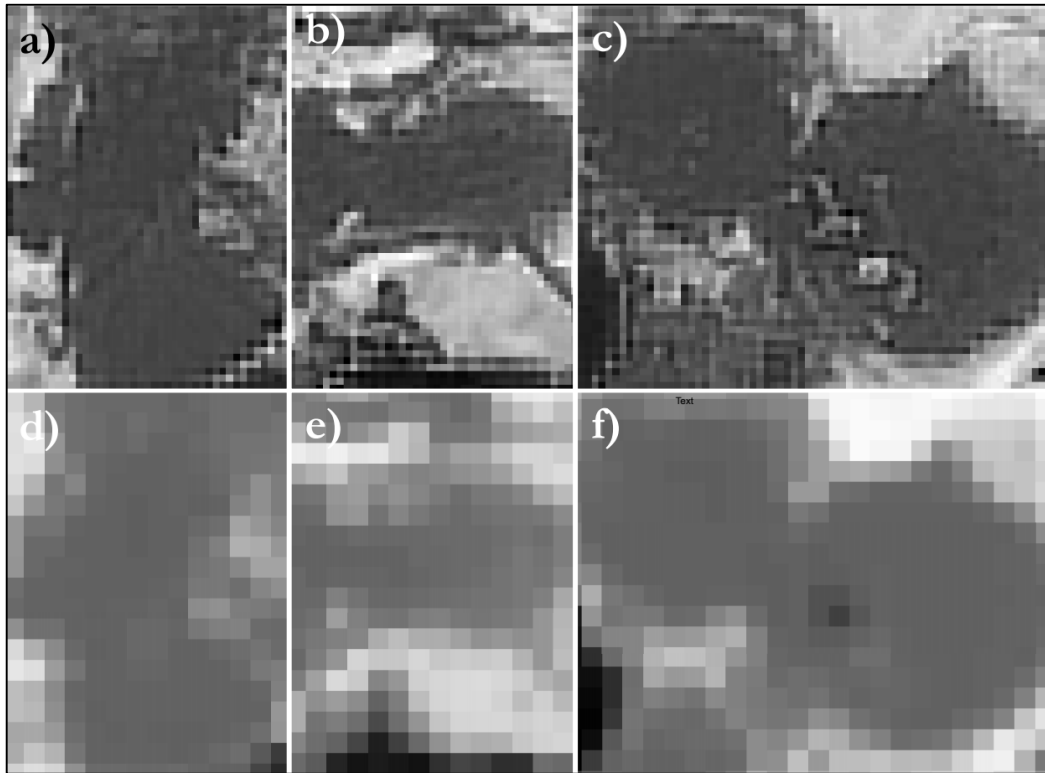




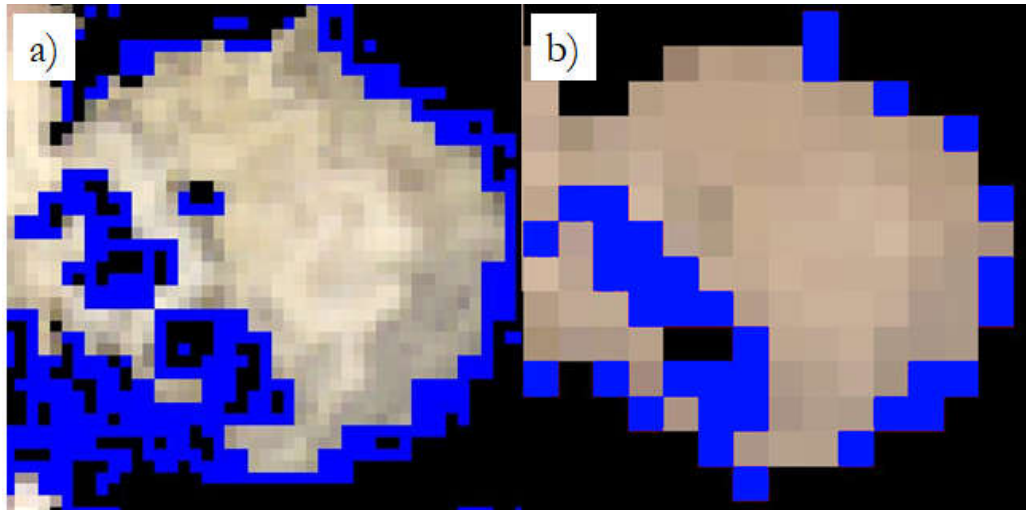




Appendix F Images of NDVI products and water masked

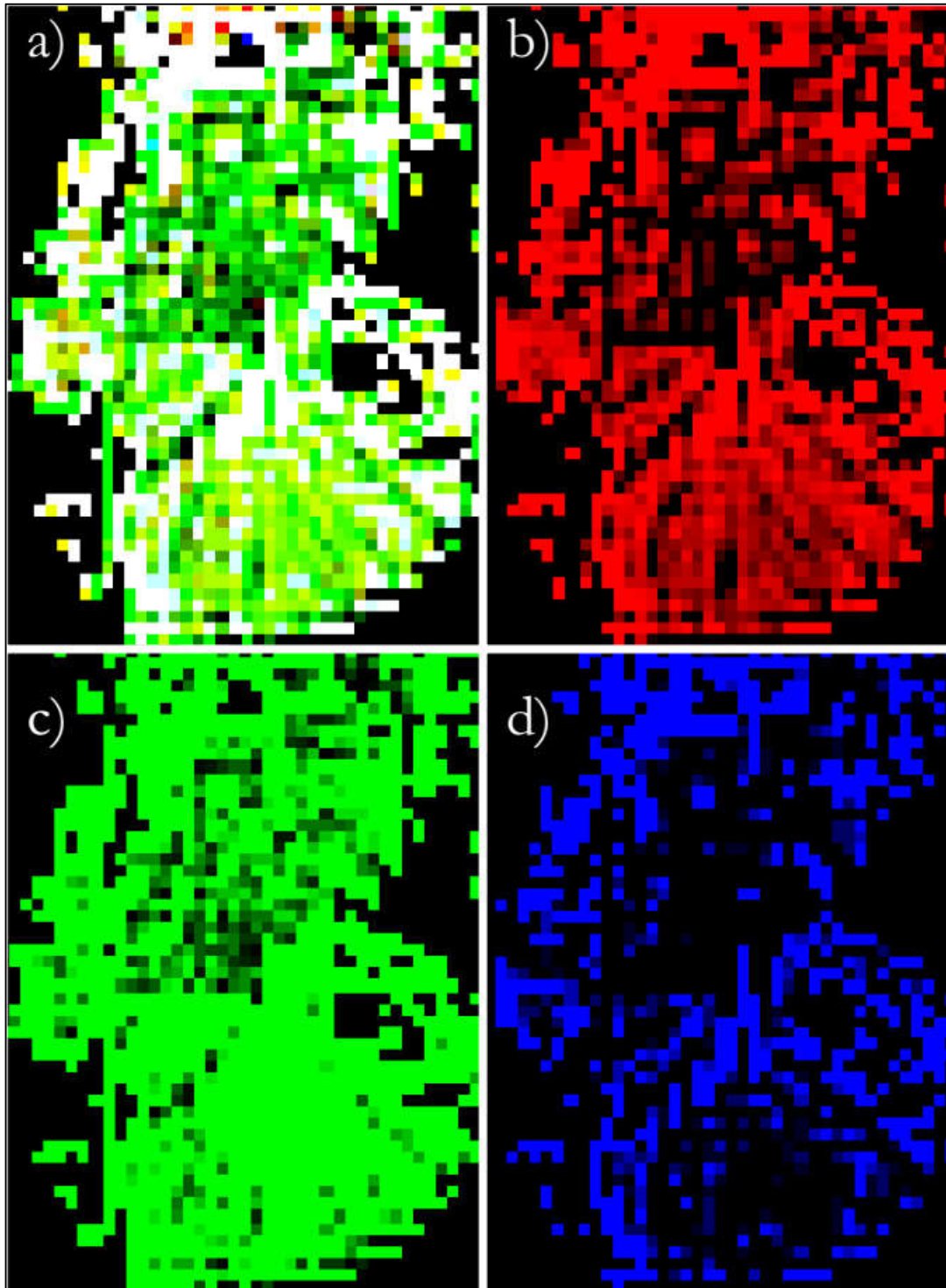


Images of NDVI products using Sentinel-2 MSI and Landsat 8 OLI images. NDVI images for location 1(a, d), location 2 (b, e), and location (c, f) resulted from Sentinel-2 MSI (a, b, c) and Landsat 8 OLI (d, e, f) images in a 2–98% linear stretch with a colour ramp *low*  *high*. The spatial resolution of NDVI product using Landsat 8 OLI and Sentinel-2 MSI is 30m and 10m respectively.

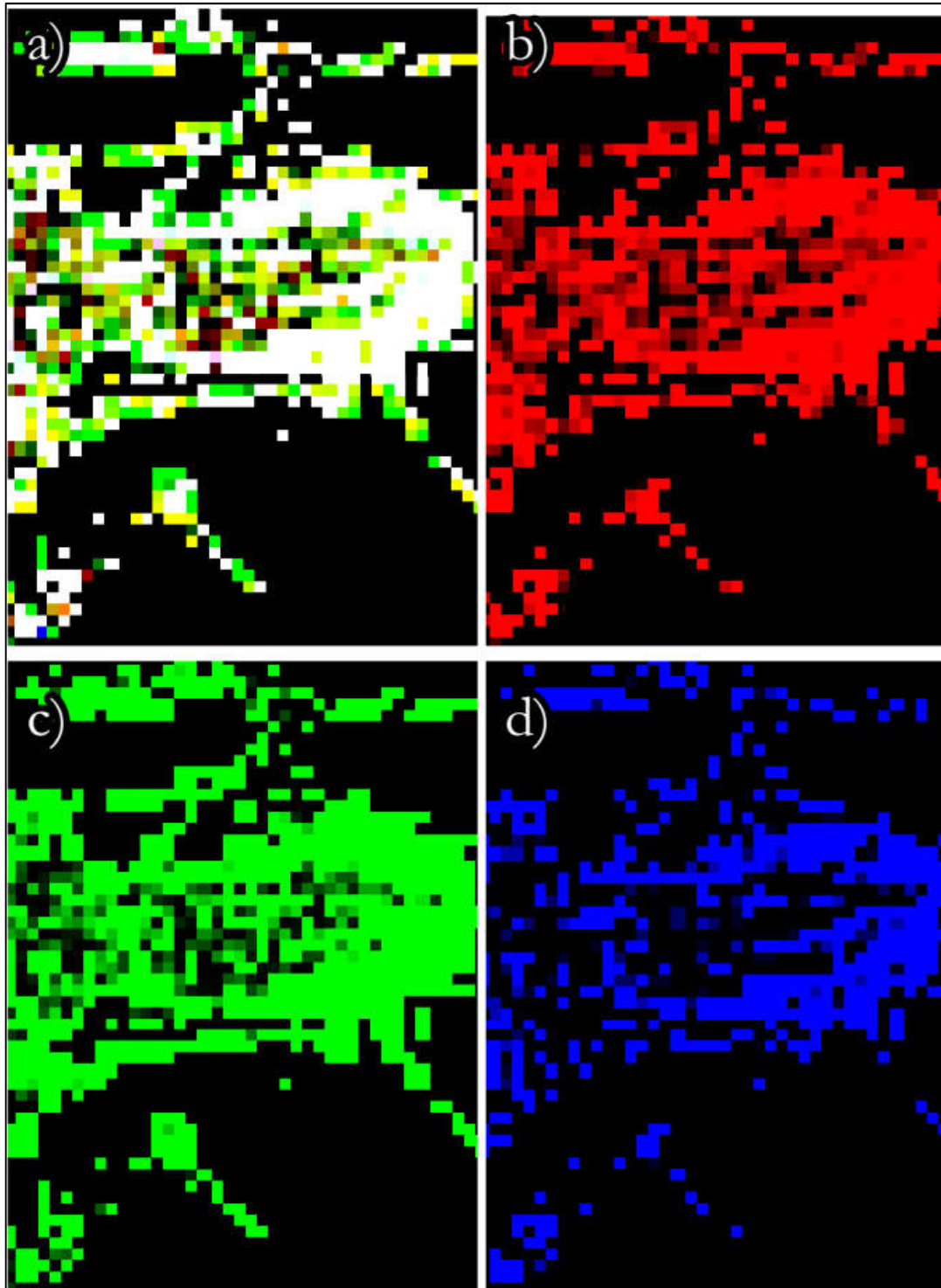


Mixed pixels of vegetation and water masked using Sentinel-2 MSI band 8a (a) and Landsat 8 OLI band 5(b). The threshold for masking is 0.4 for both images. Blue colour indicates mixed area between vegetation and water. Black colour indicates vegetation area that was masked using NDVI beforehand.

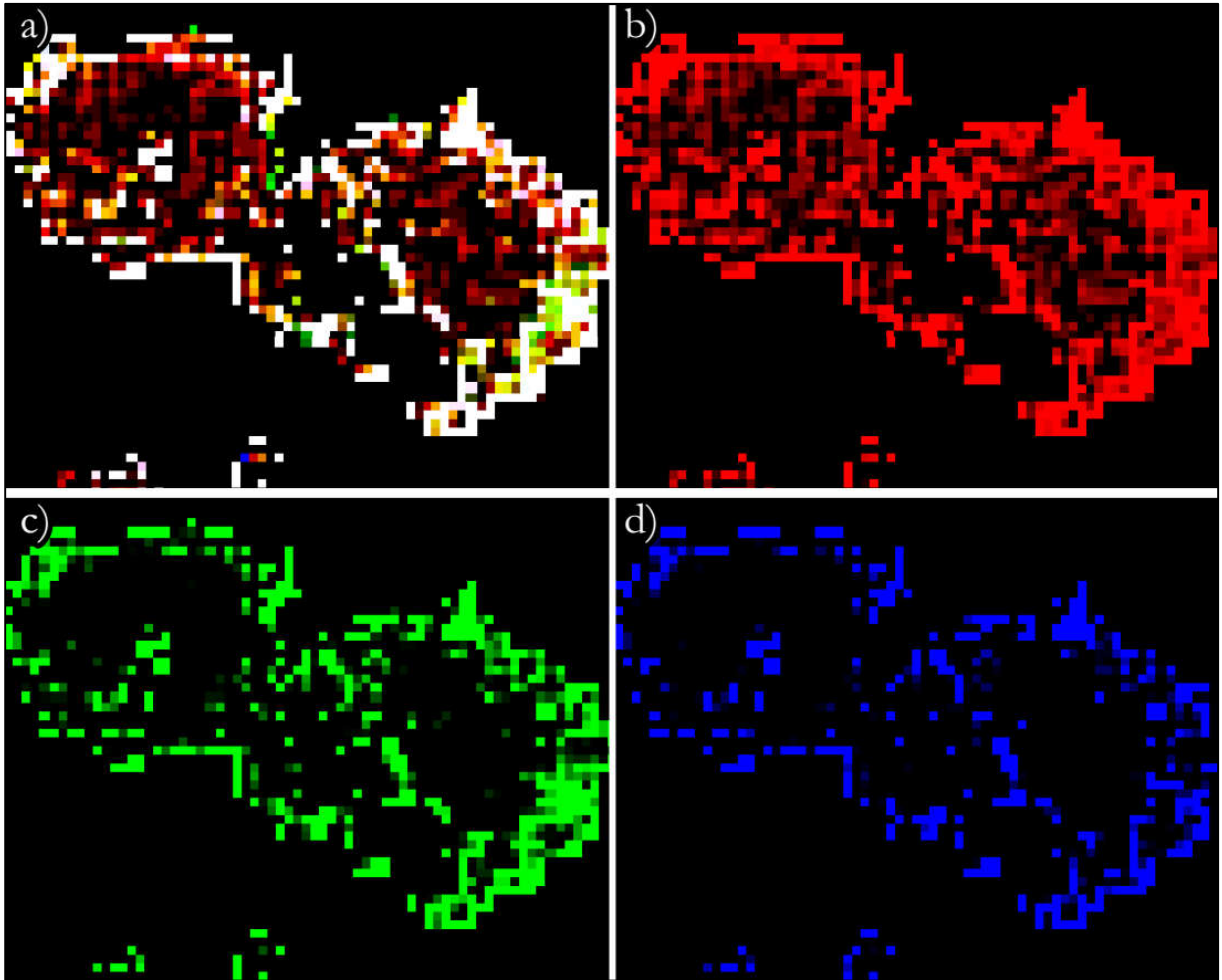
Appendix G Images of spectral parameter products



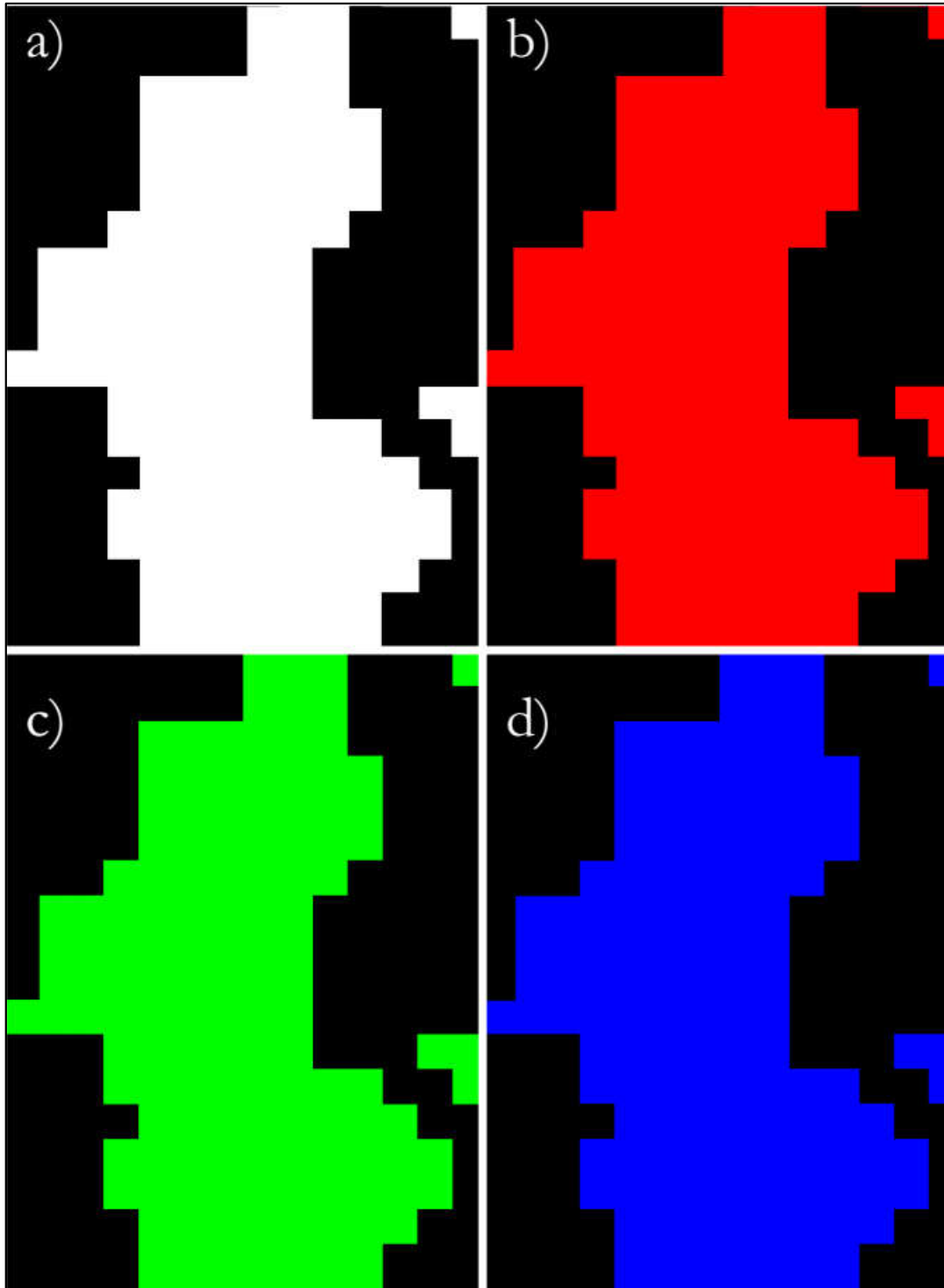
Images of spectral parameter products using a Sentinel-2 MSI image with a 10m spatial resolution for location 1. The images are masked for vegetation and water. a) Showing an RGB colour composite of band ratio ($B5/B4$), band depth ($B4$), and band math ($(B3-B4) \times (B5-B4)$). A white-coloured pixel indicates a combination of high value for the three bands, meaning that there is an absorption feature at Band 4. b) The band ratio product with a colour ramp *low* (1.0001) ■ *high* (1.05). c) The band depth product with a colour ramp *low* (0) ■ *high* (0.02). d) The band math product with a colour ramp *low* (0) ■ *high* (0.0004).



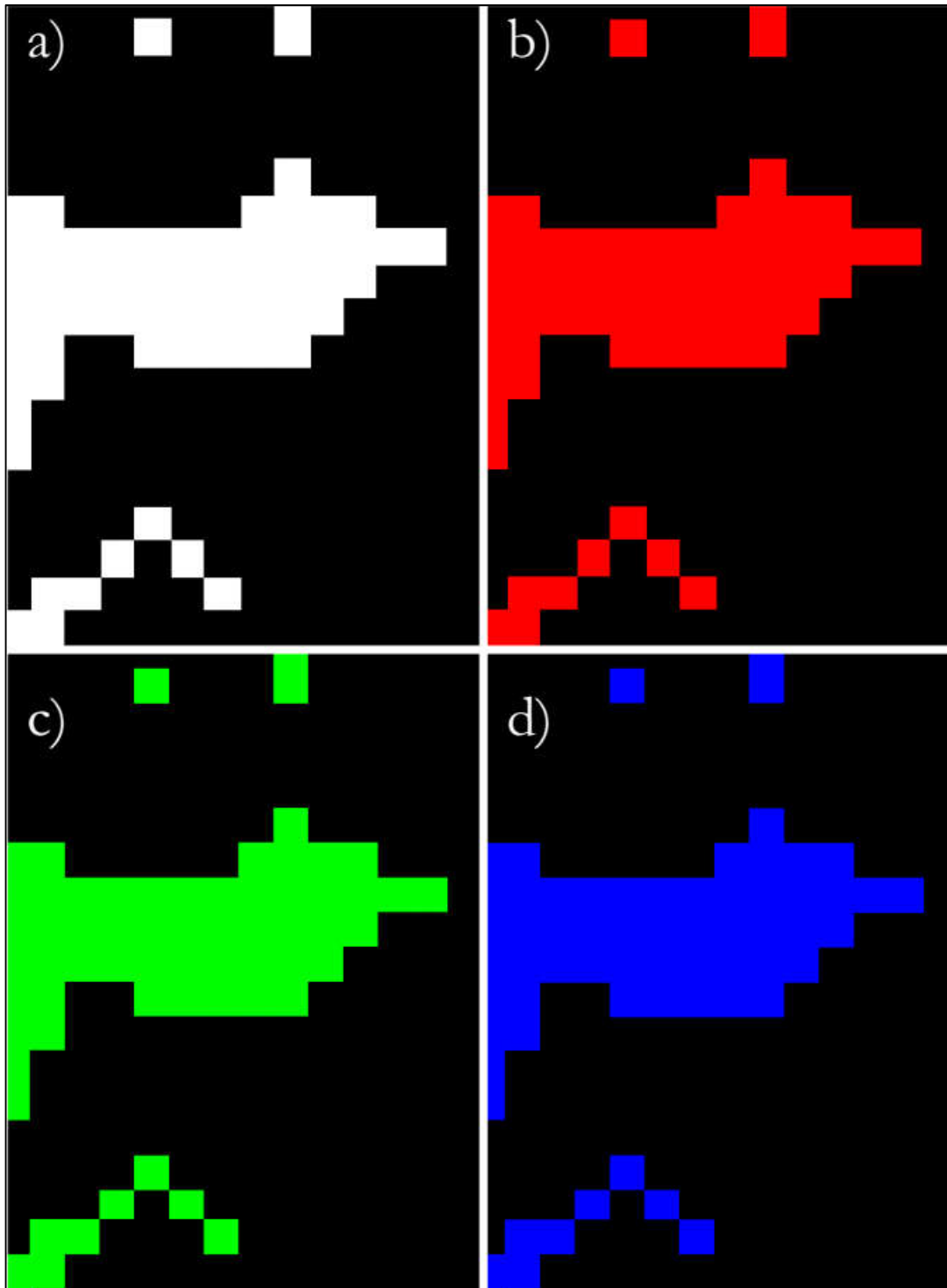
Images of spectral parameter products using a Sentinel-2 MSI image with a 10m spatial resolution for location 2. a) Showing an RGB colour composite of band ratio ($B5/B4$), band depth ($B4$), and band math ($(B3-B4) \times (B5-B4)$). A white-coloured pixel indicates a combination of high value for the three bands, meaning that there is an absorption feature at Band 4. b) The band ratio product with a colour ramp *low* (1.0001) ■ *high* (1.05). c) The band depth product with a colour ramp *low* (0) ■ *high* (0.02). d) The band math product with a colour ramp *low* (0) ■ *high* (0.0004).



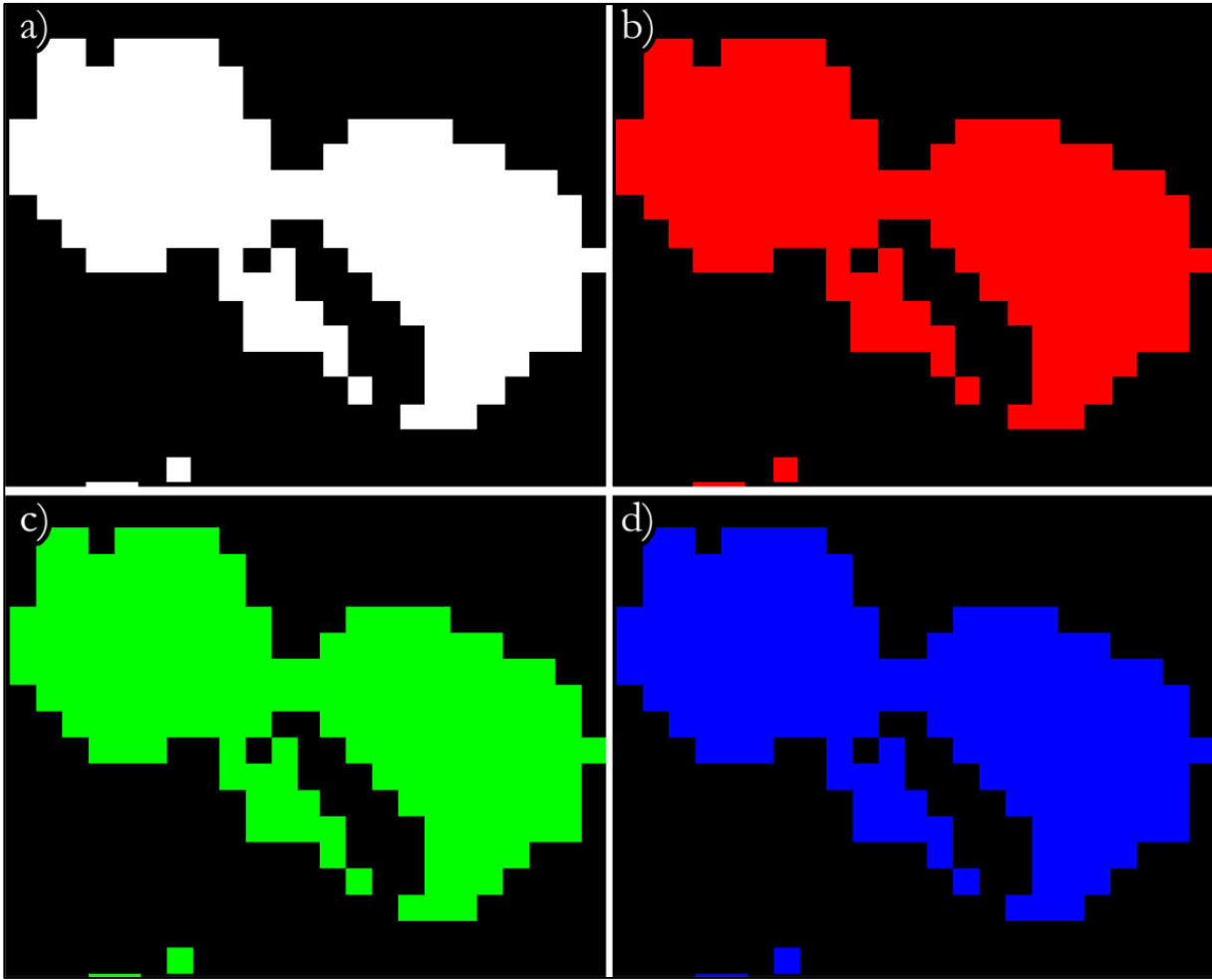
Images of spectral parameter products using a Sentinel-2 MSI image with a 10m spatial resolution for location 3. The images are masked for vegetation and water. a) Showing an RGB colour composite of band ratio ($B5/B4$), band depth ($B4$), and band math ($(B3-B4) \times (B5-B4)$). A white-coloured pixel indicates a combination of a high value for the three bands, meaning that there is an absorption feature at Band 4. b) The band ratio product with a colour ramp *low* (1.0001)  *high* (1.05). c) The band depth product with a colour ramp *low* (0)  *high* (0.02). d) The band math product with a colour ramp *low* (0)  *high* (0.0004).



Images of spectral parameter products using a Landsat 8 OLI image with a 30m spatial resolution for location 1. The images are masked for vegetation and water. a) Showing an RGB colour composite of band ratio ($B5/B4$), band depth ($B4$), and band math ($(B3-B4) \times (B5-B4)$). A white-coloured pixel indicates a combination of high value for the three bands, meaning that there is an absorption feature at Band 4. b) The band ratio product with a colour ramp *low* (1.0001)  *high* (1.05). c) The band depth product with a colour ramp *low* (0)  *high* (0.02). d) The band math product with a colour ramp *low* (0)  *high* (0.0004). After stretching the images with the threshold, no pixels of band ratio, band depth, and band math image are lower than the high limit of colour ramp; so that they appear red in band ratio image, green in band depth image, and blue in band math image.



Images of spectral parameter products using a Landsat 8 OLI image with a 30m spatial resolution for location 2. The images are masked for vegetation and water. a) Showing an RGB colour composite of band ratio ($B5/B4$), band depth ($B4$), and band math ($(B3-B4) \times (B5-B4)$). A white-coloured pixel indicates a combination of high value for the three bands, meaning that there is an absorption feature at Band 4. b) The band ratio product with a colour ramp *low* (1.0001)  *high* (1.05). c) The band depth product with a colour ramp *low* (0)  *high* (0.02). d) The band math product with a colour ramp *low* (0)  *high* (0.0004). After stretching the images with the threshold, no pixels of band ratio, band depth, and band math image are lower than the high limit of colour ramp; so that they appear red in band ratio image, green in band depth image, and blue in band math image.



Images of spectral parameter products using a Landsat 8 OLI image with a 30m spatial resolution for location 3. The images are masked for vegetation and water.. a) Showing an RGB colour composite of band ratio ($B5/B4$), band depth ($B4$), and band math ($(B3-B4) \times (B5-B4)$). A white-coloured pixel indicates a combination of high value for the three bands, meaning that there is an absorption feature at Band 4. b) The band ratio product with a colour ramp *low* (1.0001) ■ *high* (1.05). c) The band depth product with a colour ramp *low* (0) ■ *high* (0.02). d) The band math product with a colour ramp *low* (0) ■ *high* (0.0004). After stretching the images with the threshold, no pixels of band ratio, band depth, and band math image are lower than the high limit of colour ramp; so that they appear red in band ratio image, green in band depth image, and blue in band math image.